Molecular Modeling for Rational Design of Polymer Dielectrics

Mayank Misra

Submitted in partial fulfillment of the
requirements for the degree of
Doctor of Philosophy
in the Graduate School of Arts and Sciences

COLUMBIA UNIVERSITY

2017

ABSTRACT

MOLECULAR MODELING FOR RATIONAL DESIGN OF POLYMER DIELECTRICS

MAYANK MISRA

The state-of-the-art in high voltage and high energy density capacitors is dominated by biaxially oriented polypropylene (BOPP), a linear dielectric with electronic polarizability but low dielectric constant ($\sim$ 2.2). BOPP provides an energy density of 5 J/cm^3 at the breakdown, which occurs at $\sim$ 720 V/μm for films $\sim$ 10 μm thick. While there are many approaches to increase the energy, they either offer solutions to specific applications or suffer from fundamental limitations. The principal focus of the dissertation will be centered on rational design for the development of such materials. We study all three verticals of dielectric properties, namely: dielectric permittivity; dielectric loss; and breakdown strength. We then use the information obtained to design a copolymer with enhanced dielectric properties. We start by using simulations and experiments to delineate the mechanism by which the addition of a small number of polar –OH groups to a nonpolar polymer increases the static relative permittivity (or dielectric constant) by a factor of 2. However, the dielectric loss in the frequency regime of interest to power electronics is less than 1%. We observe that a small amount of adsorbed water plays a critical role in this attenuated loss. Further, we study the effect of other polar pendant groups on dielectric properties of polyethylene. By systematically comparing the static relative permittivity of crystalline and semi-crystalline samples we find amorphous phase as the dominant player in these types of material. The constraints

provided by the surrounding chains significantly impede dipolar relaxations in the crystalline regions, whereas amorphous chains must sample all configurations to attain their fully isotropic spatial distributions. We also explore the use of the time–temperature superposition (tTS) principle for calculating the dielectric loss of the dielectric materials. This approach helps us explore time scales in simulations which were previously inaccessible using classical MD. We find that the tTS method performed well in determining dielectric losses in the system as long as unrelaxed components are not included in the calculation. This methodology, which provides us with a significantly faster and reliable pathway for calculation of dielectric loss, allows us to identify the role of polar sidegroups on the dielectric loss of common non-polar polymeric dielectrics. Further, we explore the dielectric breakdown mechanism in polymer dielectrics by introducing external electric fields in the materials. Conventionally the prediction of dielectric strength has focused on ground state energy calculation, thus restricting the analysis of the breakdown process to purely electronic in nature. While this provides reasonable predictions for low-temperature systems, we observe that electromechanical breakdown plays a crucial role in the high-temperature regimes. Our simulation results suggest that fracture mechanics drive electromechanical breakdown, which dominates over electronic breakdown at relevant operating temperatures. Finally, we utilized these fundamental insights into dielectric properties for designing copolymer with enhanced dielectric properties.

Contents

List of Figures

List of Tables

Acknowledgements

During the last five and a half years, in the journey of discovering fundamentals of polymer dielectrics, I have discovered myself. In the language of polymer physics, the constant struggle of being under the fire has transformed me from amorphous (*random*) to crystalline (*or at least semi-crystalline*). Every person I came in intellectual contact with over the course of my Ph.D. has left an unforgettable impression on me.

Firstly, I would like to express my sincere gratitude to my advisor Prof. Sanat for the continuous support and guidance. He provided me with enough freedom during my Ph.D. research so that I can develop the ability to do independent research while not letting me stray from the eventual goal. I have learned a lot from working under him, especially the importance of seeing the big picture. I am sure that I still have a lot to learn, but I am certain that his guidance has shown me the right direction. I could not have imagined having a better advisor and mentor for my Ph.D. study.

When I joined the Kumar Group, I had very little knowledge of polymer physics or simulations. I would firstly like to thank Prof. Christopher Durning and Prof. Jeffrey Koberstein, who are also my committee members, for teaching me everything I know about polymers. I vividly remember my first class at Columbia University

on a gloomy Tuesday at 10 AM when Prof. Durning entered the room and lit it up the room with his knowledge. His introduction to polymer physics helped me learn that polymers have more to them than just chemistry. After taking multiple classes on polymers with Prof. Koberstein I now wear polymer glasses, where anything I see in a room reminds me of the polymer responsible for it. I also reached a point in my Ph.D. where for around 36 months I only had dreams related to polymers (*my parents thought I was going mad*). I would also like to thank Prof. Angelo Caccuito and Prof. Jeffrey Kysar for serving as my committee members despite their busy schedule.

A complete research is incomplete without collaboration and here I would like to thank Prof. Rampi Ramprasad, Prof. Robert Weiss, Prof. Mike Chung, Prof. Mukerrem Cakmak, and Prof. Greg Sotzing who provided me consistent guidance and an opportunity to collaborate with their groups. The students from their groups Dr. Ghanshyam Pilania, Dr. Chenchen Wang, Dr. Sahil Gupta, Dr. Xuepei Yuan, Arun Mannodi-Kanakkithodi and Greg Treich were helpful and tolerant with me while teaching me how DFT and experiments worked. Working on the collaborative project with them gave me new insights to polymer dynamics and synthesis.

I would like to give my thanks to all the current and past group members I have met in Prof. Kumars lab, including Dr. Dong Meng, Dr. Yuping Xie, Dr. Behnaz Bozorgui, Dr. Manish Agarwal, Dr. Jagannathan T. Kalathi, Dr. Michael Clark, Dr. Mithun Radhakrishna, Dr. Daniel Sinkovits, Dr. Makoto Asai , Dr. Vianney Gimenez Pinto, Dr. Kai Zhang, Dr. Dan Zhao, Thi Vo, Ellie Buenning, Connor Robert Bilchak, Sebastian Russell, Andrew Matthew Jimenez, and Gianna Maria

Credaroli; I have learnt a lot from all of you and thanks for being there whenever I needed help (*which was frequent*). I would also like to mention Chathuranga De Silva and Porakrit Leophairatana for the extensive discussions on polymers and being cooperative co-TA's. want to express my sincerest gratitude to my mentor Dr. Manish Agarwal for helping me start my research in the lab and teaching the basics of polymer simulations.

Life can be a lot easier when you find friends who do not hesitate to call you out for your idiocy while also are standing by you during hard times. Thi Vo, Sharvil Patil, and Sanghamitra Gogoi you have been an integral part of my journey at Columbia University and I hope the relationship I have with you all lasts forever. Listening to me talk about my research and non-research ideas can be taxing at times and I appreciate the patience you, all shown me.

I would also like to thank my grandfather (Dr. Narendra Prasad Misra) and my uncle (Dr. Vishal Misra) who have been my source of inspiration since childhood. Finally, I want to acknowledge my parents (Manoj and Nivedita Misra), who have shown me the light when the times were dark. I thank you both for the constant support you continually provide and keeping me shielded all the difficulties of life. In the end, I would like to also thank the person whose photo resides in my wallet. My brother Eashan, thank you for tolerating my torments so that I can find inner peace.

Dedicated to my parents and

my grandmother

Good words don't cost anything,
but they pay you beyond your expectations.
–Maya Misra

Chapter 1

Introduction

1.1 Introduction

Recent advances in pulsed power technology have made it possible to apply the technology for various applications by utilizing its high power efficiency. Pulsed power is rapid release of energy from an energy storage device allowing power to be amplified at moderate energy consumption. In pulsed power, the energy is stored in the energy storage device over a long time period, and then it is released in a short and intense pulse, which gives high instantaneous peak power. The instantaneous high peak power has given rise to many applications, from surface treatment of materials to treatment of microorganisms in foods [1].

There are many energy-storage devices incorporating batteries, supercapacitors, electrolytic capacitors, and solid-state capacitors. These elements possess different power and energy densities as depicted in the modified Ragone Chart in Figure 1.1. Fuel cells and batteries exhibit high-energy densities but have low-power densities. Capacitors are on the other end of the spectrum where they possess high-power densities with low-energy densities due to the short discharge times below 0.01 seconds [2]. Capacitor components have the highest power density among all of the devices

shown in Figure 1.1 and are perfect for pulse power generation. However, the primary limitation for capacitors is energy density, which is significantly lower than other energy storage and conversion devices.

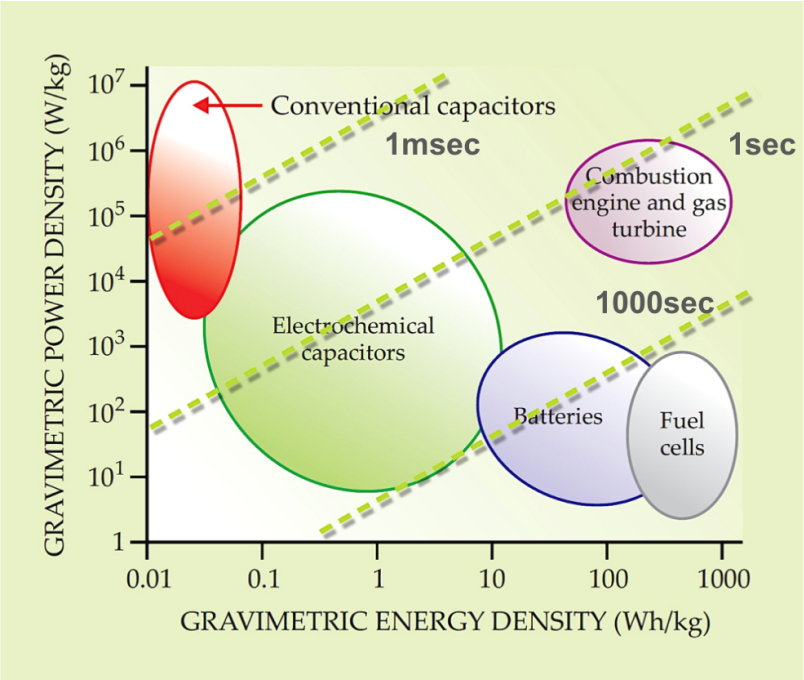

Figure 1.1: Power density vs energy density for various energy storage components [3].

1.2 Dielectric Properties

The selection and design of a dielectric material depends on the requirements specific to the application. In the case of dielectric applications, requirements can be stated in terms of the following properties: capacitance, processability, dissipation factor, mechanical strength, electrical breakdown, temperature stability, cost, and so on [4]. The capacitance and dissipation factor are known to be directly related to the material's intrinsic properties, while very little is known about the dependency of

electrical breakdown which we will delineate in this dissertation. Capacitance is related to the static dielectric permittivity. For the case where the material is in between parallel electrodes, and the capacitance is given as

$$C = \varepsilon_0 \varepsilon_r \frac{A}{d} \tag{1.1}$$

where, ε_0 is the permittivity of free space (8.85x10^{12} F/m), ε_r is the static permittivity or static dielectric constant, A and d are the cross-sectional area and thickness of the material respectively. In general, for any shape of the electrodes, the capacitance is found to be linearly dependent on static permittivity.

The dissipation factor, tanδ, is defined by the real part of the complex relative permittivity, ε_r', and the imaginary part of the complex relative permittivity, ε_r'', given by

$$tan\delta = \frac{\varepsilon_r''}{\varepsilon_r'} \tag{1.2}$$

Undesirable dielectric heating increases with increasing dielectric loss.

A dielectric shows various polarization mechanisms including orientational, ionic, and electronic polarization. The real and imaginary parts of the complex relative permittivity are dependent on frequency as depicted in Figure 1.2. Dielectric permittivity displays a decrease when a polarization mechanism is induced at a frequency. Dielectric loss shows the highest value when polarization frequency is the same as vibration frequency [5].

If an electric field is applied to a linear dielectric material such as polymers, e.g.,

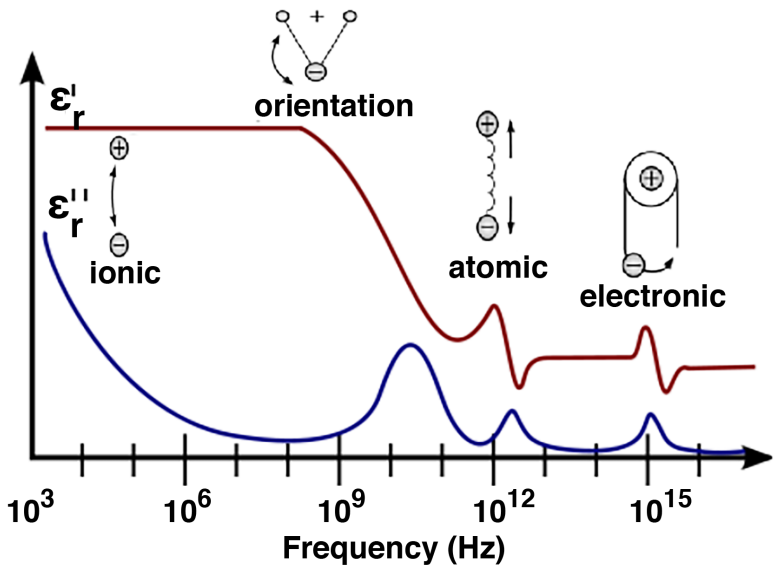

Figure 1.2: Typical frequency dependence of dielectric permittivity (ε_r') and loss (ε_r'') for a dielectric material [6].

polyethylene or polypropylene , the polarization-electric field (P-E) will show a linear response. If an electric field is applied to a ferroelectric material, a polarization will remain after removing the electric field and P-E will show a hysteretic non-linear response. The dielectric displacement is directly proportional to the applied electric field given by

$$P = \varepsilon_0 \varepsilon_r E \tag{1.3}$$

Hence the static relative permittivity (ε_r) of a material is also calculated from slope of P-E curve. While the inside the hysteresis loop is proportional to the dielectric loss (ε_r''). The area under the curve is related to the stored energy in the dielectric.

$$U_d = \int E \mathrm{d}D \tag{1.4}$$

The maximum energy stored per unit volume (U_e) is related to dielectric permittivity and breakdown strength is given as

$$U_e = \frac{1}{2}\varepsilon_0\varepsilon_r E_b^2 \cong \frac{1}{2}CV_m^2\frac{1}{Ad} \tag{1.5}$$

where, E_b is the dielectric breakdown, which is proportional to the maximum applied voltage V_m. While A and d are the cross-sectional area and thickness of the material respectively. Consequently, the low energy density for dielectric materials can be achieved by increasing the relative permittivity or the dielectric breakdown strength of the material. However, an increase in the dielectric constant will lead to an increase in dielectric losses, leading to an increase of equivalent series resistance. Due to internal resistances some portion of electrical energy is absorbed by the material in the form of thermal energy, which randomizes dipole orientation. Hence, dipole moments cannot react to changes in electric fields instantaneously resulting in dielectric loss [7].

1.3 Dielectric Materials

Dielectric materials were traditionally made from ceramic materials e.g., SiO2 and SiOF. While inorganic materials have higher dielectric constants than polymers, polymers are finding increasing use as dielectric materials. As early as the mid sixties polymers e.g., polyvinyl fluoride was used as dielectric materials in capacitors [7]. The use of polymer became popular due to their easier processing, flexibility, and self-healing property, which is driven by lower thermal properties such as glass transition and melting temperature. Their solubility is controllable without offsetting

Polymeric Film	Operating temperature (°C)	Breakdown Strength (V/μm)	Static Permittivity (ε_r)	Dissipation factor (tan δ)	Energy density (J/cm^3)
Polypropylene (PP)	105	700	2.2	≤ 0.02	1.2-1.4
Polyester (PET)	125	570	3.3	≤ 0.5	1-1.5
Polycarbonate (PC)	125	528	2.8	≤ 0.15	0.5-1
Polyvinylidene-fluoride (PVDF)	125	590	12	≤ 1.8	2.4
Polyethylene-naphthate (PEN)	125	550	3.2	≤ 0.15	1-1.5

Table 1.1: Dielectric properties of polymeric capacitor films.

their intrinsic properties. In the case of inorganic and ceramic materials, they have much higher thermal properties hence the temperature requirement leads to extreme processing temperatures.

Polymers can be polar or non-polar and this feature significantly affects the dielectric properties of the material. Examples of polar polymers include Polymethyl-methacrylate (PMMA), Polyvinylidene–fluoride (PVDF), Polyvinyl chloride (PVC), and Polycarbonates (PC) while non-polar polymers include Polytetrafluoroethylene (PTFE), Polyethylene (PE), Polypropylene (PP) and Polystyrene (PS). Under alternating electric field, polar polymers require some time to align the dipoles. The dielectric properties of the commonly used polymeric dielectric materials are compared in Table 1.1 [8, 9]. Polyester offers a high operating temperature, but it has a relatively high dissipation factor which increases with temperature and frequency. Polyvinylidenefluoride (PVDF) polymer film has a very high dielectric constant but also shows an high dissipation factor.

Polypropylene (PP) offers a combination of high energy storage capability, high breakdown field, low relative dielectric constant, and low dielectric losses (tan δ)

at industrial frequencies. The beneficial properties of polypropylene are due to the propylene chain molecules which can be oriented under the effect of the electric field and thus resulting in low loss. Hence the state of the art polymeric capacitor film is metallized biaxially oriented polypropylene (BOPP), with an energy storage density of ∼1.5 J/cc [9, 10]. This material has the unique combination of fast response, low loss, and high breakdown field in the range of 700 V/μm for small areas. Any improvement to polypropylene (PP) would require an increase in relative permittivity and/or breakdown strength while preserving low loss.

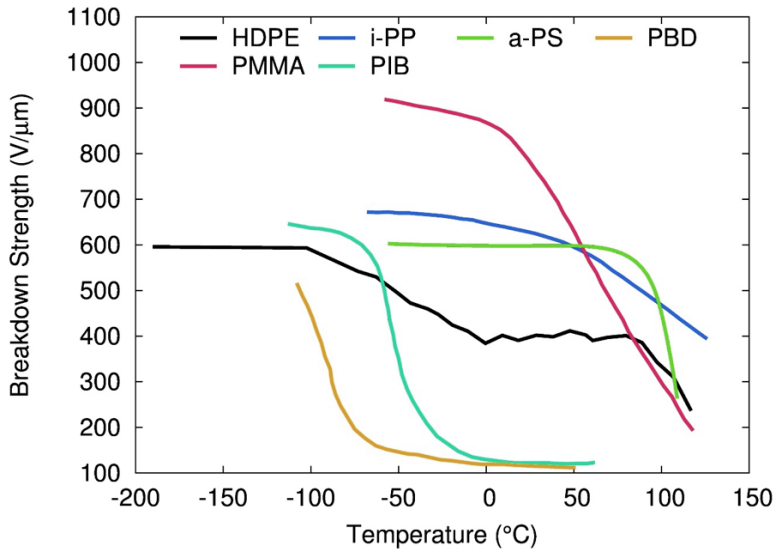

Figure 1.3: Temperature dependence of dielectric strength in polymer dielectrics. The electric strength increased with decreasing temperature [11].

For breakdown strength there is a strong dependence on temperature as depicted in Figure 1.3. A general trend in polymers is that breakdown strength decreases with increasing temperature. Some polymers show an abnormal change in breakdown strength with changing temperature. An understanding of the relationships among temperature dependence, polymer chemistry, and morphology may lead to improved

energy storage for polymer-based capacitors — which is the basis of this dissertation.

1.4 Simulations

Different approaches can be used to investigate a given dielectric phenomenon in polymer dielectrics. The most common one is the experiment, a technique that has been used by humans for a long time. Through experiments, the observer can get an accurate representation of the process of interest since an experiment by definition is carried out under controlled and reproducible circumstances [12]. Based on experiments hypotheses can be concluded, and laws and theories can be formulated. The second approach to investigate a phenomenon is a simulation where reality is modeled in a representative system. Simulations are used when conducting the experiment is costly, tedious, time-consuming, or sometimes not possible. Hence simulations have become a more popular way to probe material properties. Experiments are still required to validate and confirm results gathered from simulations. Computer simulations have become a very frequently used tool, not only in science but many different fields, such as risk management, stock market prediction, the development of cars and planes, drug discovery and much more. This dissertation focuses on computer simulation of molecules using fundamental equations that describe interactions between atoms. All the systems mentioned in this dissertation use different Molecular Dynamics (MD) simulations [13].

The first thing that is important to mention is that we do classical MD. That means quantum effects are not considered, or only considered in a mean-field manner.

Everything that underlies the laws of quantum physics, e.g. the motion of electrons, is neglected. The inaccuracies arising from these effects have to be corrected by the parametrisation of force field, which governs the main interactions between particles in MD. A force field consists of data specifying charges of atoms, van der Waals parameters, bond lengths, bond angles, and more. For all of our simulations we have used OPLS force field parameters [14–18]. In a molecular dynamics simulation we are interested in the interaction of atoms, which connected through chemical bonds. Each atom is represented by a sphere with position vector r and the potential energy function for OPLS force field is given by,

$$E(r^N) = E_{bonds} + E_{angles} + E_{impropers} + E_{dihedrals} + E_{nonbonded} \tag{1.6}$$

As we can see the potential energy function of our system consists of five terms. The first four terms are the bonded term and it considers interactions within a molecule. The last term is responsible for keeping the proper hybridization type for particular groups of atoms. When deviating from an ideal reference value of a length or an angle in these terms, the potential energy rises

$$E_{bonds} = \sum_{bonds} K_r(r - r_0)^2 \tag{1.7}$$

$$E_{angle} = \sum_{angles} k_\theta(\theta - \theta_0)^2 \tag{1.8}$$

$$E_{impropers} = \sum_{impropers} k_\xi(\xi - \xi_0)^2 \tag{1.9}$$

$$E_{dihedrals} = \sum_{dihedrals} \left(\frac{V_1}{2}[1 + \cos(\phi - \phi_1)] + \frac{V_2}{2}[1 - \cos(2\phi - \phi_2)] + \frac{V_3}{2}[1 + \cos(3\phi - \phi_3)] \right) \tag{1.10}$$

$$E_{nonbonded} = \sum_{i>j} f_{ij} \left(\frac{A_i j}{r_{ij}^{12}} - \frac{C_i j}{r_{ij}^{12}} + \frac{q_i q_j e^2}{4\pi\varepsilon_0 r_{ij}} \right) \tag{1.11}$$

where r, θ, ξ, and ϕ are the bond lengths, bond angles, improper dihedral angles, and torsional dihedral angles. The variables with the 0 subscript are the reference or ideal values and $A_i j$, $C_i j$, q_i, and q_j are the parameters of the force field. Generally all interactions have a harmonic functional form, except for the torsional dihedral-angle term which has a trigonometric form. The label K indicate force constants.

In molecular dynamics simulation, we use the above described potential to the evolution of atomic coordinates in time. A trajectory is generated consisting of positions and velocities. In order to propagate the atomic coordinates, an integration of Newtons second law [19] is used

$$m\frac{\mathrm{d}^2 r}{\mathrm{d}t^2} = -\nabla E(r) \tag{1.12}$$

where m denotes the atom's mass and $-\nabla E(r)$ the conservative force on the particle obtained from the force field. In our simulations the equation is solved numerically

iteratively using Verlet algorithm [20]. This would produce an ensemble with a fixed number of particles, a constant volume, and constant energy. Since experiments are rather carried out under constant pressure or temperature, it is also possible to generate these ensembles by applying methods that keep pressure and temperature constant [21–27].

Chapter 2

Incorporation of hydroxyl groups

The state of the art in polymeric capacitor films is metallized biaxially oriented polypropylene (BOPP), with an energy storage density of 2.2 J/cc [9, 10]. Metallized BOPP has the unique combination of fast response, low loss, good clearing, and high breakdown field in the range of 700 V/μm for small areas. Any improvement to polypropylene (PP) would require an increase in relative permittivity and/or breakdown strength while preserving low loss. While the obvious strategy of adding polarizable groups to PP does increase its relative permittivity, the slowed down dynamics of most polar groups also produces increased dielectric loss in the range of frequencies relevant to power electronics. The improvement of the dielectric properties of PP has thus remained an open challenge in this field.

Recent experimental studies indicate that the covalent addition of a small amount (2–6 mol%) of –OH groups to isotactic PP chains alleviates these difficulties. Indeed, it was found that the addition of these hydroxyl groups causes a significant increase in the static relative permittivity and breakdown strength of the polymer while still maintaining a relatively low dielectric loss (Figure 2.1) [28]. While the origins of these results have been attributed to the high crystallinity of PP coupled to a unique hydrogen bonding network structure caused by the –OH groups, little

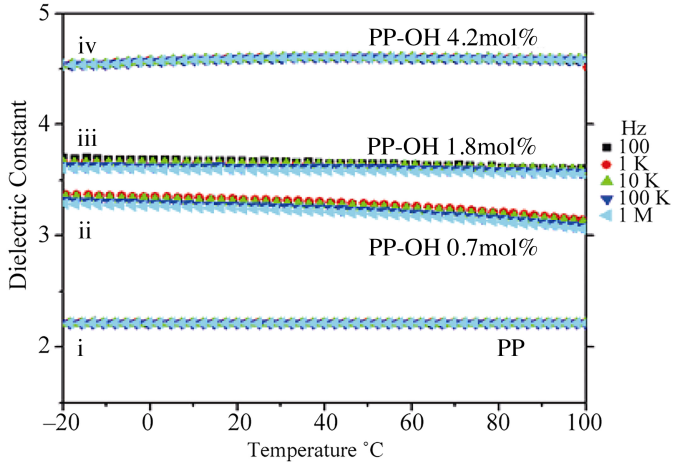

a)

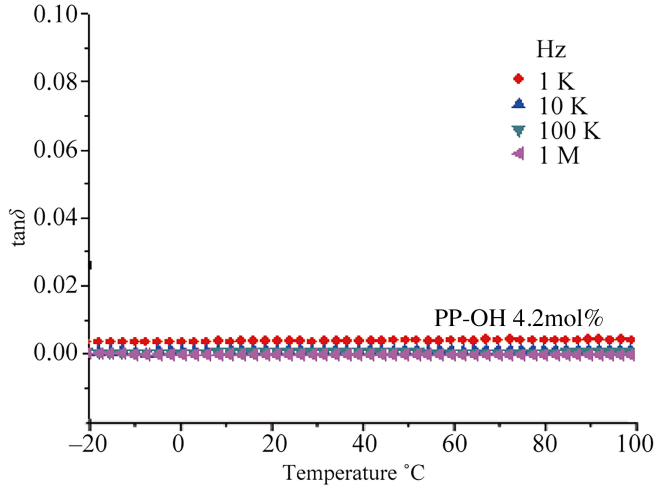

b)

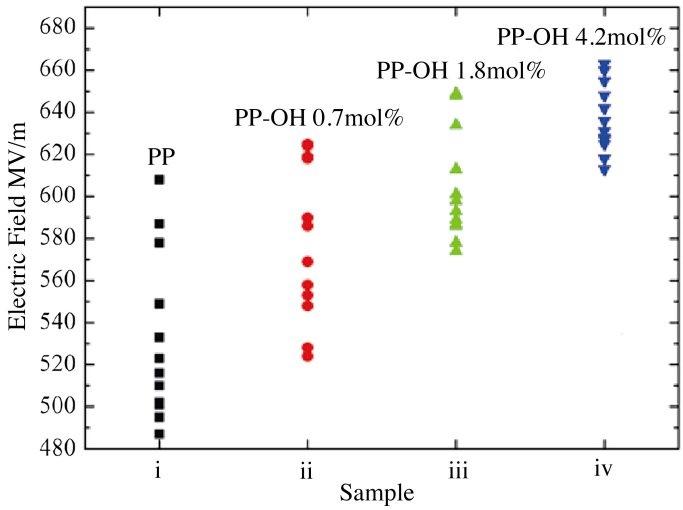

c)

Figure 2.1: (a) Relative permittivity, (b) dissipation factor , and (c) breakdown strength for (i) PP and three PP-OH copolymers containing (ii) 0.7, (iii) 1.8, and (iv) 4.2 mol% OH content

understanding exists of these unusual phenomena at a molecular level. Probing these molecular processes through the aid of large scale molecular dynamics simulations, in conjunction with experimental findings, is the primary focus of this chapter of the dissertation.

While the crystallization of PP is hard to simulate [29], polyethylene (PE) crystallizes readily even during typical MD simulations [30–36]. So, from a simulation point of view, it makes sense to focus on copolymers of PE. We are further guided to this choice since experimental dielectric storage and loss results for PP–OH, and new results for PE–OH, both of which behave similarly (Figure 2.2), support the apparent generality of our assertion that the addition of –OH groups to a nonpolar hydrocarbon chain serves to increase its static relative permittivity without simultaneously increasing loss.

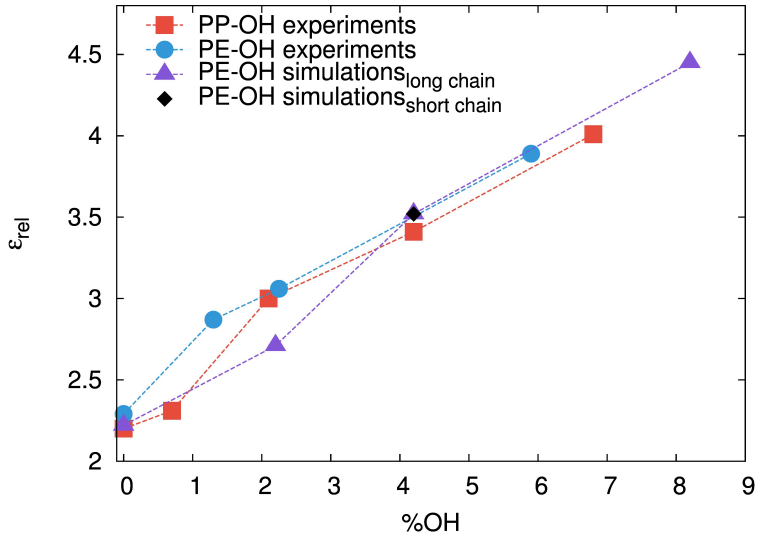

Figure 2.2: Static relative permittivity, ε_{rel}, comparison of PP–OH and PE–OH. The simulation values are derived as discussed in the text.

We begin by discussing the two relevant set of experiments and follow up with

our simulations. For the experimental investigation of the dielectric properties of PE, our collaborators synthesized random copolymers PE-OH with varying –OH concentration of 1.30, 2.25, and 5.90 mol% [37]. The relative permittivity of these dried thin samples was measured by a HP multifrequency LCR meter in the frequency range of 100 Hz to 1 MHz at room temperature (Figure 2.2). In addition to results on PE-OH, our collaborators also measured the relative permittivity for PP-OH samples which were described by Chung et .al. [28]. The PP–OH results shown in Figure 2.2 are different from the earlier published results. The previous results corresponded to samples whose water concentrations were not carefully controlled. To drive out water that is not tightly bound to the polymer, we stretched the films biaxially and then dried them at 110C for 12 h. The water content in the samples was measured by differential scanning calorimetry. For a 1.2 mol% -OH sample, it was found to decrease from 1.19 wt% to 0.32 wt% upon drying. Evidently, some fraction of the water is held tenaciously by the polymer, presumably through hydrogen bonds with the –OH groups on the PP chains.

The results (Figure 2.2) for the static relative permittivity of PP–OH as a function of –OH content are in good agreement with the PE-OH data. The measured static relative permittivity was found to increase with increasing –OH content. This data also follows the same trend as those of PP-OH without the drying step [28], but the static relative permittivity measured from the dried samples are systematically lower. While the excess water in PP-OH also apparently increases the relative permittivity without substantially increasing the loss, we consider that this result is likely not stable, so that the water content would reduce to a plateau value with time. Figure

2.3 shows that the loss for PP-OH remains low except in the very low frequency regime.

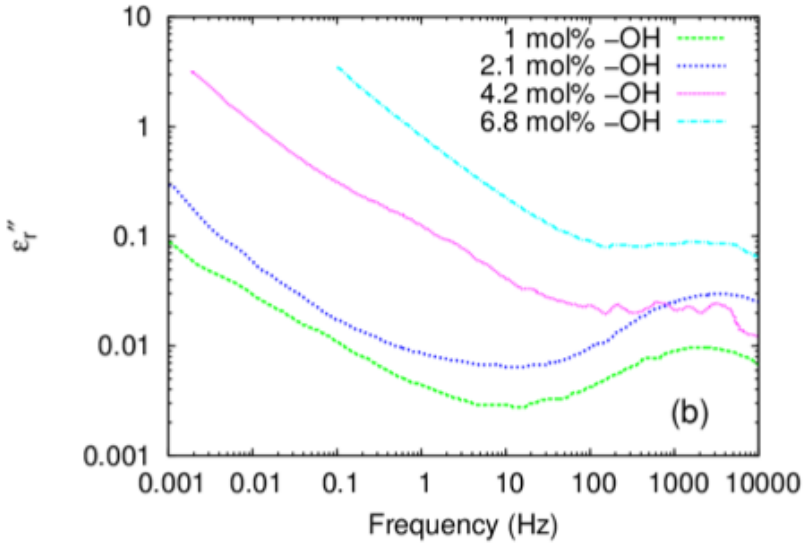

Figure 2.3: Frequency dependence of the dielectric loss ε''_{rel} for the PP-OH samples which have been dried.

2.1 Short Chain Polyethylene

In our simulations, we used the Optimized Potentials for Liquid Simulations–All Atom force field (OPLS–AA). Although many force fields exist for PE, the generic nature of the OPLS–AA formalism lends itself to a wide variety of polymeric systems [15]. Polarizable force fields could be used for greater accuracy, but we use a non-polarizable force field due to its computational expediency. Since the non-polarizable force field simulations are expensive, we exploit general-purpose graphical processing units (GPGPU) to accelerate the van der Waals and long-range Coulombic calculations [38, 39], as implemented in LAMMPS [40].

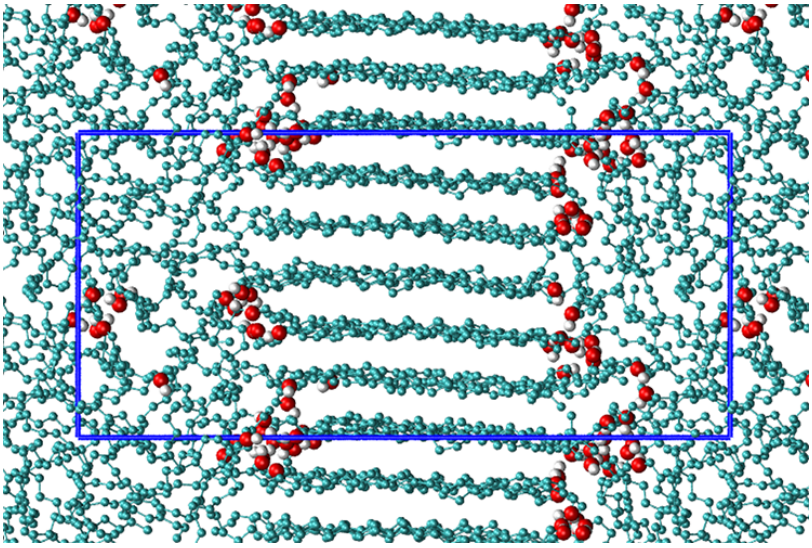

Figure 2.4: Simulation snapshots of 4.2 mol %PE–OH, 64 chains of containing 21 carbons each. Each chain is terminated by either –OH or $–CH_3$. Oxygens and hydroxyl hydrogens are shown as red and silver spheres respectively. The blue box marks the central simulation box of the periodic boundary conditions.

To understand the mechanism, we start with short chain simulation of substituted polyethylene. We generated 64 chains of polyethylene composed of 21 CH_2 groups each. Out of the 128 termination sites, we randomly selected 114 sites and terminated them with –OH. The rest of the 14 sites were terminated using CH_3, consequently generating a 4.2 mol % PE–OH. This concentration of –OH in the system is similar to the concentration –OH in the PP–OH experiments. The chains are then allowed to equilibrate at an unrealistic high temperature of 1000K for 5 ns to produce an amorphous system. The system is cooled down to the 500K at a rate of 25 K/ns. It is then further allowed to equilibrate at 500K for 5 ns to generate an amorphous system with a density of 0.77 g/cm^3. The temperature is reduced by 10K and then it is again equilibrated again at 490K for 1 ns. The same method of step cooling of 10 K/ns is applied until the system reaches 300K. At 300K the system is then allowed

to relax for 5ns. The figure 2.4 shows the snapshot of this system at 300K. As seen in the figure, the structure looks semi–crystalline in nature. Further to compare the structure to experiments, we look at the top view of the crystalline part of the polyethylene (Figure 2.5). We find the crystalline structure to be orthorhombic in nature ($\alpha = \beta = \gamma = 90$), as seen in experiments [41]. We also calculate the lattice constant of this orthorhombic lattice and find $a = 7.55$Å and $b = 5.06$Å which is comparable to lattice constant $a = 7.4$Å and $b = 4.94$Å obtained using XRD [41].

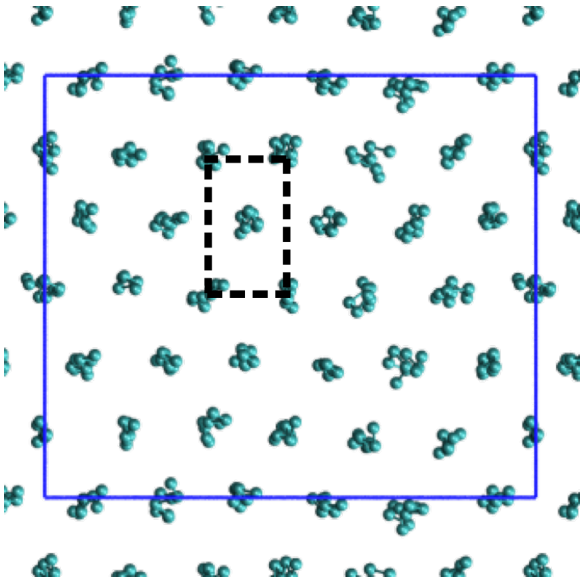

Figure 2.5: Top view on crystalline part of polyethylene.

Since the system is similar to an experimentally obtained system, we use it to calculate the static relative permittivity. To calculate the relative permittivity, the net dipole moment was of the system was sampled under NVT conditions for 20ns. The static relative permittivity is computed [42, 43] as

$$\widetilde{\varepsilon}_{rel} = \varepsilon_{\infty} + \frac{4\pi < M^2 >}{3Vk_BT} \tag{2.1}$$

where M is the dipole moment of the simulation box, k_B is Boltzmanns constant, T is the temperature, V is the simulation volume, and ε_∞ is the constant that accounts for the electronic component which is not included in the classical MD calculations. The calculated $\widetilde{\varepsilon}_{rel}$ for the system is $\widetilde{\varepsilon}_{rel,xx} = 3.67$, $\widetilde{\varepsilon}_{rel,yy} = 3.6$, and $\widetilde{\varepsilon}_{rel,zz} = 3.3$ in the 3 orthogonal directions. Hence, the average relative permittivity is $\widetilde{\varepsilon}_{rel} = 3.52$ (Figure 2.2), which agrees with the values estimated for the experiments. Note that in the simulation there were some assumptions made that may be unrealistic in nature. Considering –OH as the terminating groups might not be accurate since, experimentally they were found to be pendant/side group. The bias was created to force the –OH out of the crystalline structure, thus maintaining the high crystallinity in the system. Although the static relative permittivity calculated from the simulations seems reasonable, this method will not replicate the decrease in crystallinity with the increase of the hydroxyl content in the material, as seen in experiments [28, 37]. Thus, we simulated a single long chain of polyethylene, where the –OH are randomly substituted as a side group in the system.

2.2 Long Chain Polyethylene Crystallization

We recognize that having a semi-crystalline structure is crucial for mimicking a simulation. We know the rate of cooling can play a critical role in crystallization [44, 45]. Therefore, we examine different annealing techniques in our simulations to develop a reliable and computationally inexpensive "annealing" procedure. We analysis two flavors of cooling: step cooling and continuous cooling. In step cooling,

we decrease the temperature by a small amount after every nanosecond and then let the system equilibrate at that temperature for a nanosecond before modifying the temperature again (Figure 2.6a). Continuous cooling is very similar to step cooling as well where the step size of the change in temperature is 10 picoseconds (Figure 2.6b).

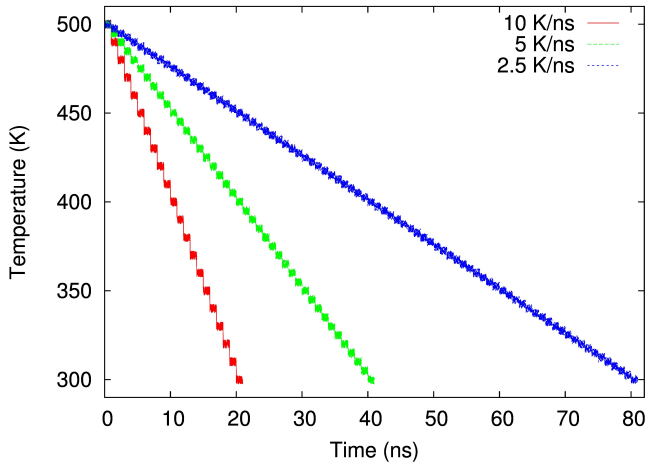

a)

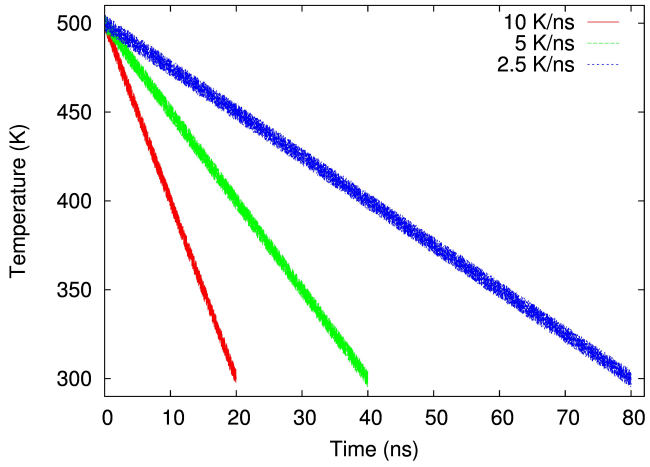

b)

Figure 2.6: Temperature control for cooling from 500 K to 300 K by (a) step and (b) continuous process during the simulation.

We created a single long polyethylene chain made of 3200 methyl (–CH_2–) units.

Method	Cooling Rate (K/ns)	Crystallinity %
Step	2.5	65±2
Step	5	61±2
Step	10	57±2
Continuous	2.5	66±2
Continuous	5	65±2
Continuous	10	59±2

Table 2.1: Effect of cooling rate on crystallinity of polyethylene.

An amorphous structure of the system is produced by heating it at 1000 K for 5 ns under NPT ensemble. Once the system is equilibrated (volume stabilizes) at that temperature, the temperature is then lowered in a continuous manner to 500 K in 10 ns. The system is again allowed to equilibrate at 500 K for 2 ns. We use this final structure as the initial seed for the annealing procedure analysis. We test the both of the mentioned cooling techniques (i.e. step and continuous) by cooling the samples from 500 K to 300 K at a cooling rate of 10 K/ns, 5 K/ns and 2.5 K/ns. The final structure obtained seems to be highly crystalline visually. However, a systemic quantitative analysis is required to differentiate the crystallinity between each sample. Consequently, we use a site order parameter for quantifying the crystallinity. In the sample, each carbon is assigned a bond orientation unit vector, which is calculated by connecting the midpoints of its two adjacent backbone bonds [31]. The bond order parameter between the ith atom and the jth atom is given by

$$A = \frac{3 < \cos^2\theta > -1}{2} = \frac{3 < (\overrightarrow{b_i} \cdot \overrightarrow{b_j})^2 > -1}{2} \tag{2.2}$$

where a_i and b_i are unit orientation vectors of the respective atoms. The order

parameter for a carbon site is calculated by averaging the bond order parameters for all carbons within a radius of 0.7 nm [46]. A carbon with a local order parameter of more than 0.62 was considered crystalline. The calculated crystallinity for each sample is shown in Table 2.1. We observe that in general with a decrease in the cooling rate the crystallinity increases. Furthermore, continuous annealing produces a higher crystalline system. However, the method of annealing does not depend on the cooling rate when the rate is 2.5 K/ns suggesting that it is the maximum crystallinity feasible from the simulations. The same crystallinity is also obtained at a lower cooling rate (faster simulation) of 5 K/ns using continuous annealing method. Henceforth, we will use this annealing technique for all mentioned simulations in this dissertation. The snapshot of the structure at 300 K using this technique is shown in the figure 2.7.

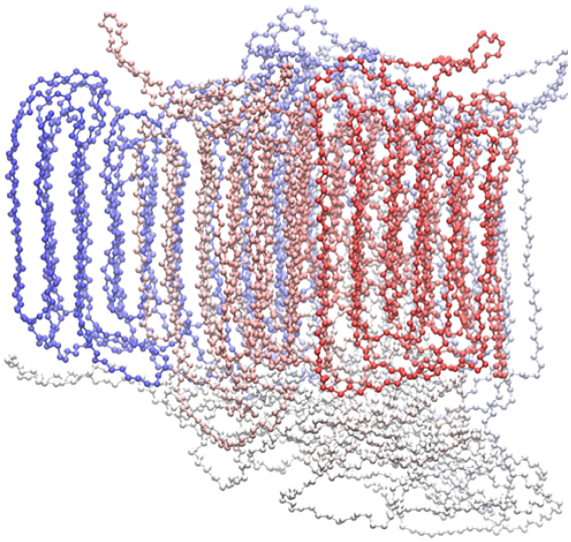

Figure 2.7: Semi-crystalline polyethylene constituting of 3200 backbone carbons at 300 K continuous cooled at a rate of 5 K/ns from 500 K where it was a melt. The carbons are colored by their index number.

2.3 Addition of hydroxyl group

As discussed in Section 2.1 we bias the insertion of –OH in the amorphous phase by adding them to the end of the short chain. In this section, we study the difference between randomly substituted –OH and preferentially substituted –OH to amorphous phase. We use the semi-crystalline polyethylene (single chain, 3200 carbons) at 300 K, generated using continuous cooling from 500 K at a rate of 5 K/ns. Using the local order parameter discussed above we classify carbon as either crystalline or non-crystalline (amorphous). We selected 64 amorphous carbons randomly and substituted one of the hydrogens with a hydroxyl group, thus creating a sample comparable to the sample generated in Section 2.1. The system is then equilibrated at 300 K for 10 ns. The final obtained the structure in shown in Figure 2.8a. For comparison, we also generate a sample where –OH are randomly substituted. We take the amorphous polyethylene (single chain, 3200 carbons) at 500 K and randomly select 64 carbons where one of the hydrogens is replaced with a hydroxyl group. The sample is then cooled to 300 K at a rate of 5 K/ns and equilibrated for 10 ns. The final obtained structure at 300 K is shown in Figure 2.8b .

The static relative permittivity for the two samples was computed (using Equation 2.1) by sampling the net dipole moment under NVT conditions for 20ns. The static relative permittivity for biased and randomly substituted –OH was found to be 3.53 and 3.52 respectively. The relative permittivity for both systems is similar and is in good agreement with experimental observation (Figure 2.2). However, on calculating the crystallinity of the samples and we observe the crystallinity of the sample where

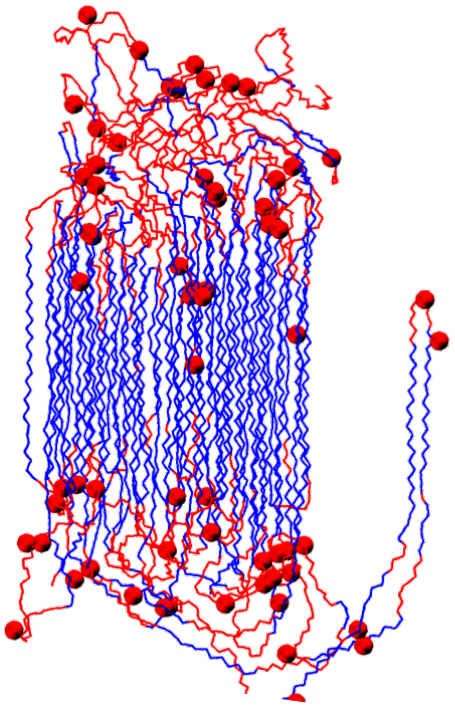

a)

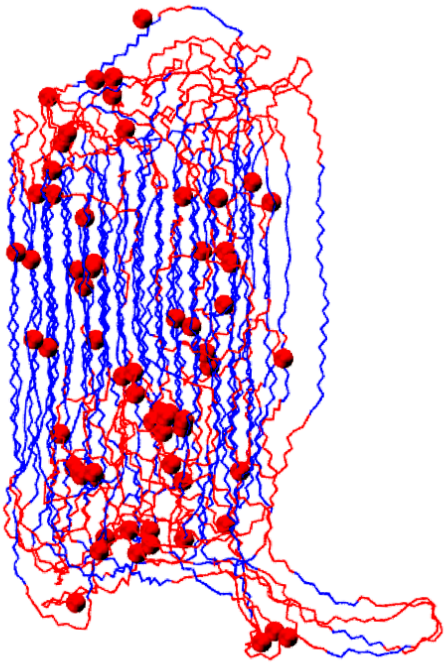

b)

Figure 2.8: Snapshot of 4 mol% semi-crystalline PE–OH at 300 K where –OH were substituted in (a) amorphous region or (b) randomly. The red section of the chain is amorphous, while the blue component is crystalline.

–OH were replaced in amorphous regime remains unchanged (65 ± 2 %). While in the sample where the –OH were replaced randomly, the crystallinity drops to $55 \pm 2\%$. This decrease in crystallinity is also seen in experiments [28, 37] and is indicative of a random distribution of –OH in the system. Further analysis of the distribution of –OH will be done in later sections of the dissertation.

Another difference between experiments and simulations is the use of spacers on the pendant group. In the simulations, the hydroxyl group is attached to the backbone directly, but in experiments they use 5-7 methyl groups as spacers. We simulate the sample with spacers and analyze the variation in properties due to the longer side group. To simulate the PE–OH with spacers we use the amorphous PE–OH (3200 carbons) at 500 K and replace the –OH group with $(CH_2)_4$–OH. To avoid a significant change in the structure, we keep the attachment site of the side group to be identical in the two samples. The same protocol for crystallization was applied to the sample with spacer group. The final snapshot of the crystallized system with spacers is shown in Figure 2.9. The calculated crystallinity using local order parameter for the system is $61 \pm 2\%$, which is comparable to the PE–OH sample without spacers. The bigger observed difference in between the samples is in the densities of the two samples. The density for PE–OH without spacers was similar to PE system equal to 0.93 g/cc, while the sample with spacers has a density of 0.9 g/cc. Hereafter, the static relative permittivity for the sample was calculated (using Equation 2.1) by sampling the net dipole moment under NVT conditions for 20ns. The static relative permittivity for the two samples is found to be the same i.e. 3.52. This similarity in the relative permittivity was surprising as the densities of the two system were

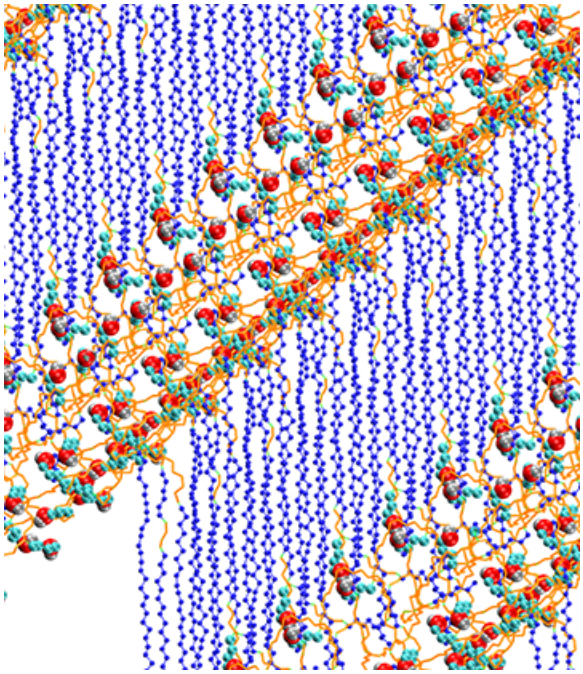

a)

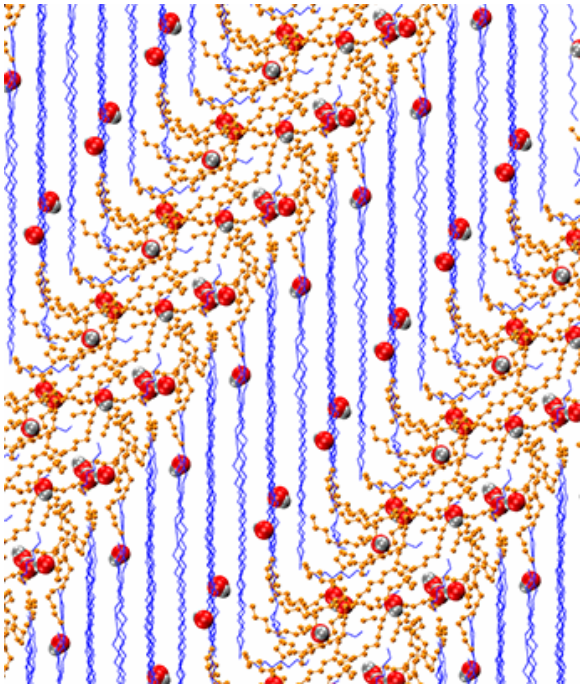

b)

Figure 2.9: Snapshot of periodic images of 4 mol% semi-crystalline PE–OH at 300 K (a) with and (b) without spacers. The orange section of the chain is amorphous, while the blue component is crystalline. Oxygens and hydroxyl hydrogens are shown as red and silver spheres respectively. Carbon used as spacers are shown in cyan. Backbone and spacer hydrogens are not shown for clarity.

found to be different. However, on further analysis, we observe that the $< M^2 >$, representing the maximum amplitude of fluctuation of the dipole is higher for the sample with spacers. The increase is due to the mobility of the spacers group, as in the sample without spacers the mobility of the –OH group is hindered.

2.4 Long Chain Polyethylene Copolymer

In Section 2.2 and 2.3 we have developed and compared simulation technique. In this section, we will use them to study the reason behind the increased dielectric properties of PE–OH. A single polyethylene chain with 1000 backbone carbon atoms was equilibrated at 500K and 1 bar, where it is in a molten, amorphous state. Samples with 2.2 mol%, 4.2 mol% and 8.2 mol% –OH groups (i.e., 11, 21, and 41 groups per chain, respectively) were prepared using the last configuration of the pure PE simulation run, by directly bonding –OH groups to randomly selected carbons on the polymer backbone, replacing one of the H atoms. These –OH contents closely parallel the functionalization levels realized in both the PE experiments reported here and PP experiments reported previously [28]. The systems were cooled from 500K to 300K at 5K/ns under isobaric conditions. The volume was allowed to stabilize at 300K for 40∼50ns, followed by 5∼6ns equilibration in the canonical (NVT) ensemble. Thereafter, the net dipole moment was sampled under NVT conditions for 50ns for calculation of static relative permittivity.

Configuration snapshots of PE chains with various levels of -OH content are shown in Figure 2.10. Visually, crystallinity remains high for the 2.2 and 4.2 mol% samples,

but is significantly decreased for the 8.2 mol% sample. To quantify crystallinity we again use the local order parameter (Equation 2.2) and we find that pure PE is 65±2% crystalline, while PE–OH samples with 2.2, 4.2, and 8.2 mol% OH are 56±3, 57±2 and 32±2% crystalline, respectively. The trend in crystallinity is qualitatively similar to the PE–OH experimental results [28, 37]. The mobility of the polar groups is influenced by the surrounding environment, so we classify each –OH group as belonging to the crystalline, amorphous, or interphase region according to the backbone carbon atom that it is bound to (Table 2.4). Note that a very high fraction of the –OH groups are in interphase, probably reflecting Flory's notion that these "defect" groups are rejected from the crystal. This segregation gives them more mobility for reorientation, which increases the static relative permittivity.

	Amorphous	Crystalline	Interphase
2.2	0.12	0.01	0.87
4.2	0.14	0.10	0.76
8.2	0.26	0.02	0.72

Table 2.2: Fraction of –OH groups in the amorphous, crystalline and interphase regions. A carbon with local order parameter of more than 0.62 was considered crystalline, less than -0.12 was considered amorphous, and interphase otherwise.

	$< M^2 >$	$< M >^2$	$< M^2 > / < M >^2$
2.2	0.49	0.14	0.29
4.2	1.23	0.45	0.37
8.2	2.08	1.18	0.57

Table 2.3: Dipole moment and static relative permittivity for PE–OH system with varying amounts of –OH

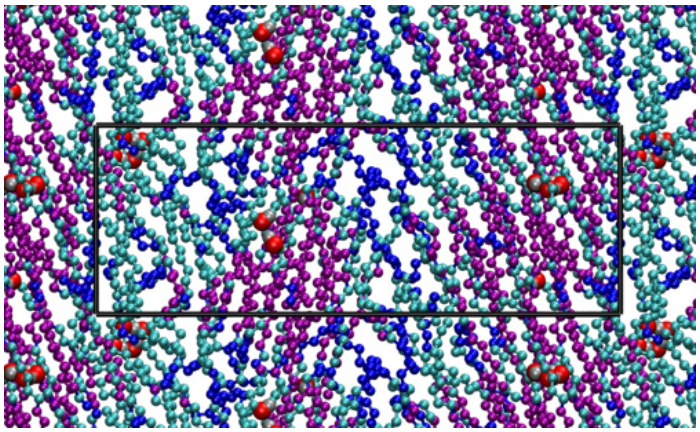

a)

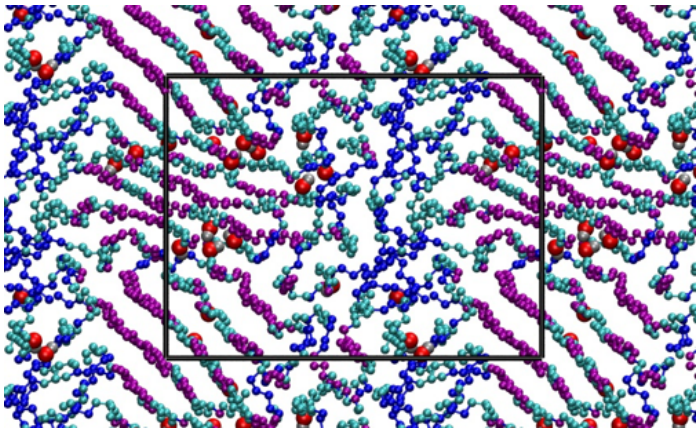

b)

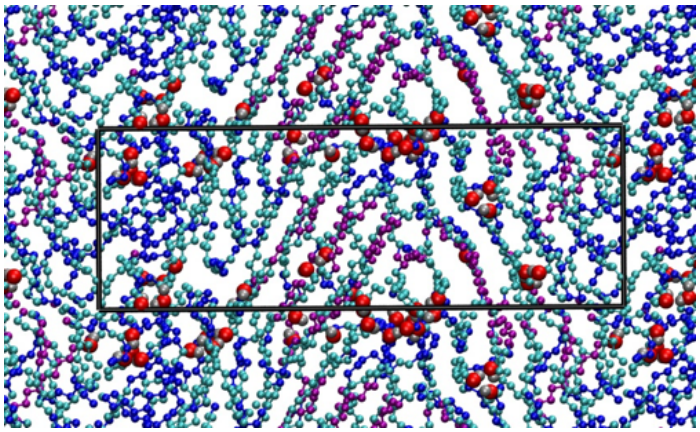

c)

Figure 2.10: Simulation snapshots of (a) 2.2 mol %PE–OH, (b) 4.2 mol% PE–OH and (c) 8.2 mol% PE–OH. Oxygens and hydroxyl hydrogens are shown as red and silver spheres respectively. Crystalline, interphase and amorphous carbons are shown in purple, cyan, and blue, respectively. Backbone hydrogens are not shown for clarity. The black box marks the central simulation box of the periodic boundary conditions.

2.5 Static Relative Permittivity

We calculate the static relative permittivity for the above systems using Equation 2.1, the calculated $\widetilde{\varepsilon}_{rel}$ obtained, shown in Table 2.4, for 4.2mol% PE–OH is in good agreement with the value obtained from experiments (Figure 2.2). However, the system was found to have a remnant dipole moment over the simulation timescale of 100ns. In particular, this unrelaxed part at 100ns for 2.2, 4.2 and 8.2mol% –OH was found to be 29, 37, and 57%, respectively expressed as the ratio (Table 2.4). Two salient points are emphasized here. First, for melts of PE–OH at T = 500K, relaxes to zero over this simulation timescale. Second, a detailed examination of our simulations shows that the –OH groups that are accidentally incorporated in the crystal domains relax over timescales shorter than 100 ns. Thus, this unrelaxed dipole moment is not due to constraints from the crystal. Rather, we conjecture that they are from hydrogen bonding interactions that do not decay over the 100ns timescales accessible in the simulations. A corollary to this statement is that the relaxations of these H–bonded interactions should give rise to large dielectric losses at timescales longer than 100ns. Since our experiments show low dielectric loss, some other phenomemon is at play here. In particular, we conjecture that these differences are caused by the presence of the small amount of "bound" water in both the PE–OH and PP–OH samples.

To examine the presence of water, we chose the 4.2 mol% PE–OH system for further study, to which we added varying amounts of water in a series of simulations. The water molecules were described by the transferable intermolecular four-point

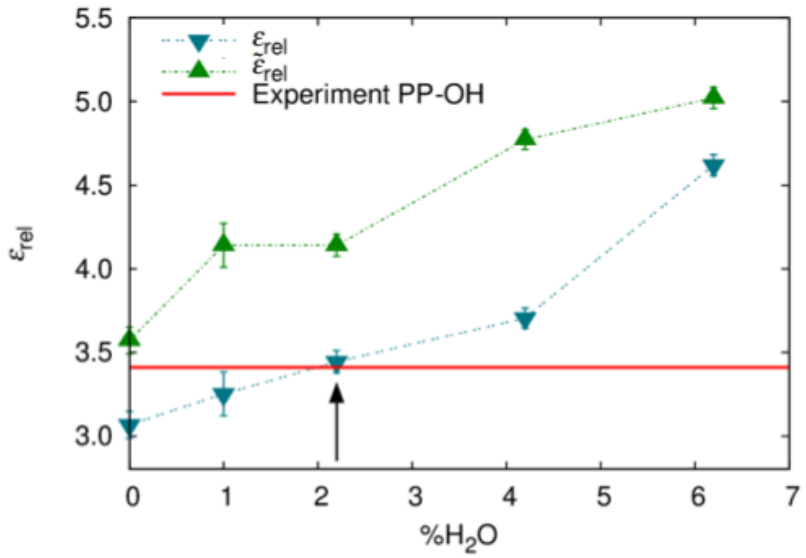

Figure 2.11: PEOH as a function of added water, calculated using two different methods. Green triangles are $\widetilde{\varepsilon}_{rel}$ (eq 2.1), while blue inverted triangles are ε_{rel} (eq 2.3). The red line represents the static relative permittivity measured for the 4.2 mol% PP-OH.

potential (TIP4P) model [47], and were added randomly to the last configuration of the 4.2 mol% PE–OH simulation at 300K. Each system was heated to 500K and then cooled to 300K using the same protocol as for the dry PE–OH simulations. The addition of water causes a significant increase in relative permittivity which overpredicts the experiments (Figure 2.11). The definition of Equation 2.3 assumes that the net dipole moment relaxes completely at long time, but there exists another quantity, [48]

$$\varepsilon_{rel} = \varepsilon_{\infty} + \frac{4\pi\left(< M^2 > - < M >^2\right)}{3Vk_BT} \tag{2.3}$$

whose latent assumption is that the remnant dipole moment never relaxes, and thus does not contribute to the static relative permittivity. This assumption is compatible with the experimental observation that these materials have low loss in

the experimental timescale. This curve for$\widetilde{\varepsilon}_{rel}$ is also plotted in Figure 2.11, and is systematically lower than that for ε_{rel}. We note that there exists a finite water content at which ε_{rel} agrees with experiment, but the actual water content must be characterized to establish this point of agreement.

2.6 Water Content

We consider two ways to characterize the water content from the simulations. First, we pursue an analysis based on hydrogen bonding. Later, a more extensive calculation based on dielectric loss will support the same conclusions. A key to the analysis is the distinction between free and bound water. We consider a water molecule to be bound if it is connected to a hydroxyl group by at least one hydrogen bond, and free otherwise. Hydrogen bonds are defined according to the standard procedure with a cutoff distance of 0.3 nm and a cutoff angle of 30° [49, 50]. We find that the amount of bound water increases with increasing water content up to ∼2.2 mol%, beyond which this bound population reaches a plateau while the free population continues to grow (Figure 2.12). We therefore conclude that all additional water molecules beyond this plateau join the population of free water, and we expect that further addition of water will eventually lead to macroscopic phase separation between a pure water phase and a PEOH phase with adsorbed water. We define the plateau concentration of 2.2mol% as the equilibrium water content in this sample. This concentration corresponds to a ratio of ∼0.5 water molecules per hydroxyl group. This is in good agreement with the experimental measurements, where the 0.32wt% water content in the 1.2mol%

–OH sample corresponds to a ratio of 0.41 H2O/–OH. The plateau concentration also identifies the point at which ε_{rel} agrees with the experiment (Figure 2.11). The implications of this agreement will be addressed in later sections.

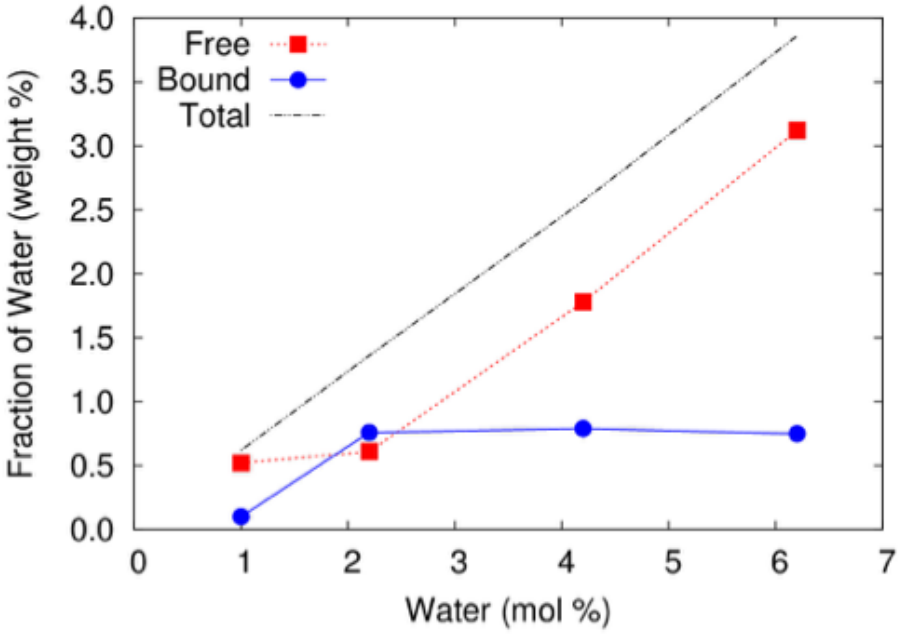

Figure 2.12: Weight percentage of free, bound, and total water in the system as a function of water in 4.2 mol% PEOH.

2.7 Dielectric Loss

In the previous section, the fluctuation of the system dipole moment was used to calculate the static relative permittivity. Here, we use the related autocorrelation function to calculate the dielectric loss as a function of frequency, but we can only access frequencies within the timescale of the simulation. We calculate the dipole correlation function (DCF) as [43]

mol% –OH	A	$\tau(ps)$	α	ε''_{max}	ω_{max} (Hz)	τ_{avg} (ps)
2.2	0.64	26	0.57	0.08	3.0E+10	33
4.2	0.73	20	0.45	0.16	3.7E+10	27
8.2	0.73	19	0.44	0.18	3.8E+10	26
mol% H_2O						
1	0.66	8.1	0.35	0.14	8.3E+10	12
2.2	0.75	14	0.37	0.20	4.9E+10	20
4.2	0.89	2.8	0.33	0.27	2.4E+11	4.2
6.2	1.00	1.3	0.25	0.44	4.8E+11	2.1

Table 2.4: Mean relaxation time and fitting parameter for dipole correlation function using stretched exponential form for PE–OH systems with varying –OH and water concentrations.

$$\Phi(t) = \frac{< \overrightarrow{M}(0) \cdot \overrightarrow{M}(t) > - < \overrightarrow{M}(0) >^2}{< M^2 > - < M >^2} \tag{2.4}$$

where $\overrightarrow{M}(t)$ is the dipole moment at time t (Figure 2.13), which we fit with a stretched exponential form with a prefactor: $\Phi_{fit}(t) = A\exp[-(t/\tau)^\alpha]$. The prefactor represents a very fast initial decay of strength $1 - A$.

The fitted function (Table 2.7) was Fourier-transformed to calculate the complex dielectric permittivity,$\varepsilon^*(i\omega) = \varepsilon'(\omega) - i\varepsilon''(\omega)$, as a superposition relation is given by

$$\frac{\varepsilon^*(\omega)}{\Delta\varepsilon} = \int_0^\infty e^{i\omega t} \frac{\mathrm{d}\Phi(t)}{\mathrm{d}t} \mathrm{d}t \tag{2.5}$$

whose imaginary part is the dielectric loss (Figure 2.14). The average relaxation time was calculated as $\tau_{avg} = 1/\omega_{max}$ [51], where, ω_{max} is the angular frequency of the peak $\varepsilon''(\omega)$.

In the dry PE–OH system we observed that the relaxation time remains constant while the dielectric loss increases with increasing –OH content. The addition of 1.0

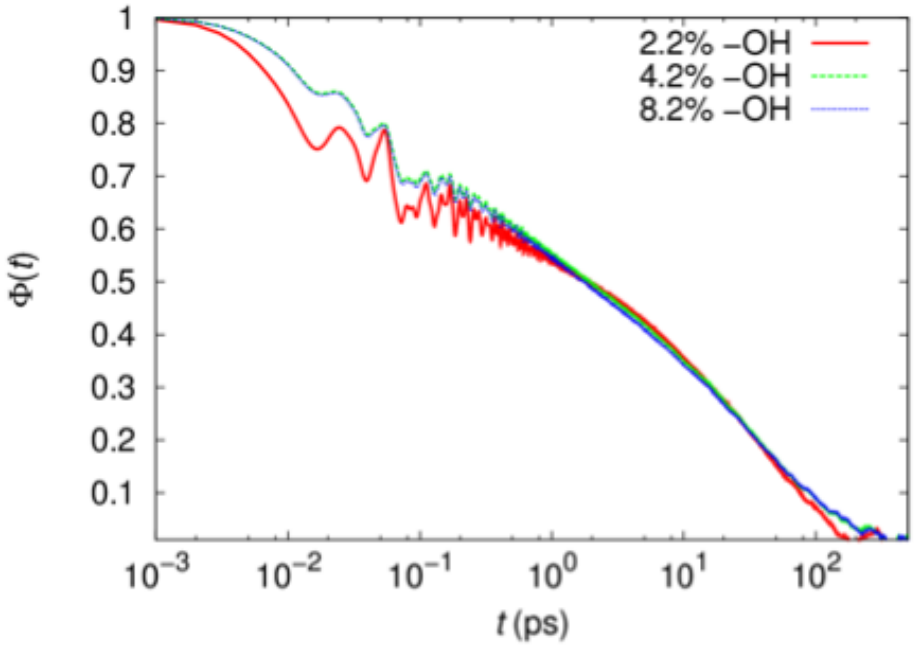

a)

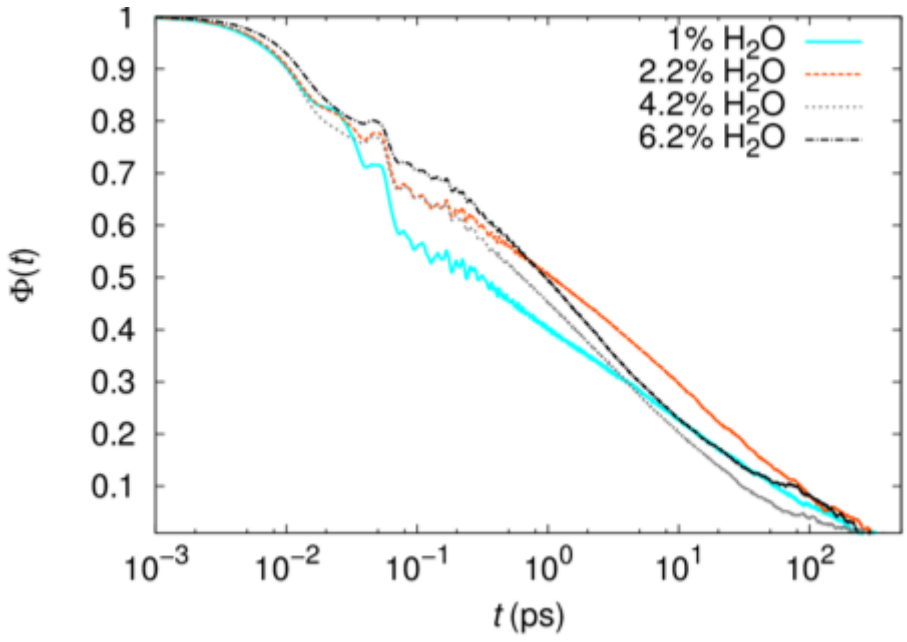

b)

Figure 2.13: Dielectric Decay Function for (a) PE–OH systems with varying –OH concentrations and (b) 4.2mol% PE–OH system with varying water content.

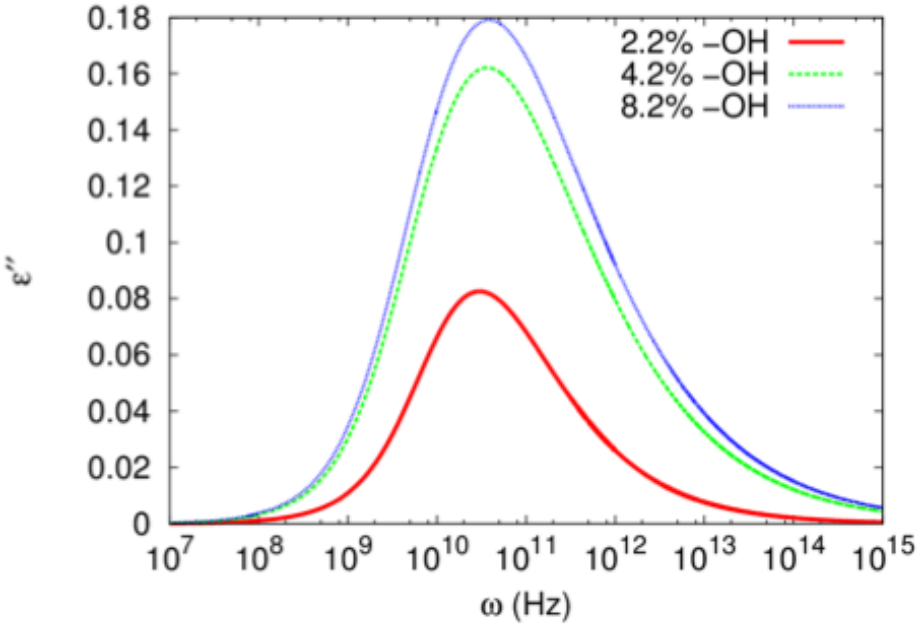

a)

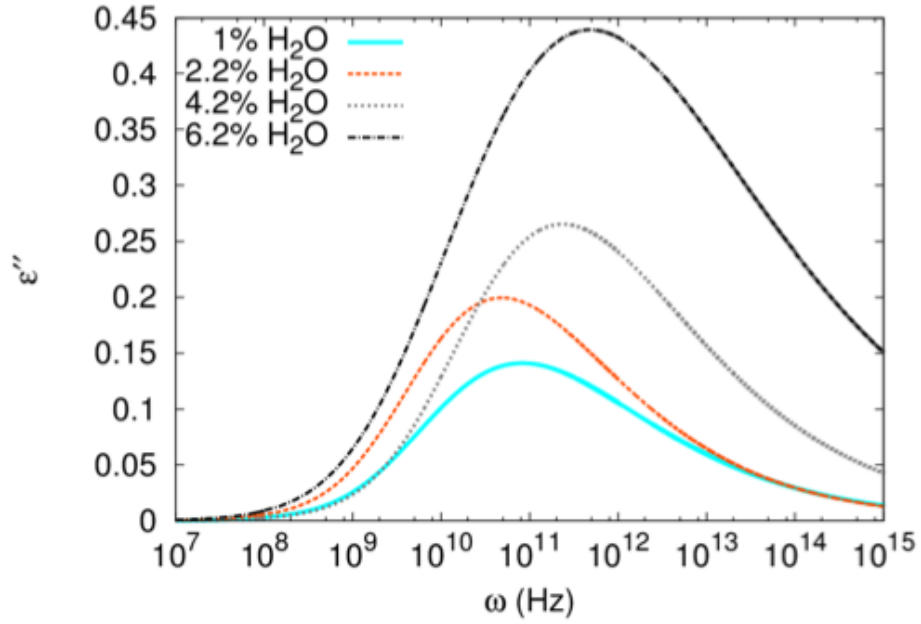

b)

Figure 2.14: Dielectric loss ε'' for (a) PE–OH systems with varying OH concentrations and (b) 4.2mol% PE–OH system with varying water content.

mol% –OH	A	τ_1 (ps)	α_1	τ_2 (fs)	α_2	$\omega_{1,max}$ (Hz)	$\omega_{2,max}$ (Hz)	$\tau_{1,avg}$ (ps)	$\tau_{2,avg}$ (fs)
1	0.30	3.7	0.57	0.08	1.0	2.0E+11	1.8E+13	5	56
2.2	0.53	8.5	0.45	0.16	1.0	8.1E+10	1.5E+13	12	67
4.2	0.49	11	0.44	0.18	1.0	6.2E+10	1.2E+13	16	83
6.2	0.32	12	0.35	0.14	1.0	5.3E+10	1.0E+13	19	100

Table 2.5: Mean relaxation time and fitting parameter for dipole correlation function for water in 4.2 mol% PE–OH system with varying water content.

mol% water to the 4.2mol% PE–OH system decreased the relaxation time from 27 ps to 12 ps. The relaxation time increased for the 2.2% H_2O system, and then decreased for systems with higher water content. This was also accompanied by a decrease in the prefactor A, which suggests that the very fast relaxation process becomes less important relative to the relaxation in the simulation timescale with increasing water content. A similar non-monotonic behavior of relaxation time was observed in simulations of polyoxyethylene diluted by water [43], and this behavior was attributed to different relaxation behaviors between free water and water bound to the polymer and to their changing relative populations with increasing water content.

To further explore the influence of water on the relaxation, we measured the dipole moment of the water molecules only and calculated their dipole correlation function (Figure 2.15a). Here, we find that DCF can be fit with sum of two stretched exponential functions:

$$\Phi_{fit}(t) = A\exp\left[-\left(\frac{t}{\tau_1}\right)^{\alpha_1}\right] + (1-A)\exp\left[-\left(\frac{t}{\tau_2}\right)^{\alpha_2}\right] \tag{2.6}$$

After the Fourier transform to find, ε'' two peaks appear at ∼12ps and ∼0.06ps (Table 2.7), which are in agreement with the two different water relaxation peaks

identified measurements of organic materials [52]. Both relaxation times obtained are much faster than the relaxation time of 4.2 mol% PE–OH sample without water (27 ps), which suggests that water accelerates the relaxation dynamics of the system. The height of the higher frequency peak increases with increasing water content, which we identify as the free water peak. In contrast, the lower frequency peak already saturates at 2.2%, which is in perfect agreement with the behavior of the bound water fraction as found through the less computationally intensive hydrogen-bond analysis. The bound water peak not only has a longer relaxation time but also has wider tail, due to lower α_1 (Table 2.7), which gives rise to increased loss at lower frequency, although the loss implied is still negligible for frequencies less than 1MHz. Though the free water has a higher loss peak, its relaxation both occurs at a higher frequency and decays more quickly with frequency, since $\alpha_2 = 1$, which corresponds to a Debye process. This implies that additional of free water will increase the static relative permittivity without increasing loss below 1MHz, which is what experiments observed.

2.8 Discussion

To summarize, we have found several points of agreement between the simulations of PE–OH with water and the experiments. The static relative permittivity, ε_{rel} and the stoichiometric ratio of water molecules to hydroxyl groups match the experiments. Additionally, the dielectric loss analysis of the water molecules only explains how additional water increases the static relative permittivity without adding loss in the

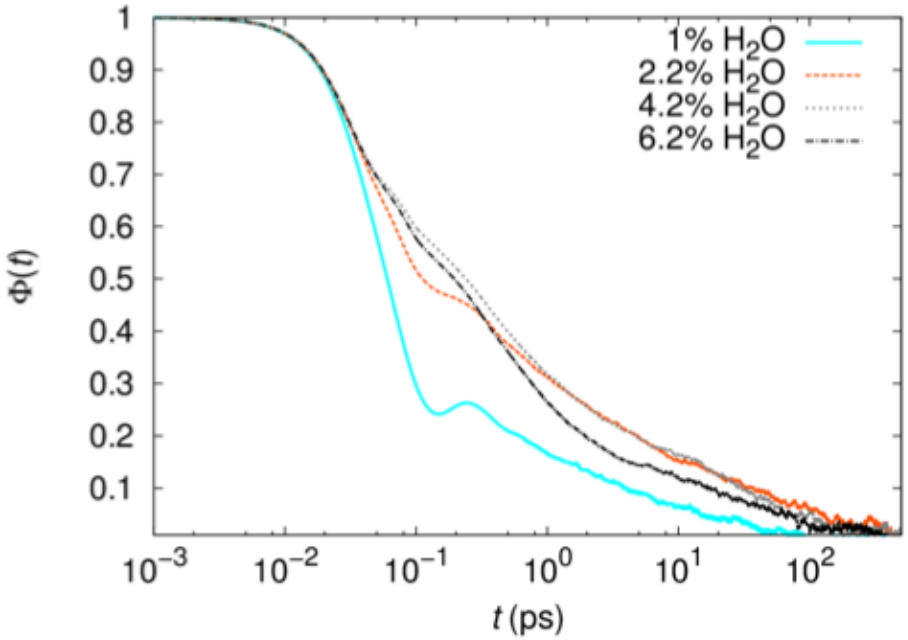

a)

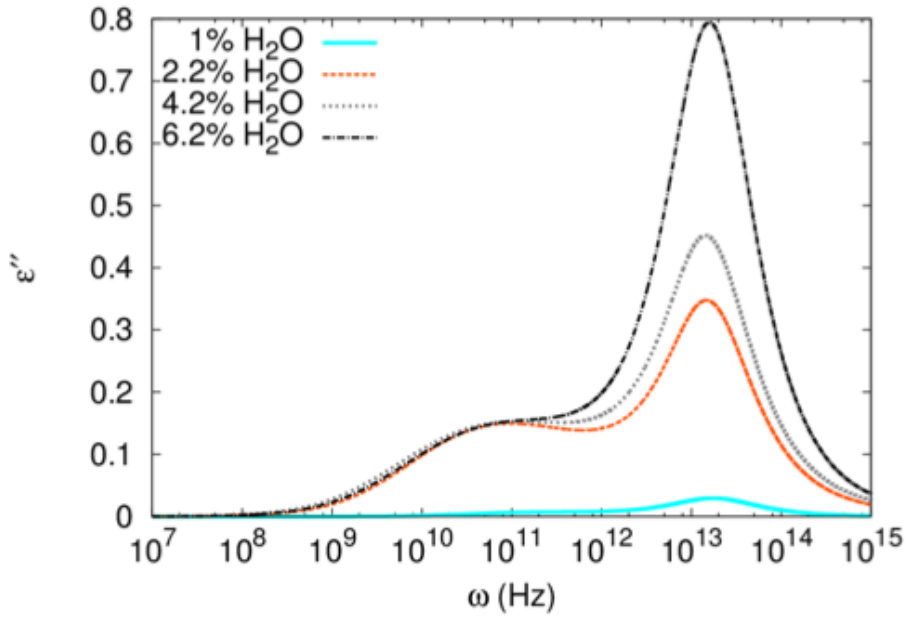

b)

Figure 2.15: (a) Dielectric Decay Function $\Phi(t)$, and (b) dielectric loss ε'' for water in 4.2mol% PEOH system with varying water content.

experimental measurement. Finally, the good agreement between the static relative permittivity ε_{rel} and experiment, combined with the formulas built-in assumptions – that the dipole moment does not relax on simulation timescales does not contribute to the relative permittivity – imply that there should be no loss in the experiments, which find the loss to be quite low.

However, we also found striking agreement in the relative permittivity between the simulations with dry PE–OH and the experiments under a different set of assumptions, namely that the system relaxes completely, so that the entire variance of the dipole moment contributes to the static relative permittivity (Figure 2.2). Although the experimental samples are known to contain a small amount of adsorbed water that was not included in the dry PE–OH simulations, we argue that the agreement is not coincidental. Specifically, we argue that the simulations are an accurate representation of what would be measured if the experimental samples could be made without any adsorbed water. This is an unproven conjecture, that remains to be verified by experiment. If this is true, it implies that two hydrogen-bonded –OH groups will relax within the experimental timescale, but when they are bridged by water, they become more strongly constrained and do not relax.

Supporting evidence in favor of this conjecture can be found by analyzing the amount of relaxation that occurs within the simulation timescale. For the 4.2mol% PE–OH system with 2.2mol% water, we separately analyzed the dipole autocorrelation of each CH-OH group (as a net neutral group of atoms), and we found that 69% of the groups were bound to one another via a bridging water molecule, while the other 31% were either single or H–bonded directly to another –OH group. We find

that those bridged by water relaxed the least while those not water-bridged relaxed the most; the Pearson correlation coefficient relating water bridging to relaxation is -0.73 suggesting a strong anti-correlation. Quantified another way, 89% of the remnant dipole at 100ns is due to water–bridged hydroxyl groups. The water in these groups are tightly bound, having a loss peak about two orders of magnitude smaller than free water.

Chapter 3

Effect of other polar groups

In the last section, the addition of a small number of polar hydroxyl (–OH) groups drastically increases the static relative permittivity of a nonpolar polymer. The critical role of hydrogen bonding and polarity has encouraged us to explore various polar side groups in this chapter. We will compare the feasibility of the incorporation of other polar groups and the accuracy of prediction methods for static relative permittivity for the samples. However, the central theme of this chapter will be to study the effect of morphology on the prediction of the static relative permittivity critically.

A particularly attractive method to predict the dielectric properties of materials is density functional theory (DFT). While this approach is very popular, its large computational requirements allow effective treatment of unit cells with just a small number of atoms in an ordered array, i.e., in a crystalline morphology. Here, by comparing DFT and Molecular Dynamics (MD) simulations on the same ordered arrays of functional polyolefins, we examine the efficiency of the two methodologies for estimating the dielectric storage modulus.

3.1 Introduction

We critically examined the assumption that underpins much of the current understanding and predictive ability of static relative permittivity. We predict the static relative permittivity of copolymer of polyethylene (PE–X) chains functionalized with a fixed amount (4.2 mol%) of different side groups (X) in a series of DFT and MD simulations. We have already studied –OH group, and we will compare it with a non-polar group $–CH_3$. Since hydrogen bonding formation was critical to increase in the static relative permittivity, we explored the group that can form strong ($–NH_2$) and weak (–SH) hydrogen bonds along with the one that cannot ($–NO_2$). Following that, we compared them with a hydrogen bond-forming group –COOH which is much larger in size.

We determined the crystal geometry for the functionalized PE using DFT. The crystal geometry obtained from DFT allowed us to calculate the static relative permittivity using density functional perturbation theory (DFPT). Thereafter, we performed two flavors of MD simulations - one in the ground state crystal structure simulated by the DFT and a second self-assembled semi-crystalline state spontaneously formed by these polymers when they are cooled from the melt to a temperature below their equilibrium melting points. The ionic static relative permittivity found in our first set of simulations are in quantitative agreement with the DFT calculations for the functionalized PE. This close agreement validates both the MD and the DFT protocols. However, the MD simulations using a semi-crystalline state yields ionic contributions to the static relative permittivitys that

are up to 10 times larger than those obtained from crystalline simulations. An equilibrium statistical thermodynamical argument suggests that this reduced static relative permittivity in the DFT calculations is a direct consequence of the fact that dipole moment fluctuations are significantly reduced in the crystalline state, while they are maximized in the amorphous state. Our results, therefore, emphasize the crucial role of polymer morphology in accurately predicting the static relative permittivitys of this commercially important class of materials.

3.2 Crystalline Polymer

Density Functional Theory

Our collaborators determine the relaxed crystal geometries of the functionalized PE using density functional theory (DFT). We started from the stable PE crystal structure with two chains stacked next to each other in a unit cell. In one of the two chains, every 4^{th} –CH_2 unit has an H atom replaced by a side group X, giving rise to the PE–X crystal (Figure 3.1). Note that the 25 mol% functionalization simulated here is much higher than typical experiments with 0.8–8 mol% functional groups. DFT, [53, 54] as implemented in the Vienna ab initio software package (VASP), [55] is applied on the starting polymer geometry. The DFT relaxation is performed using the rPW86 functional in which the DFT-DF2 vdW correction is applied [56] to capture the van der Waals interactions in the polymer correctly [57]. The projector-augmented wave (PAW) pseudopotentials [58] were applied, along with a tight energy

Table 3.1: The static relative permittivity calculated for different systems.

	$DFT_{electronic}$	DFT_{ionic}	MD_{DFT}	MD
$-CH_3$	2.45	0.02	0.02 ± 0.01	0.02 ± 0.01
–OH	2.47	0.17	0.19 ± 0.01	1.02 ± 0.02
$-NH_2$	2.49	0.07	0.05 ± 0.01	0.98 ± 0.01
$-NO_2$	2.39	0.26	0.36 ± 0.02	0.79 ± 0.03
–COOH	2.43	0.26	0.45 ± 0.03	0.48 ± 0.04
–SH	2.55	0.07	0.05 ± 0.02	0.69 ± 0.02

convergence criterion of 10^{-8} eV and an energy cut-off of 600 eV. The relaxed polymer crystal structure arrangement obtained is used as an input for a subsequent density functional perturbation theory (DFPT) [59, 60] calculation. DFPT provides us with the static relative permittivity tensor, that includes the electronic component [61] as well as the ionic (lattice) component [62]. The static relative permittivity values were obtained by determining the trace of the respective dielectric tensors. As expected, the calculated electronic contribution is found to be similar for all the polar groups. However, the ionic static relative permittivity (ε_{ionic}) is found to be different for the various functionalities (Figure 3.2, Table 3.1).

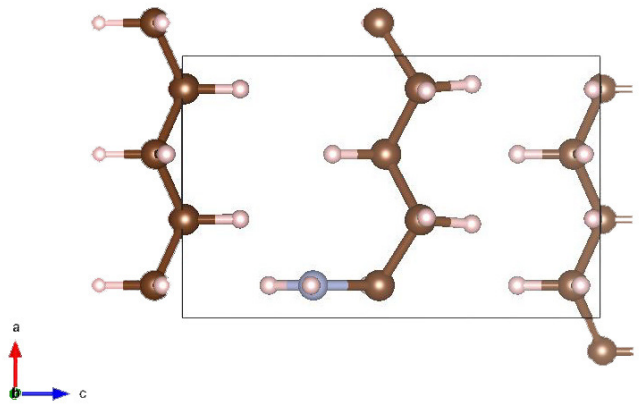

Figure 3.1: PE-X crystal structure with two chains stacked next to each other in a unit cell used for DFT.

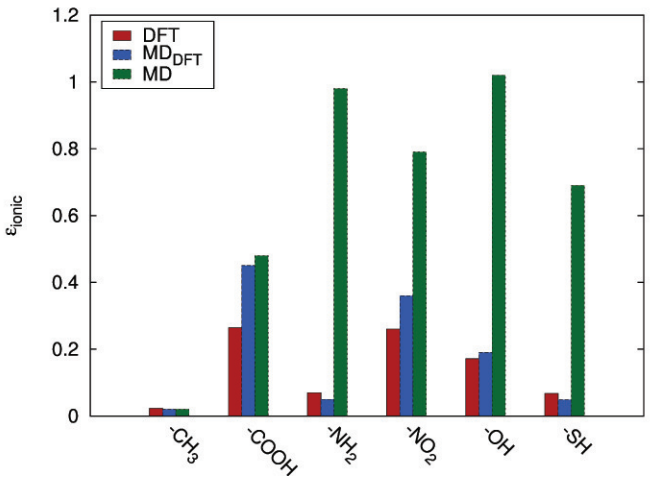

Figure 3.2: The ionic static relative permittivity of PE–X systems calculated using DFT is represented by the red histogram. The blue histogram represents the ionic static relative permittivity calculated using MD for the crystal structures obtained from DFT. The green histogram represent the ionic static relative permittivity calculated from MD for semi-crystalline system.

Molecular Dynamics

We used the DFT generated structures as the initial configuration for MD simulation using the all atom OPLS-AA force field [15]. To speed up the simulations, we exploit general-purpose graphical processing units (GPGPU) to accelerate the van der Waals and long-range Coulombic calculations,[38][39] as implemented in LAMMPS[40]. Two infinite chains of 500 carbons each were prepared using the geometry obtained from DFT. The PE–X systems obtained were then allowed to equilibrate under canonical (NVT) ensemble for 5 ns. The systems were then run for 50 ns to calculate the ionic static relative permittivity (ε_{ionic}) using $\varepsilon_{ionic} = \frac{4\pi\left(\langle M^2\rangle - \langle M\rangle^2\right)}{3Vk_BT}$, where M is the dipole moment of the system at a timestep, V is the volume, T is the temperature and k_B is the Boltzmann's constant. The ionic static relative permittivity obtained from DFT and MD simulations for these purely crystalline samples agree with each other (Table

4.1, Figure 3.2). This agreement between non-polarizable classical simulation and DFT suggests that dipole polarization contribution becomes insignificant in such a low concentration of polar groups. However, the static relative permittivity observed in experiments for PE–OH is found to be significantly larger than the predicted values[63]. We predict an ionic contribution of ≈ 0.2, which makes the total static relative permittivity ≈ 2.65 while the experiments yield values of more than 3.5. Similar results are also found for the PE–NH_2 functional group (Figure 3.3).

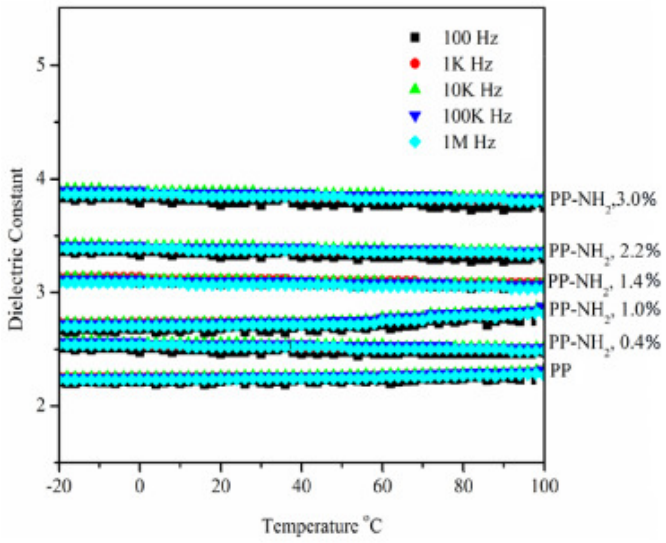

Figure 3.3: Dielectric Constant of PP–NH_2 with 1.0 , 1.4 , 2.2, and 3.0 mol% –NH_2.

We postulate that this discrepancy arises because these DFT-inspired simulations do not consider the amorphous phase and the crystal-amorphous regions. To confirm this assumption, we studied the PE functionalized with 25 mol% –OH groups further. The system is heated at 1000K for 10 ns under NPT conditions, cooled to 500K at a rate of 50 K/ns, and then allowed to equilibrate at 500K for another 5 ns. Under these conditions, the system is molten. Subsequently, this melt is cooled to 300K at

a rate of 2 K/ns. At 300K, the volume of the system is again equilibrated for 20 ns. The crystallinity of the final structure is then measured by calculating the local order parameter (LOP)[64–69]. Here, each carbon is assigned a bond orientation unit vector, which is calculated by connecting the midpoints of its two adjacent backbone bonds. The bond order parameter between the i^{th} and the j^{th} atom is given by $A = \frac{3\langle\cos^2\phi\rangle - 1}{2} = \frac{3\langle(\vec{b_i}\cdot\vec{b_j})^2\rangle - 1}{2}$ where $\vec{b_i}$ and $\vec{b_j}$ are unit orientation vectors of the respective atoms. The order parameter for a carbon site is determined by averaging the bond order parameters for all carbons within a radius of 0.7 nm. Any carbon with a LOP of more than 0.80 is considered crystalline. The crystallinity of this system was found to be 21 ± 3 %, which is significantly lower than the crystallinity for previously studied PE–OH systems (≈ 60-70 %), which admittedly had lower levels of functionality (maximum of 8.2 mol%) [37]. The system is then run for 50 ns under NVT conditions to calculate the static relative permittivity. The calculated $\varepsilon_{ionic} = 1.96 \pm 0.03$, which is approximately 10 times higher than the result from the fully crystalline structures, validates our hypothesis that the morphology of the materials is crucial for the accurate prediction of the static relative permittivity of these class of polymers.

3.3 Semi-crystalline polymer

We now simulate semi-crystalline systems that are more relevant to the experiment – namely with 4.2 mol% functional groups. To generate PE–X, we create a single polyethylene chain with 1000 backbone carbon atoms. The chain is first equilibrated

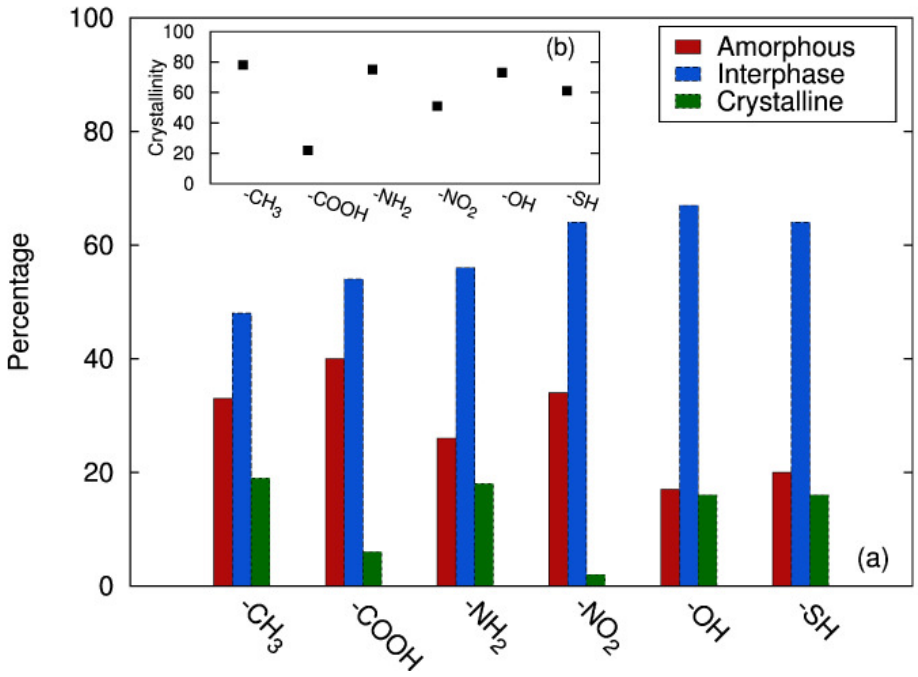

Figure 3.4: The main figure shows the distribution of polar groups in crystalline, interphase and amorphous regions. The inset shows the crystallinity in the system.

at 500 K and 1 bar, where it is in a molten, amorphous state. We then randomly replace 4.2 mol% H-atoms of the CH_2 with the appropriate polar group to generate the amorphous PE–X. The PE–X systems were continuously cooled from 500 K to 300 K at a rate of 2.5 K/ns under isobaric conditions. The system's volume is then allowed to stabilize at 300 K for 20 ns. Thereafter, it is equilibrated in the canonical (NVT) ensemble for 10 ns, and the net dipole moment is averaged for a further 50 ns.

Morphology analysis of the systems at 300 K suggests that the polar groups are predominately localized in non-crystalline regions. More specifically, we quantify the distribution of polar groups, by measuring the degree of crystallinity using the LOP discussed above. A carbon with a LOP less than 0.25 is considered amorphous; more

than 0.80 is considered crystalline; everything in between is considered interphase. We observe for all the PE–X, systems the polar groups prefer to stay in non-crystalline regions (Figure 3.4), which agrees with Flory's notion that these "defect" groups are rejected from crystal[70].

The inset to Figure 3.4 shows that the crystallinity using LOP of all the PE–X is comparable ($\approx$ 60-80%) except for PE–COOH. We compare the crystallinity of these PE–X systems with pure PE by crystallizing PE using the same protocols. The crystallinity of the PE system is calculated to be 79 $\pm$ 2 % using LOP. This appears to not compare favorably with the crystallinity values obtained from differential scanning calorimetry, namely 48% and 46% for pure PE and 1.3mol% PE–OH, respectively [37]. Clearly, a major source of discrepancy is that the theory and the experiments determine crystallinity in different ways. To obtain an experimentally relevant crystallinity, we calculate the ratio of the heat of fusion as obtained from the simulations, ΔH_f, with that of a perfect PE crystal (68.4 cal/g)[71]. To obtain the heat of fusion, we calculated the enthalpy difference between the semicrystalline sample and a corresponding fully amorphous sample at the same temperature (300K). For our simulated PE system, $\Delta H_f = 536.26 \pm 24.63$ kcal/mol, which is equivalent to 38.30 $\pm$ 1.74 cal/g. Thus, the crystallinity for the simulated PE system is found to be 56 $\pm$ 3 %, which is within 20% of the experimental value.

Table 3.2: Percentage of groups in a cluster.

$-CH_3$	–COOH	$-NH_2$	$-NO_2$	–OH	–SH
14 ± 5 %	76 ± 2 %	28 ± 3 %	7 ± 5 %	57 ± 2 %	11 ± 4 %

Since hydrogen bonding plays a critical role, we analyze the systems for cluster

formations. To quantify any pairing of the functional groups, we measure the distance between the polar groups. If the distance between them is less than 3.3 Å, they are considered to be a part of a cluster. Note that here we do not consider the angle constraint and hence it is not hydrogen bonding analysis. The average number of clusters is then reported in the Table 3.2. PE–CH_3 and PE–NO_2, where the functional group does not hydrogen bond, are found to have low clustering. Whereas, PE–NH_2 , PE–COOH and PE–OH form clusters of the polar group.

The ε_{ionic} calculated from these semi-crystalline samples is shown in Figure 3.2. The static relative permittivity from these semi-crystalline samples is found to be significantly larger than those estimated by DFT on the purely crystalline systems at a higher polar concentration in all the systems, except in the case of –COOH. The most significant difference is seen in PE–NH_2 system where the ε_{ionic} is calculated to be 20 times larger than for a semi-crystalline system, as compared to the purely crystalline system. To understand the discrepancy in the results, we synthesized PP–NH_2 [72] and measured its static relative permittivity. Figure 3.3 shows static relative permittivitys of several PP–NH_2 containing 0.4, 1, 1.4, 2.2 and 3.0 mol % –NH_2, respectively, over a temperature range from -20 to 100 °C and a frequency range from 100 to 1 M Hz. We find that our prediction of static relative permittivity using semi-crystalline structure is much closer to experimentally expected values. Note that our simulations do not contain water. As shown in our previous work [37], "bound water" can lead to an additional increase in the static relative permittivity of the material. Hence, morphology is crucial for accurate quantitative prediction of the static relative permittivity for polar polymers relevant to capacitor applications,

which is the primary result of this study.

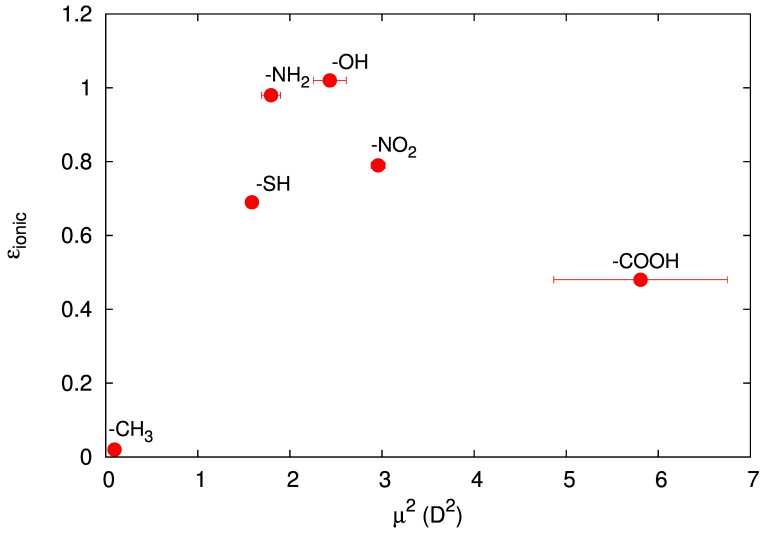

Figure 3.5: Comparison of the ionic static relative permittivity to square dipole moment for various polar groups.

3.4 Dipole Moment Relationship

In order to understand the variation of static relative permittivity with these different functional groups, we are inspired by its definition for amorphous systems, $\langle M \rangle = 0$: $\varepsilon_{ionic} \propto \frac{\langle M^2 \rangle}{V}$. We chose to calculate the microscopic analog of this quantity, and thus we enumerate the dipole moment (μ) of each polar group (CH_2–X) from the trajectory of the simulations. The average dipole moment of each molecule in the sample gives the final dipole of the polar group. Figure 3.5 shows the correlation of the squared dipole moment to ε_{ionic}. We find a linear correlation between some polar groups, but PE–NH_2 , PE–NO_2 and PE–COOH deviate from the trend due to their size, implying that volume of the polar groups plays a significant role in accurately

predicting the relative permittivity.

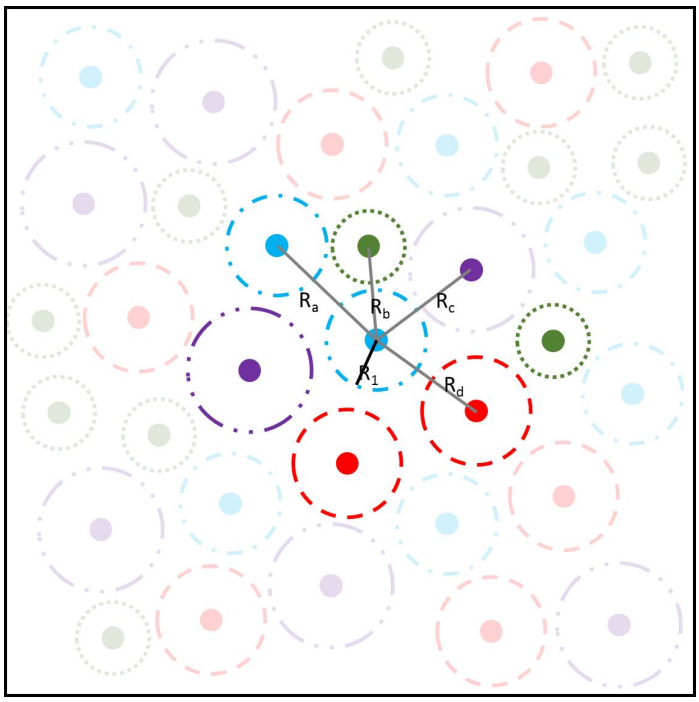

Figure 3.6: Methodology for calculation of volume of each atom in the system.

The volume of each polar group (CH_2–X) is calculated by assuming all atoms are hard spheres. Using the known centers of mass, we find the minimum distance between the atoms of each element and other atoms. The radius of the element is initially defined as half of the distance between the element and the closest atom. The assumed radius allows us to predict the volume occupied by the atoms within the simulation box, and subsequently, the void volume of the system. We then change the radius of each element iteratively to minimize the void volume of the simulation box (Figure 3.6). Thus the radius of the element in the polar group is estimated and subsequently so is the volume of the polar group. Figure 3.7 shows a high correlation between static relative permittivity with the ratio of the square of the dipole moment of each polar group relative to the calculated molar volume. One exception is the

case of $-NO_2$, which shows some discrepancy from the linear trend. Note also that we use the quantities relevant to a –COOH dimer due to its known propensity to dimerize. Therefore, we can predict the static relative permittivity by calculating the "molecular" dipole moment and the "density" of these functional groups an idea that also explains the results of Dong et. al. [73].

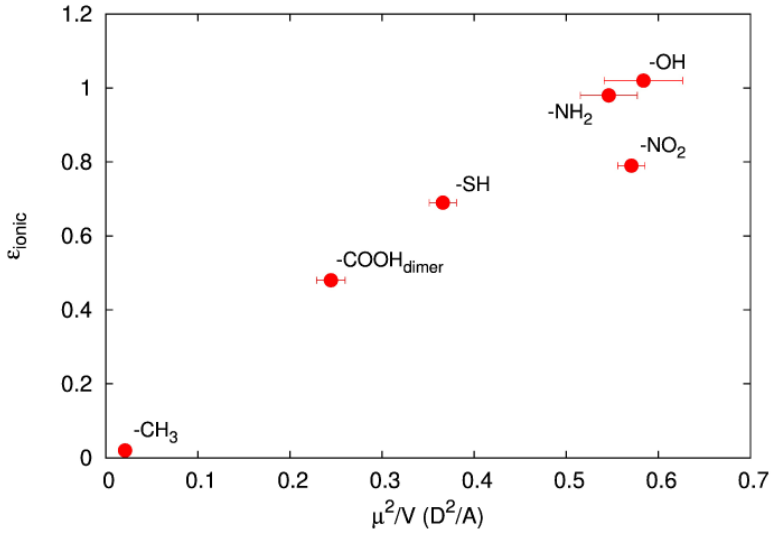

Figure 3.7: Comparison of the ionic static relative permittivity to square dipole moment by volume for various polar groups.

We now provide a mathematical understanding of the role of morphology in the prediction of the static relative permittivity. We go back to the definition: $\varepsilon_{ionic} = \frac{4\pi\left(\langle M^2\rangle - \langle M\rangle^2\right)}{3Vk_BT}$, and note that the significant quantities are $\langle M^2\rangle$ and $\langle M\rangle$, where $M = \sum_i \mu_i$, i.e., the sum of the individual dipoles in the system. For simplicity let us consider one chain, and make the simplified assumption that local dipoles are aligned along the bond direction. In this situation, the net dipole of the chain is equivalent, within a multiplicative constant, to the end-to-end vector of the chain. For a purely Gaussian chain $\langle M\rangle = 0$ and $\langle M^2\rangle$ is equivalent to mean square end-to-end

distance of the chain. The statistics of a single chain under the action of a stretching force (as derived by Rubinstein and Colby [74]), clearly show that the variance, $\langle M^2 \rangle - \langle M \rangle^2$ assumes its maximum value for a Gaussian chain (or alternatively in an amorphous phase), and decreases monotonically to zero at full extension (i.e., in a completely ordered crystalline domain). By analogy, for small enough variations about the amorphous state, the ε_{ionic} will be unaffected. Now consider a large enough perturbation where all the chains are stretched fully along the z, direction but retain complete freedom along the x and y directions. In this case, it is easy to show that the ε_{ionic} will be 2/3 its value in the fully amorphous phase. The fact that the crystalline DFT results are up to an order of magnitude smaller must stem from the limited x and y mobility ("libration") of the functional groups in the crystal.

3.5 Conclusion

Our results clearly show that simulating the right morphology, especially one where the dipoles in a sample can relax in a manner that mimics experimental reality, is necessary to quantitatively predict the dipole moment of the material. Thus, simulating a purely crystalline phase, where all the dipoles are strongly constrained, will not provide a good representation of the real, semi-crystalline polymeric material of relevance to experiment. In recent works, it has been postulated that large increases in the ionic static relative permittivity can be achieved by using defective crystals with increased free volume [73, 75]. While this last idea is indeed appealing, we note that such fringed micelle type models for polymer crystals were the focus of debate

over 50 years ago. Unequivocal experimental evidence suggests that nature avoids such structures and predominantly favors the formation of a densely packed crystal surrounded by amorphous phases with lower densities. At this time, we believe that the existence of a polymer in an amorphous phase, either by itself or as part of a semi-crystalline entity, maximizes the static relative permittivity for this class of materials.

Chapter 4

Dielectric Loss

4.1 Introduction

State of the art in polymeric capacitor films is biaxially oriented polypropylene (BOPP) [76], which has an exceptionally high electrical breakdown strength (> 700 MV/m) and low dielectric loss ($> 0.1\%$), but a small static dielectric permittivity (2.2). An attractive scheme for improvement of the energy density of polypropylene (PP) is by increasing the static dielectric permittivity of the material while preserving the low loss. The obvious way to increase the permittivity is by the addition of polarizable groups to PP. While this method increases the dielectric permittivity, the slowed-down dynamics of most polar groups also produces increased dielectric loss in the range of frequencies relevant to power electronics. Recent experiments have shown that the addition of a small number of polar hydroxyl (OH) groups is known to increase the static dielectric permittivity of a nonpolar polymer[28, 37, 63], while not significantly increasing the dielectric loss in the relevant operational frequencies.

In the previous chapter, we have explored alternative functional groups for increasing the relative permittivity of substituted polyethylene (PE). While adding a small amount of these functionalities to the polymer increases the dielectric

permittivity, it could affect the material by increasing the losses and therefore limiting the potential use of the material for power electronics. Consequently, the dielectric loss needs to be estimated for a potential polar group functionalities. By utilizing Molecular Dynamics (MD) simulations, the dielectric loss of the functionalized PE can be investigated. While MD is an attractive approach for exploration of the dipole relaxation of the chain, the limit on accessible time-scales can be a limiting factor. One possible approach to overcome this time barrier is by assuming a permanent dipole moment in the system, and thus exploring incomplete dynamics[48, 77]. While this method is appropriate for trapped systems, it will have a huge error associated with estimation of dielectric loss of a class of polymers relevant to our study with a relatively small amount of polar groups. Another technique investigated recently is by using a coarse-grained model for predicting these properties significantly faster [78]. This technique is an exciting approach, but it fails to capture the local structure and dynamics (like hydrogen bond relaxation) of the system which has a significant effect on the relaxation process as shown in this work. In this study, we propose time-temperature superposition (tTS) as a possible pathway for determining the chain dynamics of semi-crystalline functionalized PE. The benefit of doing tTS is that we can capture complete relaxation of the chains in the simulation, without making computation abnormally expensive. Moreover, tTS also enables us to explore experimentally significant frequencies, $10^3 - 10^6$ Hz, thus making it more relevant for application in power electronics.

4.2 Hydroxyl substituted polyethylene

Dipole Correlation Function

The orientation of molecular dipoles is a relatively slow process in comparison to the electronic transitions or molecular vibrations, which have frequencies generally above 10^{12} Hz. Furthermore, it does not consist of a uniform switch in the arrangement of molecules; it is due to a slight adjustment of the average orientation in the face of continued thermal agitation. Only when sufficient time is allowed after the application of an electric field for the orientation to attain equilibrium will the maximum polarization, corresponding to the highest observable relative permittivity, be realized in a material. If sufficient time is allowed, then observed dielectric constant is maximum and we attain the static dielectric constant. However, if the polarization is measured instantaneously ($< 10^{12}$ ps) the observed dielectric constant is relatively low and only captures the electronic component of dielectric constant. Similarly, there is a decrease in dielectric constant for every relaxation process which is slower than the operational frequency of the material. Henceforth, a suitable material for dielectric application should have a fast orientational relaxation.

The theory of relaxation behavior was pioneered by Debye. It begins with relaxation processes described by the normalized dipole correlation function, $\Phi(t)$ (DCF):

$$\Phi(t) = \frac{< M(0) \cdot M(t) >}{< M(0) \cdot M(0) >}$$

In the regime of linear response, the application of Kubo's general theory for statistical mechanics of linear dissipative systems implies that dynamic properties can be expressed in terms of quantities relevant to the dielectric in the absence of the field [79]. The complex dielectric permittivity $\varepsilon^*(i\omega) = \varepsilon'(\omega) - i\varepsilon''(\omega)$ is obtained following the superposition relation:

$$\begin{aligned}\frac{\varepsilon^*(i\omega) - \varepsilon_\infty}{\varepsilon_0 - \varepsilon_\infty} &= \int_0^\infty \mathrm{d}t[exp(-i\omega t)] \left[-\frac{\mathrm{d}\Phi(t)}{\mathrm{d}t}\right] \\ &= 1 - i\omega \int_0^\infty \mathrm{d}t[exp(-i\omega t)]\Phi(t)\end{aligned}$$

where ϵ_0 and ϵ_∞ are the limiting low and high-frequency permittivities respectively. The $\Phi(t)$ is the normalized dipole correlation function of the polarization when a steady macroscopic electric field is removed from the medium. Hence, $\Phi(t)$ contains contributions from relaxation processes only and the above equation shows that it is a function of dielectric loss given by,

$$\Phi(t) = \frac{2}{\pi} \int_0^\infty \frac{\mathrm{d}\omega}{\omega} \left[\frac{\epsilon''(\omega)}{\epsilon_0 - \epsilon_\infty}\right] \mathrm{cos}\omega t$$

where ε_0 and ε_∞ are the limiting low and high-frequency permittivities respectively. Consequently, to assess the dielectric loss of polyethylene substituted with polar groups we calculate the dipole correlation function using Molecular Dynamics. We simulate the functionalized polyolefin chain by using the optimized potential for liquid simulations, which is an experimentally validated all atom force field (OPLS-AA) [14, 15]. Bond stretches and angle bendings are represented using harmonic potentials, and dihedral motions are governed by the OPLS-AA triple cosine series potential. van

der Waals interactions between the different chain moieties are described by standard Lennard-Jones 12-6 (LJ) potentials. The parameters for interactions between unlike pair of atoms i and j are calculated using mixing rules i.e. $\sigma_{ij} = \sqrt{\sigma_{ii}\sigma_{ii}}$ and $\varepsilon_{ij} = \sqrt{\varepsilon_{ii}\varepsilon_{ii}}$ where σ is the LJ size parameter and ε is the LJ well-depth parameter. Electrostatic interactions between two atoms, each with partial charge of q_i, are modeled by $U_E(r) = \sum_i \sum_j \frac{q_i q_j}{4\pi\varepsilon_o r}$, where r is their separation distance and ε_0 is the permittivity of free space. To speed up the simulations, we exploit general-purpose graphical processing units (GPGPU) to accelerate the van der Waals and long-range Coulombic calculations,[38, 39] implemented in LAMMPS[40].

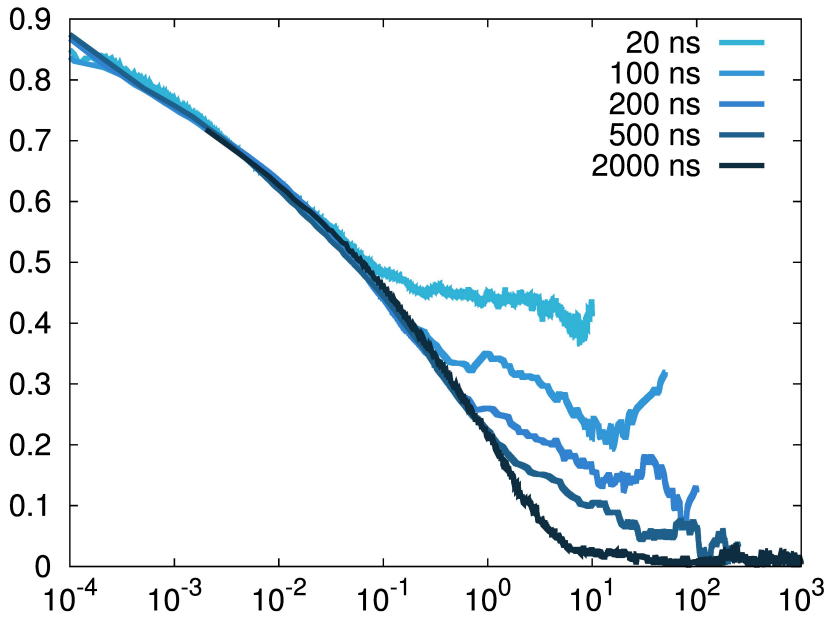

Figure 4.1: Dipole correlation function of 4.2 mol% PE–OH after 20ns, 100ns, 200ns, 500ns, and 2000ns.

We generate PE–OH by first creating a single polyethylene chain with 1000 backbone carbon atoms. The chain is equilibrated at 500 K and 1 bar, where the chain is in an amorphous state. We then randomly replace 4.2 mol% H-atoms of

the CH_2 with the appropriate –OH group to generate the amorphous PE–OH. The system is then continuously cooled from 500 K to 300 K at a rate of 2.5 K/ns under isobaric conditions. The system's volume is then allowed to stabilize at 300 K for 20 ns. Thereafter, it is equilibrated in the canonical ensemble for 10 ns, and the net dipole moment is then sampled for 20 ns for calculation of dipole correlation function, $\Phi(t)$.

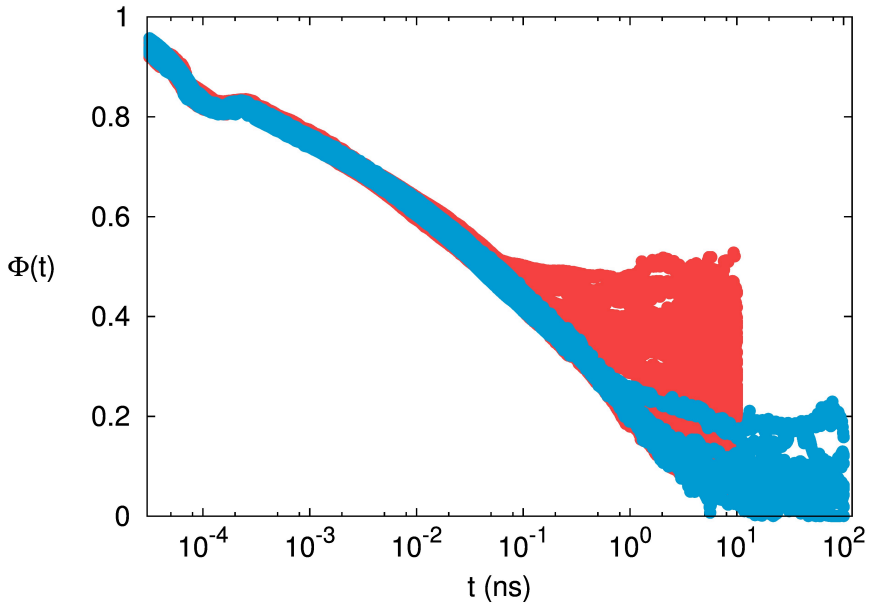

Figure 4.2: Dipole correlation function for time intervals of 20 ns and 200 ns over 2000 ns simulation.

The calculated the $\Phi(t)$ for the system at 300K at various time intervals are shown in figure 4.1. The non-zero "plateau" (M_t) observed at long correlation time for shorter time interval may be indicative of kinetically trapped system or the system having a permanent dipole moment, as considered by Goddard et. al. [48]. However, on increasing the time interval the value of M_t decreses monotonically suggesting otherwise. It requires more than 1000 ns of simulation time for the M_t to reach

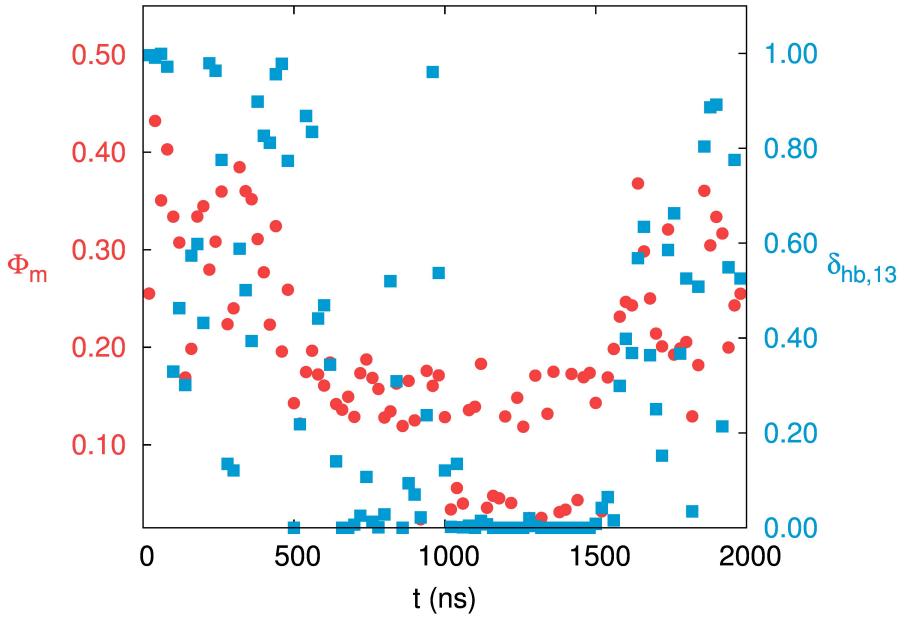

Figure 4.3: The red circles represent the average value of correlation,Φ_m , between 0.1 ns and 10 ns for 20 ns split. The blue squares represents the fraction of time hydroxyl labeled 13 is hydrogen bonded in a 20 ns split.

zero. Further, to explore the reason behind the plateau we plot dipole correlation function of the time intervals of 20 ns and 200 ns in figure 4.2 by splitting the 2000 ns simulation data into 100 and 10 parts respectively. We observe that the dipole correlation function is significantly relevant only below the $t_i/100$, where is the t_i is the time interval of the data, beyond which the data fluctuates. We also plot the average value of correlation, Φ_m, between $t_i/100$ and $t_i/2$ and find it to be non-monotonic in nature (Fig. 4.3). We argue that this non-monotonic behavior is related to hydrogen bonding. A hydroxyl is defined as a hydrogen bonded to the standard procedure described in our previous work [37], where a cutoff distance is 0.3 nm, and a cutoff angle is 30°. For each hydroxyl in a given 20 ns time interval, we calculate the fraction of time it is hydrogen bonded. Following that, we calculate the average

fraction of time hydroxyls are hydrogen bonded by averaging over all the hydroxyls in the system. This calculated time for each time interval split is compared to the Φ_m of the same split (Fig. 4.4) and the Pearson correlation is found to be high ($\rho_{\Phi_m,\delta_{hb}} = 0.95$). This shows that hydrogen bonding is playing a critical role in increasing error in the dipole correlation function. On further exploration, we find that this error is primarily due to the size of the box, and only one hydrogen-bonded cluster is responsible for it (Fig. 4.3). Hence to counterbalance for the small amount of hydroxyls in the system we have to gather more data i.e. run simulation longer.

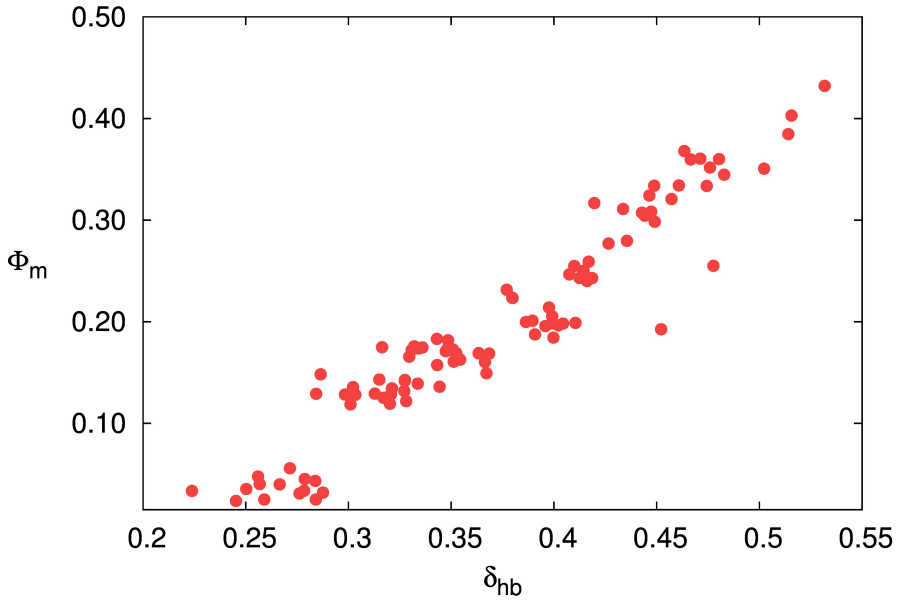

Figure 4.4: Correlation between the average value of dipole correlation,Φ_m and average fraction of time hydroxyls are hydrogen bonded in a 20 ns split.

Time Temperature Superposition

We note that the calculation of the full, equilibrated dipole correlation function of 4.2 mol % PE–OH requires simulation times on the order of microseconds. To reduce this

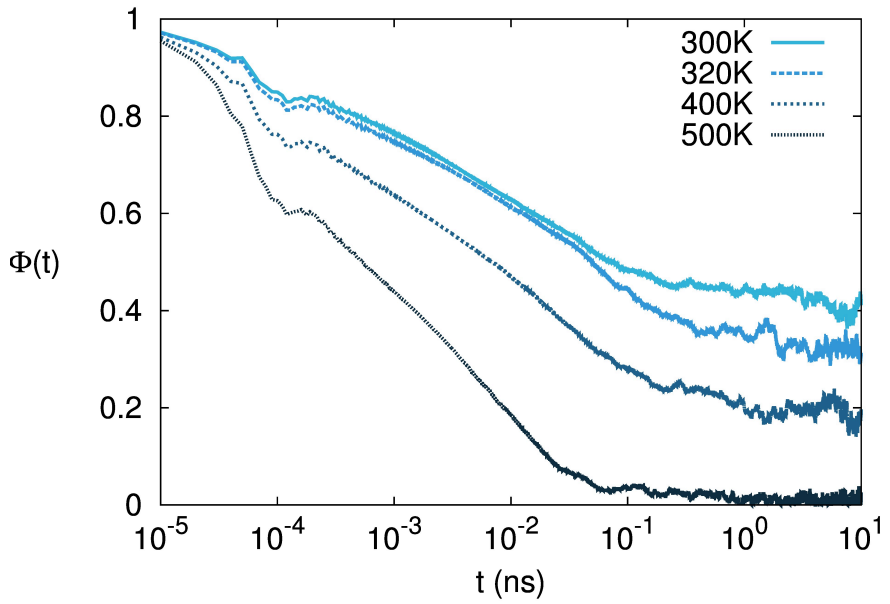

a)

Figure 4.5: Dipole correlation function of 4.2 mol% PE–OH at 300K, 320K, 400K, and 500K.

computational time, we explore the notion of time-temperature supposition (tTS). The semicrystalline system at 300K is heated to 320K and equilibrated for 5ns under NVT conditions. Thereafter, a production run of 20ns is performed to calculate DCF. Predictably, the dipoles relaxed further at 320K. The same procedure is then implemented for various temperatures until the dipoles completely relax at 500K. The DCF for 320K, 400K and 500K were shifted to create the master curve for 300K (FIG. 4.6b).

It is of our particular interest to note that these short time simulations yield "plateaus" at long timescales. We use the "decaying" part of the correlation function but ignore these plateaus (which correspond to the slowest relaxing H-bonds in each specimen) to create the master curve. Similarly, the fastest part of the relaxation function, which corresponds to librational motions, represents a different time scale

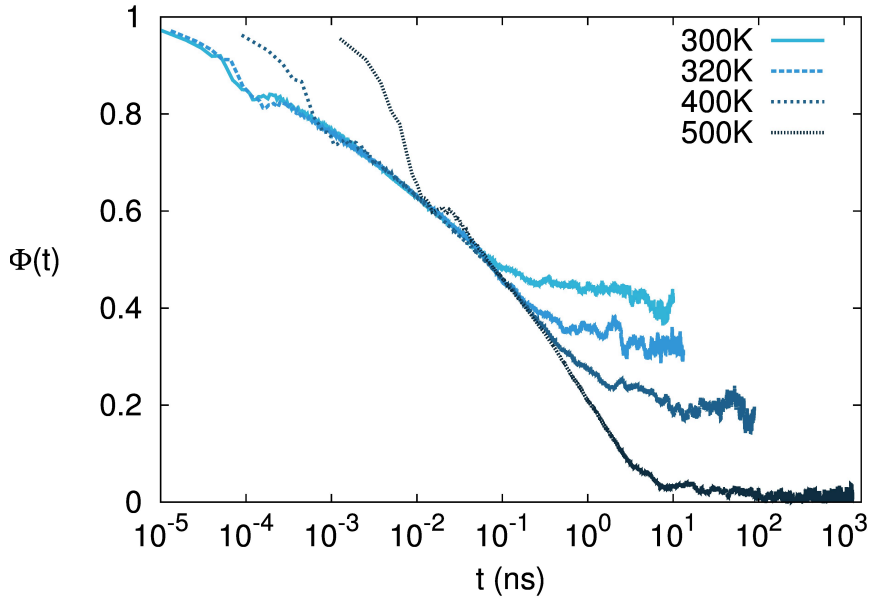

a)

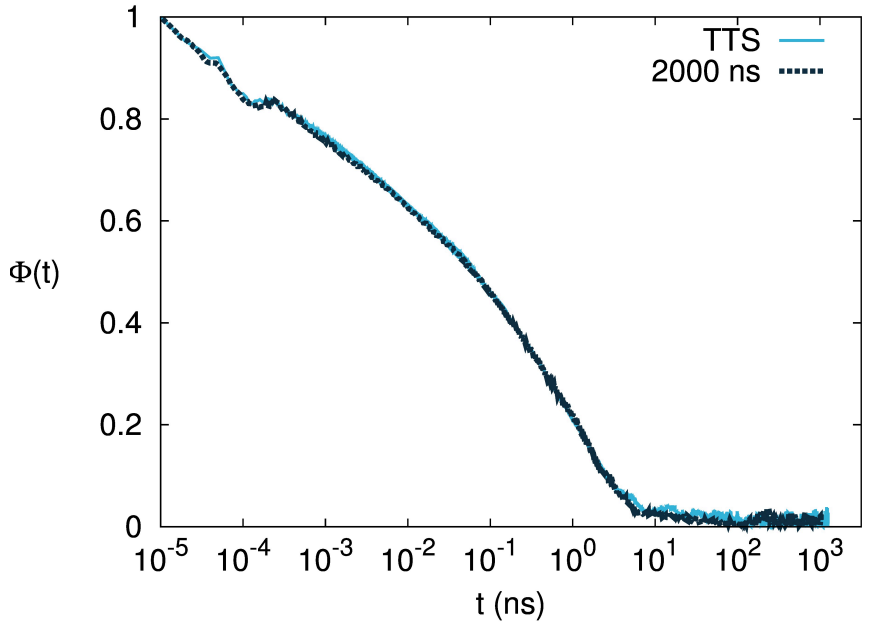

b)

Figure 4.6: (a) Master curve of dipole decay function of 4.2 mol% PE–OH at 300K using TTS (b) compared with 2000ns simulation.

process which is thus not included in the tTS procedure. The master curve obtained in this fashion, which accounts for the segmental relaxations, is compared to the single long simulation (Figure 4.6b) and they agree with each other. To examine the methods quantitatively, we fit the two obtained dipole correlation function to a stretched exponential function, $\Phi(t) = \exp[-(t/\tau)^{\beta}]$. The average relaxation time for a single long run and from tTS are calculated to be 2.19 ± 0.2 ns and 2.72 ± 0.5 ns, respectively. Importantly, while the two flavors of simulation provide the same relaxation behavior, however, the computational time required for tTS is two orders of magnitude less.

4.3 Effect of other polar groups on polyethylene

We use this tTS method to find the effect of four different types of polar groups on the characteristic relaxation time of substituted polyethylene. To generate PE–X, where X is –NH_2,–SH, and PE–NO_2, we follow the same protocol as for PE–OH. We randomly replace 4.2 mol% H-atoms of the CH_2 with the –X polar group to generate the amorphous PE–X, followed by isobaric cooling at a rate of 2.5 K/ns. The systems are then equilibrated followed by the production run for calculating the correlation function. The dipoles in PE–NH_2 and PE–SH system relax completely at 500K, while PE–NO_2 system was heated to 600K for the dipoles to completely relax. Figure 4.7a compares the dipole correlation functions of various PE–X systems. To calculate the dielectric loss and average relaxation time, we fit the obtained correlation function to a stretched exponential function. The parameter used for

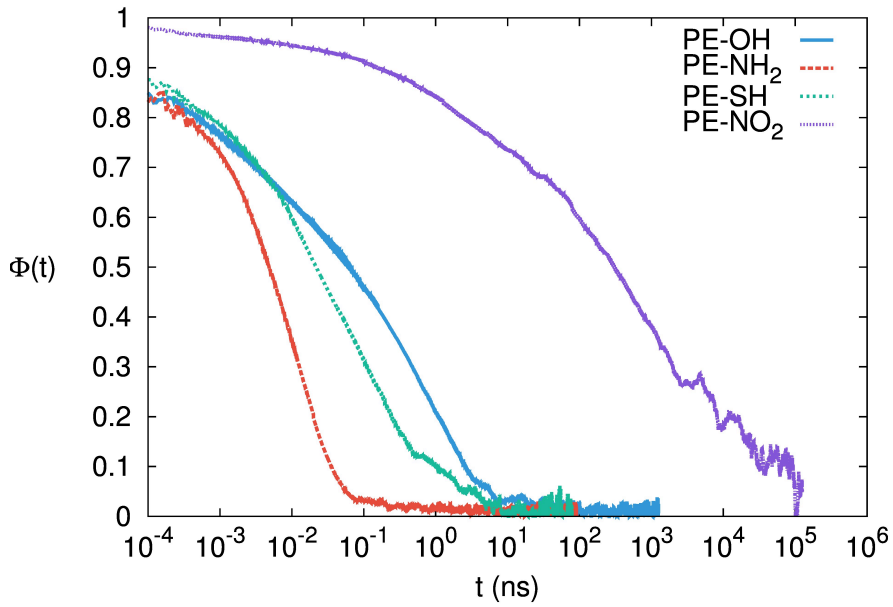

a)

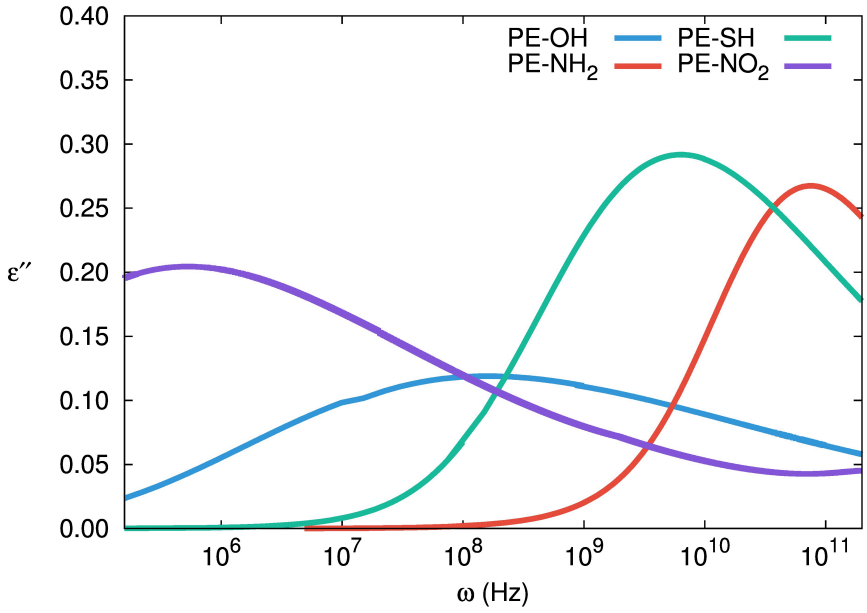

b)

Figure 4.7: Dielectric correlation function for (a) various PE–X systems obtained from time temperature superposition and (b) the calculated dielectric loss from the master curves.

fitting are shown in Table 4.1. The average relaxation time is calculated using: $\tau_{avg} = \frac{\tau}{\beta}\Gamma\left(\frac{1}{\beta}\right)$. The average relaxation is the fastest for PE–NH_2 closely followed by PE–SH and PE–OH, while PE–NO_2 is orders of magnitude higher. It is important to recognize this big difference between PE–OH, which relaxes in nanoseconds, while PE–NO_2 requires several microseconds; the latter is inaccessible using regular all-atom molecular dynamics simulation and is only achieved using tTS.

Table 4.1: Streched exponential fitting parameters for the dipole moment DCF for various systems.

	τ (ns)	β	τ_{avg} (ns)
PE–OH	2.0×10^{-1}	0.17	$2.19\text{x}10^{0}$
PE–NH_2	9.7×10^{-3}	0.49	$2.04\text{x}10^{-2}$
PE–SH	1.1×10^{-1}	0.35	$5.48\text{x}10^{-1}$
PE–NO_2	2.6×10^{3}	0.23	$1.05\text{x}10^{5}$

As described earlier, the fitted stretched exponential function is used to calculate the dielectric loss; the resulting characteristic time for local relaxations determines the location of the dielectric loss peak. Figure 4.7b shows the calculated dielectric loss for PE–OH, PE–NH_2, PE–SH, and PE–NO_2 obtained from the master curves in figure 4.7a. We observed that the loss peaks for PE–NH_2 and PE–SH are at 10^{11} Hz and 10^{10} Hz respectively, and the loss rapidly drops off to insignificant values on reaching relevant operational frequencies of MHz. Although PE–OH has peak dielectric loss at 10^{8} Hz, which is orders of magnitude higher than PE–NH_2 and PE–SH, the loss drops to less than 1% at the frequency of interest, namely 10^{5}-10^{6} Hz. The PE–NO_2 has a loss peak very close to relevant operational frequencies, thus making it inappropriate for applications.

It is hard to validate the high dielectric loss prediction of PE–NO_2 due to the

limited experimental exploration of this class of polymers. Borisova [80] compared the mobility of side-chain nitro groups in a class of polyolefin based polymers. $PVNO_3$ is most similar to the PE–NO_2 among the polymers studied experimetally. At 300K and 1 kHz, the dielectric loss for PE–NO_2 is predicted to be 0.03, while experiments on $PVNO_3$ find it to be 0.08, which is in reasonable agreement. Due to lack of experimental data, we cannot compare the dielectric loss at other frequencies. However, the frequency dependence of dielectric loss is available for a different polymer, PNO_3EMA. Figure 4.8 shows the experimental dielectric loss of PNO_3EMA [80] along with the predicted dielectric loss for the PE–NO_2. We see that the relaxation time (inverse of the loss peak) of the nitro group for the samples are similar providing a second validation of our tTS based calculation. More experimental results are necessary to give us confidence that this methodology is a reliable means for simulating these practically interesting systems.

The dielectric loss has been associated with the size of the molecule and the dipole orientation for small molecules[81]. We believe for a low concentrated spatial distributed polar group containing system this should still be valid. To examine this idea, we calculate the dipole moment of each polar group (CH_2–X) from the trajectories of the simulations. The average dipole moment of each molecule in the system gives the final dipole of the polar group. Figure 4.9 shows the relationship between the calculated dipole moment and relaxation time. The relaxation time is found to grow with the dipole moment of the system exponentially. Thus, suggesting that a possible path for designing material with low dielectric loss is by keeping the dipole moment small. However, their concentration can be increased to the point

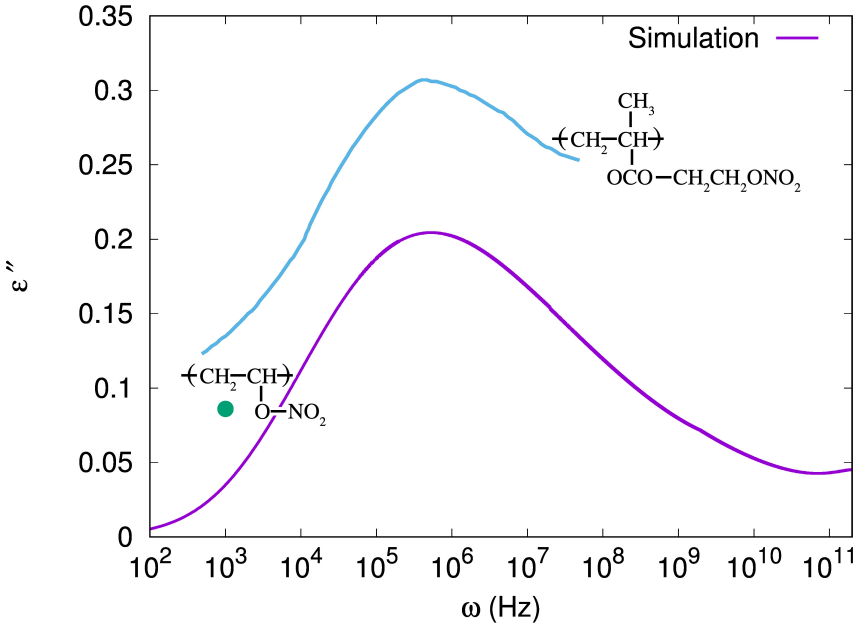

Figure 4.8: Comparision of dielectric loss of 4.2 mol% PE–NO_2 with experimentally calculated dielectric loss of $PVNO_3$ (green circle) and PNO_3EMA (blue line) [80].

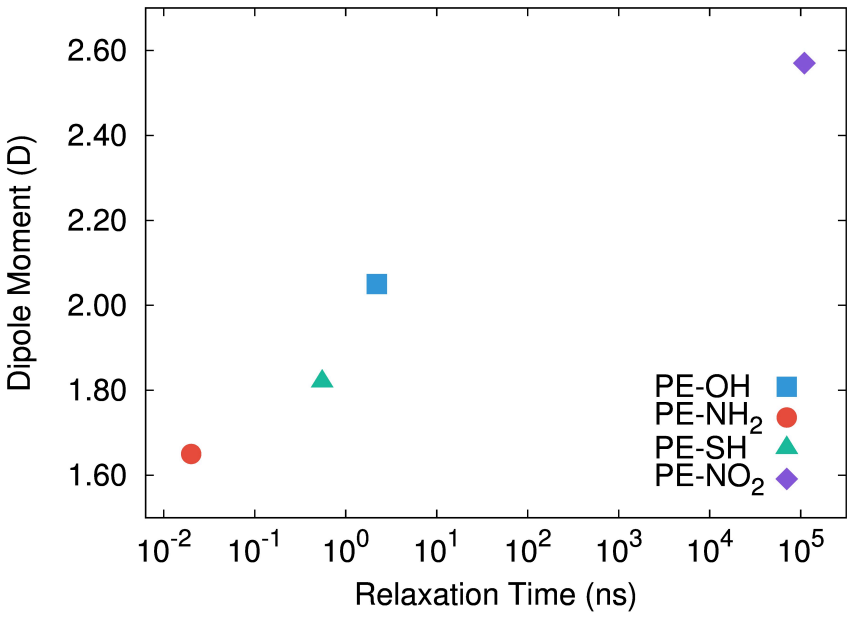

Figure 4.9: Correlation of the calculated relaxation time for PE–X systems with the dipole moment.

where they are still spatially distributed. Further analysis of the critical concentration for this change in behavior needs to be done.

4.4 Conclusions

We investigated the effect of other polar groups on the relaxation of polyethylene. To fully explore the relaxation behavior of PE–OH we ran a simulation to microseconds. We also developed a scheme for capturing the same relaxation process using time-temperature superposition. To find the two flavors of MD simulations to give the same relaxation behavior thus providing us with a significantly faster and accurate method for calculation of dielectric properties. We extend this technique to predict the dielectric loss of PE–NH_2, PE–SH and PE–NO_2 system.

Chapter 5

Dielectric Breakdown

Despite abundant experimental study on dielectric properties of polymers, the origins of high dielectric breakdown remains an open question. Although, the dielectric breakdown in polymer is a non-trivial problem, there has been a significant increase in understanding the phenomena in polymeric materials. The classical models developed for understanding breakdown have been deterministic in nature where the breakdown occurs as a direct effect of an earlier event or condition produced by crossing over a threshold electric field. We explore these deterministic models of dielectric breakdown using molecular dynamics to understand the mechanism of dielectric breakdown within polymeric materials. Since the deterministic breakdown is directed by cause, we can divide the types of deterministic breakdowns into three processes: (i) thermal breakdown, (ii) electronic breakdown and (iii) electromechanical breakdown.

Wagner et. al [82] proposed the first theoretical model to explain the breakdown observed at high temperatures in dielectric materials. The model emphasized the inverse relationship of the breakdown against temperature. This suggests that the heat released due to losses in the system results in joule heating that when not balanced, results in thermal breakdown. The increased heat can also lead to increased segmental motion, which may cause increased ionic conduction in the material. The

thermal breakdown leads to a highly localized filamentary breakdown path, leading to a catastrophic failure in the material[83].

Thermal breakdown explains the dielectric breakdown at high temperatures, but it fails to explain the cause of the breakdown in a dielectric material at low temperatures. This led to an increased focus on the effect of electronic conduction as seen in semiconductors. Due to the extensive research for semiconductors, the two most famous electronic breakdown mechanisms are Zener breakdown and electron avalanche. Both the models can describe the low temperature behavior of the breakdown accurately where the breakdown has a weak temperature dependence.

Zener breakdown occurs when an electron is able to jump from the valance to the conduction band in the presence of the external electric field. For polymers with a low band gap ($< 4eV$) fields of 10^9 V/m would cause a Zener breakdown. However, as the polymer breakdown magnitude is limited to 10^9 V/m, polymers with higher band gaps would invariably breakdown by other mechanisms. Electron avalanche occurs at high electric fields when electrons acquire enough energy due to collisions with the medium to get ionized. A small current can be greatly multiplied by an increase in the number of electrons to cause irreversible damage [84]. A high mobility($10^{-4}m^2V^{-1}s^{-1}$) is required for avalanche formation in polyethylene has been shown to exist both theoretically and experimentally [11, 85].

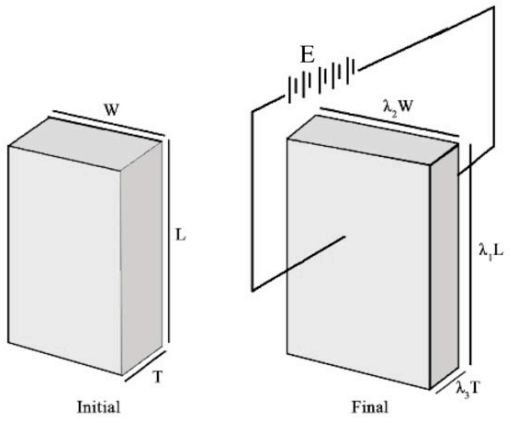

Figure 5.1: Thinning effect seen due to the electromechanical breakdown.

5.1 Electromechanical Breakdown

Electrostatic attraction forces can also result in electrometrical breakdown due to the thinning of the dielectric material by an amount that depends on the Young's modulus (Figure 5.1). If the applied voltage is maintained, the field increases due to the decrease in thickness thereby increasing the attraction further. Stark and Garton speculated that electromechanical breakdown occurs when the mechanical compressive stress on the dielectric caused by the electrostatic attraction of the electrodes exceeds a critical value which cannot be balanced by the dielectric's elasticity[86].

$$\frac{\varepsilon_0 \varepsilon_r}{2} \left(\frac{E}{T\lambda_3} \right)^3 = Y log \left(\frac{T}{T\lambda_3} \right) \tag{5.1}$$

As shown in equation 5.1, E is the electric field, T is the initial thickness in the field direction, $T\lambda_3$ is final thickness and Y is the youngs modulus. The maximum electric field is obtained at $\lambda_3 = exp(-0.5) \approx 0.6$ and the breakdown voltage is given by

$$E_{breakdown} = T\left(\frac{Y}{\varepsilon_0 \varepsilon_r}\right)^{1/2} \tag{5.2}$$

Stark and Garton carried out experiments to check the model (Equation 5.2) for both crosslinked and uncrosslinked and found it to agree with the predicted values from equation 5.2. Following their paper, other researchers also attributed the breakdown of various polymers to this mechanism[87, 88]. We further compared the observed breakdown to calculated breakdown[8, 9, 86–92] using equation 5.2 (Figure 5.2).

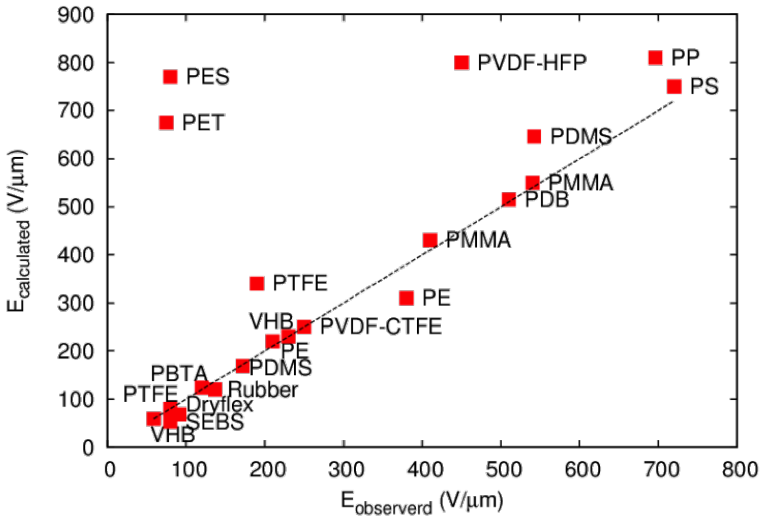

Figure 5.2: Comparison with Stark and Gartons model for various polymers[8, 9, 86–92].

To further emphasize the importance of electromechanical breakdown, the dependency of dielectric breakdown on temperature for various polymers was compared in figure 5.3. We observed that at low temperature regions, electronic

breakdown dominates where temperature has no effect on dielectric breakdown. While at high temperature region, electromechanical and thermal breakdown are dominant. The polymers soften with increasing temperature, which is related to the glass transition temperature, Tg. The polymers undergo a transition from a glassy state to a plastic flow state with increasing temperature which also results in transition from electronic breakdown to electromechanical or thermal breakdown as shown in the figure 5.3. An attempt was also made to prevent electromechanical breakdown in polyethylene by reducing its temperature to 77 K, well below its glass transition temperature. However, electromechanical breakdown mechanism was still observable[93]. Electromechanical breakdown was prevented by restraining plastic flow in the polyethylene, by encapsulating it in a crosslinked silicone rubber, which was brittle at 77 K. Hence, we observed that the breakdown process in common polymers is dominated by electromechanical breakdown at room temperature.

5.2 Simulating Breakdown

For simulations, we used the Optimized Potentials for Liquid Simulations-All Atom force field (OPLS-AA). Although many force fields exist for PE, the generic nature of the OPLS-AA formalism lends itself to a wide variety of polymeric systems[15]. Polarizable force fields could be used for greater accuracy but we use a non-polarizable force field due to its computational expediency. Since even the non-polarizable force field simulations are expensive, we exploit general-purpose graphical processing units (GPGPU) to accelerate the van der Waals and long-range Coulombic calculations[38,

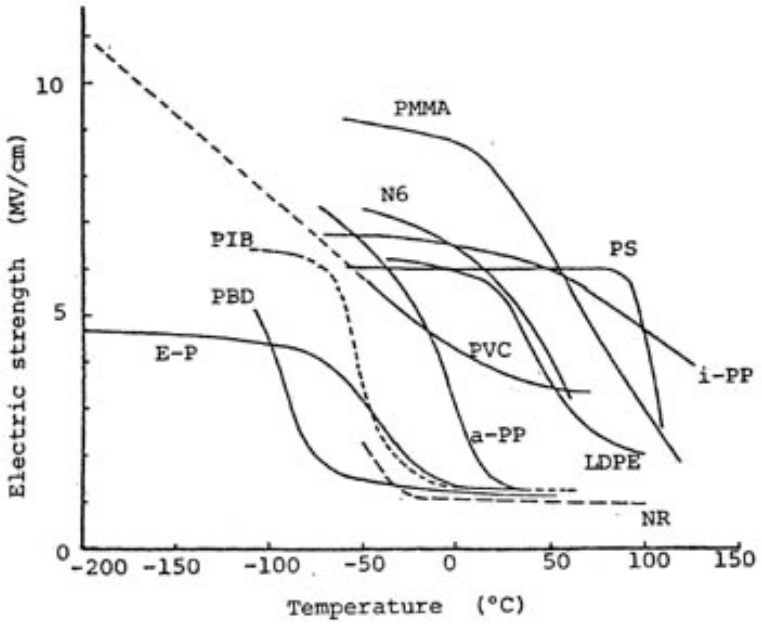

Figure 5.3: Dependency of dielectric breakdown on temperature for various polymers[11].

39], as implemented in LAMMPS[40].

Single Chain Polyethylene

A single polyethylene (PE_{1C}) chain with 1000 backbone carbon atoms was equilibrated at 500 K and 1 bar, where it was in an amorphous state. The system was then cooled from 500 K to 300 K at 5 K/ns under isobaric conditions. The volume was allowed to stabilize at 300 K for 40∼50 ns, followed by 5∼6 ns equilibration in the canonical (NVT) ensemble.

To mimic the external field a force of qe was added to all atoms[94] in isothermal–isobaric ensemble (NPT). The unidirectional field was applied and ramped up to the desired electric field voltage at a rate of 50 50 V/μm ns. The systems were then allowed to equilibrate at the desired electric field for 2ns. The average box size in

the field direction was then calculated for the last 500 ps. The average box size in the field direction relative to the initial box size gives us strain (λ) for the specific electric field voltage. For our systems, a unidirectional field was applied in each the x, y, and z direction. Thereafter, the obtained λ from three directions was averaged for each voltage to account for the isotropy missing in semi-crystalline systems in the simulations.

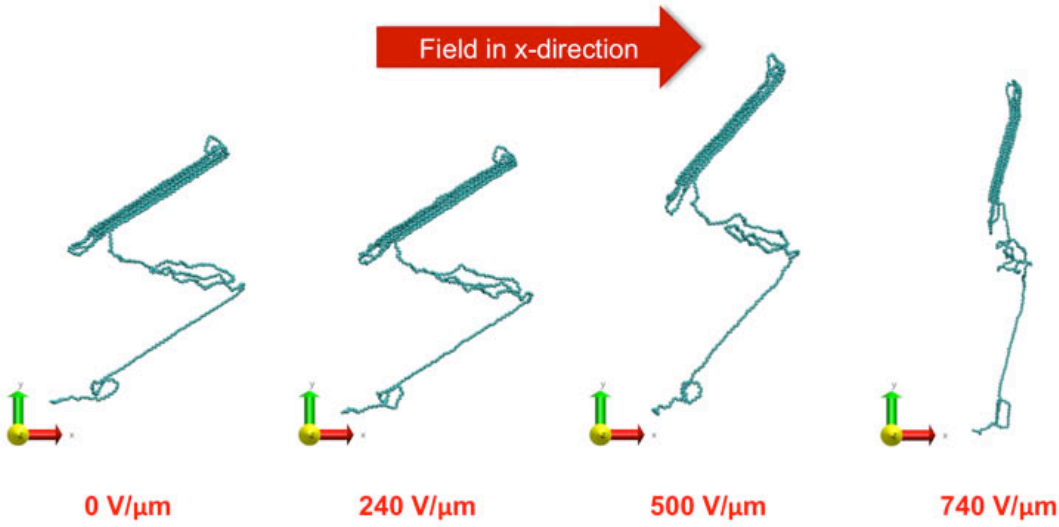

Figure 5.4: Thinning effect in single chain of PE containing 1000 carbons in presence of external electric field.

Similar to the experiments, the thinning of PE_{1C} in the field direction was observed in the simulation (Figure 5.4). There is no significant change in thickness of the polymer in the field direction at low electric fields (Figure 5.5). However, at a critical field there was a drastic decrease in thickness of the polymer in field direction, resulting in the dielectric breakdown.

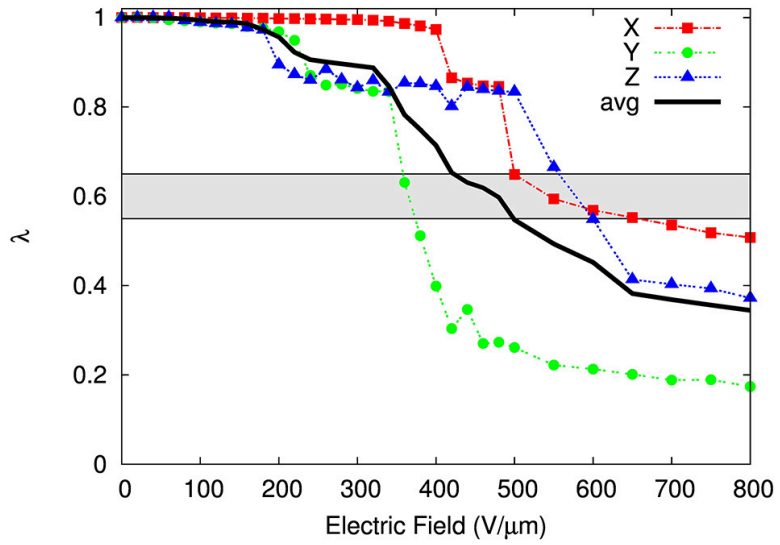

Figure 5.5: Change in thickness in the field direction at varying external electric field for PE_{1C}. The grey band represents the breakdown region calculated using Stark and Garton's model.

5.3 Effect of system size

To study the effect of the size of the system, four chains of polyethylene (PE_{4C}) with 1000 backbone carbon atoms in each chain at 1000K and 1 bar generated. We then cooled the system to 500 K at a rate of 100K/ns, where it was in an amorphous state. The system was then cooled from 500 K to 300 K at 5 K/ns under isobaric conditions. The volume was allowed to stabilize at 300 K for 10 ns, followed by 5 ns equilibration in the canonical (NVT) ensemble to get a crystalline structure (Figure 5.6). Thereafter, electric field was applied following the same protocol as used for PE_{4C}. We again observed thinning of PE in the field direction (Figure 5.7), similar to 1 chain behavior. Thus, suggesting that there is no effect of the system size on the response of system to external electric field.

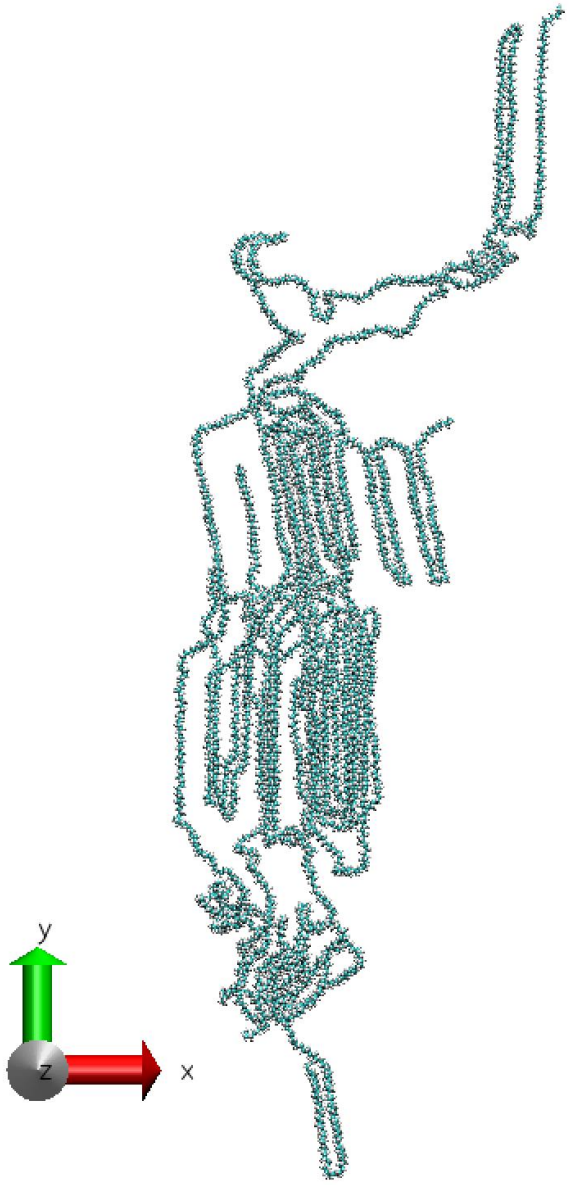

Figure 5.6: Semi-crystalline four chains of PE containing 1000 carbons in each chain

5.4 Effect of crystallinity

Amorphous system was created using eight chains of polyethylene (PE_{8A}) with 1000 backbone carbon atoms in each chain at 1000K and 1 bar. We then cooled the system to 500 K at a rate of 100K/ns and then to 300K at a rate of 20K/ns. Due to the relatively faster cooling, the system was still in an amorphous state (Figure 5.8) at

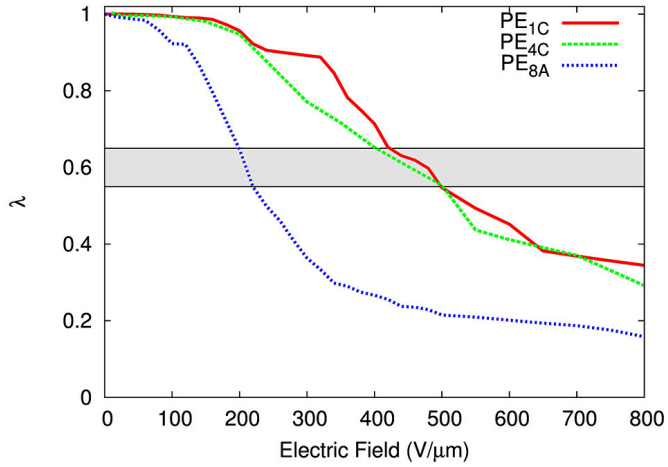

Figure 5.7: Change in thickness for the three systems of PE with respect to electric field. The grey band represents the breakdown region calculated using Stark and Garton's model.

300K. The volume was then allowed to stabilize at 300 K for 20 ns, followed by 2 ns equilibration in the canonical (NVT) ensemble. Thereafter, electric field was applied, following the same protocol as used for PE_{1C} and PE_{4C}.

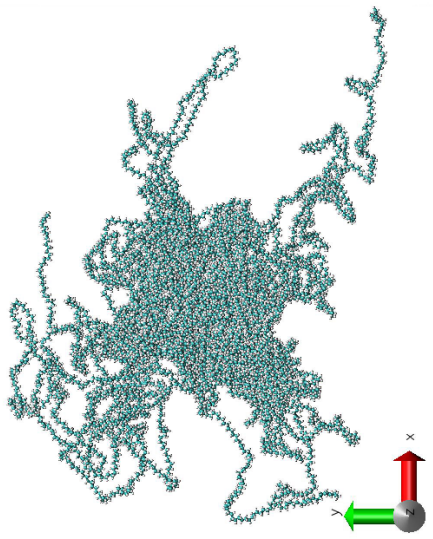

Figure 5.8: Amorphous four chains of PE containing 1000 carbons in each chain

We again a observed reduction of box size in the direction of the field (Figure 5.7).

However, the change in strain with the strength of electric field in an amorphous system was smoother and has no second (or higher) transitions at higher electric field strength, as compared to a crystalline system. Since the second transition is exclusive to crystalline systems, it is the crystalline regions in a polymer that increase the dielectric strength of a material. Furthermore, the second transition is more spontaneous which leads to catastrophic failure observed in polymeric capacitors.

5.5 Effect of polar group

After studying the effect of polar groups on dielectric constant and loss, we extend the analysis for dielectric breakdown. A system with 4.2 mol% –OH in PE was prepared following the same protocol as in our past work to get semi-crystalline PE–OH_{1C}. Additionally an eight chain system of PE–OH_{8A}, with same –OH concentration was generated. The system is cooled from amorphous state at 500K to 300K at a rate of 20K/ns. On comparing the two PE–OH systems (Figure 5.9), lower breakdown for amorphous system was again observed. Further, the breakdown of PE–OH was found to be higher than PE. Both results agreed with experimental findings[11, 37, 63].

5.6 Effect of Water and Temperature

Presence of water often leads to failure of the dielectric material at a lower electric field. It has been established that critical water is present in PE–OH[37] which

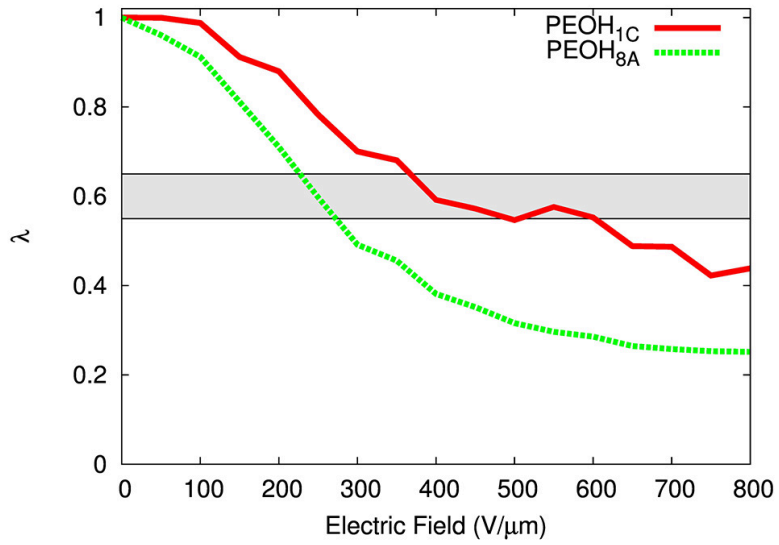

Figure 5.9: Change in thickness for the two systems of PE–OH with respect to electric field. The grey band represents the breakdown region calculated using Stark and Garton's model.

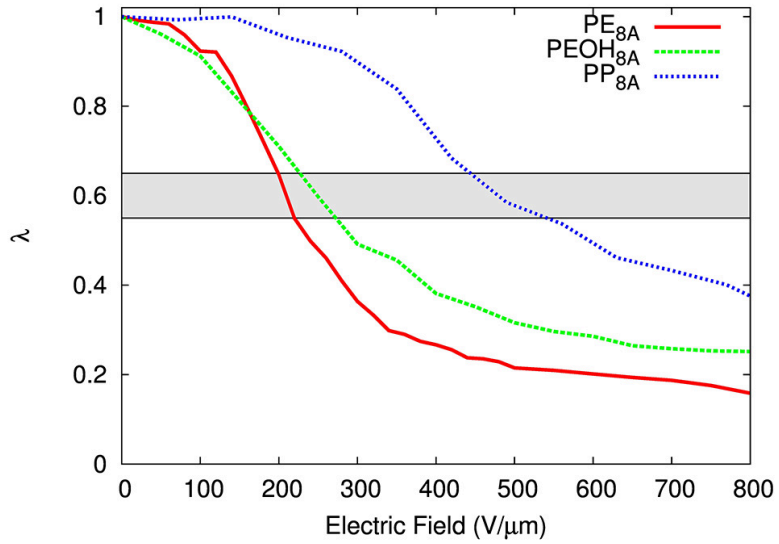

Figure 5.10: Change in thickness for the PE, PE–OH, and PP with respect to electric field. The grey band represents the breakdown region calculated using Stark and Garton's model.

should lower the dielectric breakdown. Two PE–OH systems with water, described by adding transferable intermolecular four-point potential (TIP4P) model[47], were compared to PE. The first system (PE–$OH_{1C+2.2}$) had critical amount of water (2.2

mol%), while the second system (PE–$OH_{1C+4.2}$) had excess water (4.2 mol%). The electric field was then applied to get the relationship of strain with electric field. The predicted decrease in dielectric breakdown with increase in water concentration was captured by the simulations (Figure 5.11).

The dielectric breakdown in polymers is very susceptible to temperature as shown in the figure 5.3. To study the effect of temperature, PE–OH_{1C} system was heated from 300K to 400K at rate of 20K/ns. Electric field was applied using the same protocols as the other systems to the semi-crystalline structure. The figure 5.11 shows the change in strain with electric field at 400K, and the decrease in breakdown is captured by the simulation.

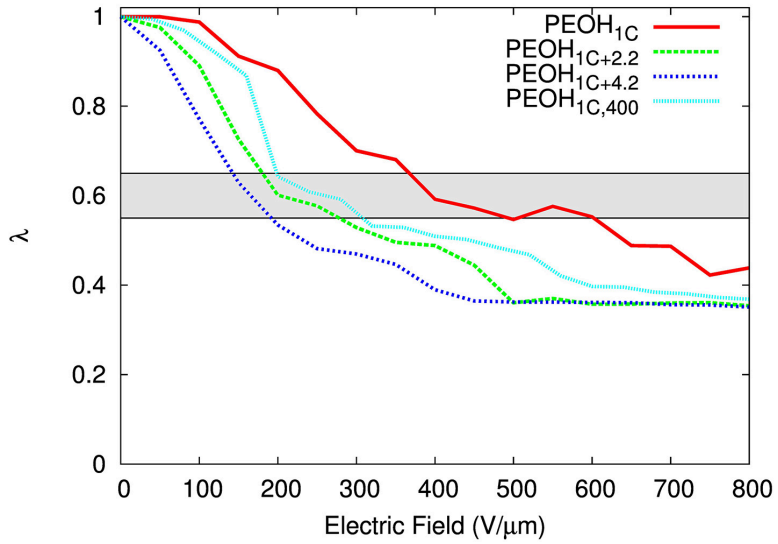

Figure 5.11: Change in thickness for the PE–OH in presence of water with respect to electric field at 300K. While cyan lines represents the change in thickness at 400K for PE–OH. The grey band represents the breakdown region calculated using Stark and Garton's model.

5.7 Polypropylene

Recent successes pertaining to the study of electromechanical breakdown in PE and PE–OH systems have encouraged us to study other polymers. Polypropylene (PP) is considered as a state-of-the-art polymeric capacitor material. Therefore, it is of interest to study behavior in the presence of an electric field compared to PE and PE–OH. Experimentally, it is seen that PP has a higher dielectric breakdown as compared to PE (Figure 5.3). In MD simulation, crystallization of PP is hard to simulate[29]. Consequently, amorphous PE and amorphous PP were compared.

Eight chains of polypropylene (PP_{8A}) with 1000 backbone carbon atoms in each chain at 1000K and 1 bar. The system was then cooled to 300 K at a rate of 100K/ns where the system was still in amorphous state. The volume was then allowed to stabilize at 300 K for 5 ns, followed by 2 ns equilibration in the canonical (NVT) ensemble. Thereafter, the electric field was applied following the same protocol as above, and strain was calculated (Figure 5.10). The critical electric field at which the thickness drastically decreases in PP is higher than PE which quantitatively agrees with experimental results.

Comparison to Stark and Garton

The dielectric breakdown can be calculated for all our simulated systems using Stark and Garton's prediction of breakdown at $\lambda = 0.6$. The figure 5.12, shows the predicted breakdown for all the simulated systems. The breakdown is not affected by the field direction for amorphous systems. However, the dielectric breakdown is much higher

when field is in parallel to c-axis.

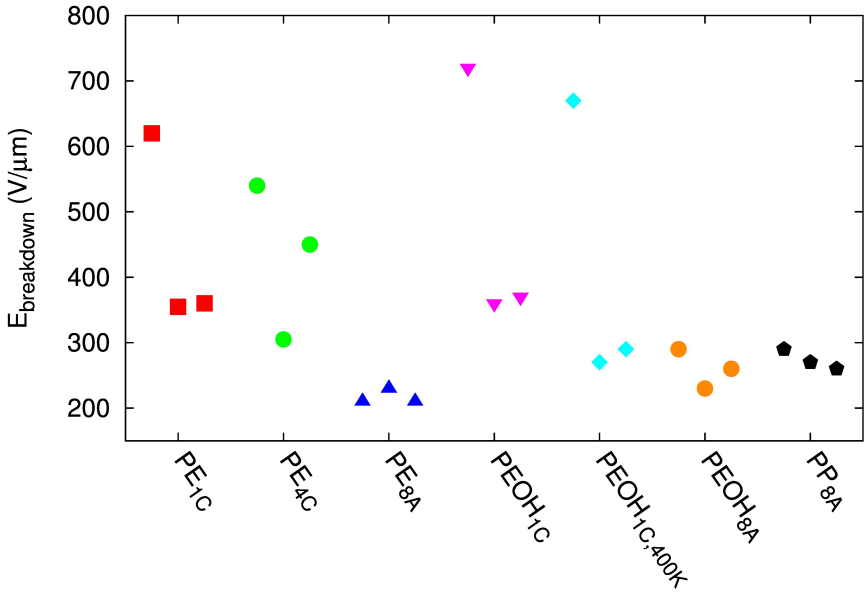

Figure 5.12: Breakdown predictions for simulated systems using Stark and Garton's model.

5.8 Theoretical Models

Neo-Hookean Model

Stark and Gartons model predicts thickness at critical electric field but it does not account for the incompressible nature of polymer chains. A widely used model for prediction of mechanical properties in polymers is the neo-hookean model, where strain energy density is given by

$$W = \frac{1}{2}G(trace(F^T F) - 3) - \alpha(|F| - 1) \tag{5.3}$$

where G is the shear modulus and α is lagrangian multiplier. Since deformation in the figure 5.1 is in two in–plane directions without any other external force $\lambda_1 = \lambda_1 = \lambda_3^{-1/2} = \lambda^{-1/2}$ and

$$W = \frac{1}{2}G(\lambda^2 + 2\lambda^{-1} - 3) - \frac{\lambda^2 D^2}{2\varepsilon} \tag{5.4}$$

Assuming that Helmholtz free energy (A) of a polymer in an electric field (Figure 5.1) is a function of deformation gradient and electric displacement, then, $\delta A(F, D) = s\delta F + E\delta D$ and;

$$s = \frac{\delta A(F, D)}{\delta F} \tag{5.5}$$

$$E = \frac{\delta A(F, D)}{\delta D} \tag{5.6}$$

Where s is the stress and E is the nominal electric field. On substituting equation 5.4 in equation 5.5 and equation 5.6 we get

$$s = G(\lambda + \lambda^{-2}) - \frac{\lambda^2 D^2}{\varepsilon} \tag{5.7}$$

$$E = \frac{\lambda^2 D^2}{\varepsilon} \tag{5.8}$$

Since there is no external surface force being applied, the material we find $D = \sqrt{G\varepsilon(\lambda^{-3} - 1))}$ using equation 5.7 and we substitute this value to equation

5.8 to get a relationship between electric field and strain as

$$\frac{E}{\sqrt{G/\varepsilon}} = \sqrt{\lambda - \lambda^4} \tag{5.9}$$

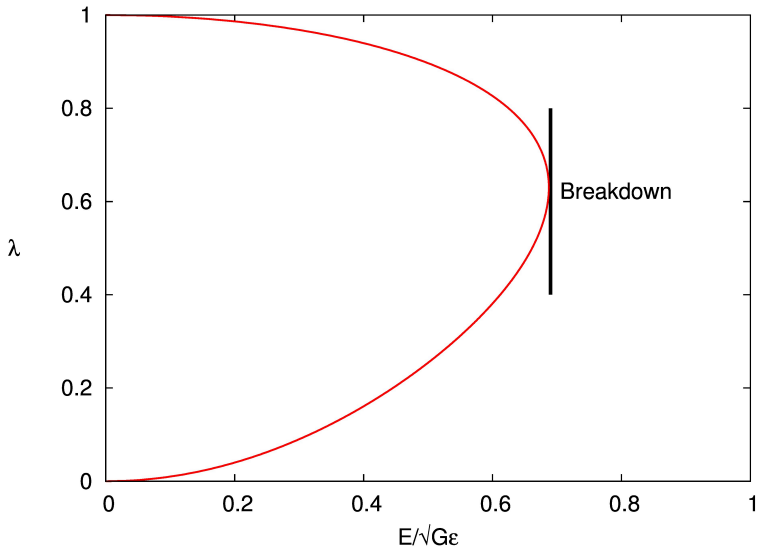

Figure 5.13: Variation of electric field as a function of strain derived using neo-hookean model (equation 5.9).

By using equation 5.9, we observe that the electric field is maximum at $\lambda = 0.63$ and maximum nominal electric field is given by $E_{max} = 0.69\sqrt{G/\varepsilon}$. The critical strain conditions are in agreement with both the experiment performed by Stark and Garton and simulations for PE.

Gent Model

Although the incompressible neo-hookean model explains the critical breakdown and behavior at high strains observed in the simulations reasonably well, it fails to describe the behavior detected at low strains. This failure at low strains is due

to the failure of neo-hookean model since it ignores the stiffness of a polymer chain. Several empirical relations have been suggested to account for this stiffness to define mechanical properties at higher strains[95–99]. For our calculation, we use the Gent model[100]. For deformation in the figure 5.1, the strain energy using Gent model is given by

$$W = -\frac{1}{2}GJ_m ln\left(1 - \frac{\lambda^2 + 2\lambda^{-1} - 3}{J_m}\right) - \frac{\lambda^2 D^2}{2\varepsilon} \tag{5.10}$$

Here, G is the shear modulus and J_m is the stiffness parameter which has been statistically proved to depend on the number of Kuhn segments. On substituting equation 5.10 in equation 5.5 we get

$$S = \frac{GJ_m}{J_m - \lambda^2 + 2\lambda^{-1} - 3} - \frac{\lambda^2 D^2}{\varepsilon} \tag{5.11}$$

since there was no external surface force being applied the material in the figure 5.1, we find $D = \sqrt{\frac{\varepsilon G J_m(\lambda^{-3}-1)}{(J_m+3)\lambda - 2 - \lambda^3}}$ using equation 5.11. And we substitute this value to equation 5.8 to get a relationship between electric field and strain as

$$\frac{E}{\sqrt{G/\varepsilon}} = \sqrt{\frac{J_m(\lambda - \lambda^4)}{(J_m + 3)\lambda - 2 - \lambda^3}} \tag{5.12}$$

Figure 5.6 depicts the variation of electric field as a function of strain, as defined equation 5.12 . The strain at inflection obtained from gent model also agrees with the other models described above. Gent model also describes the low strain behavior observed in simulations aswell. We fit equation 5.12 to our simulation results in

the figure 5.14 and find the shear modulus to be 54MPa, 47MPa, and 51MPa when electric field is passed in x, y, and z directions respectively. While we find J_m to vary significantly from 1.7 for system when electric field is passed in x direction to 10.2 when it is passed in y-direction. This change is value for J_m shows its dependence on crystal direction.

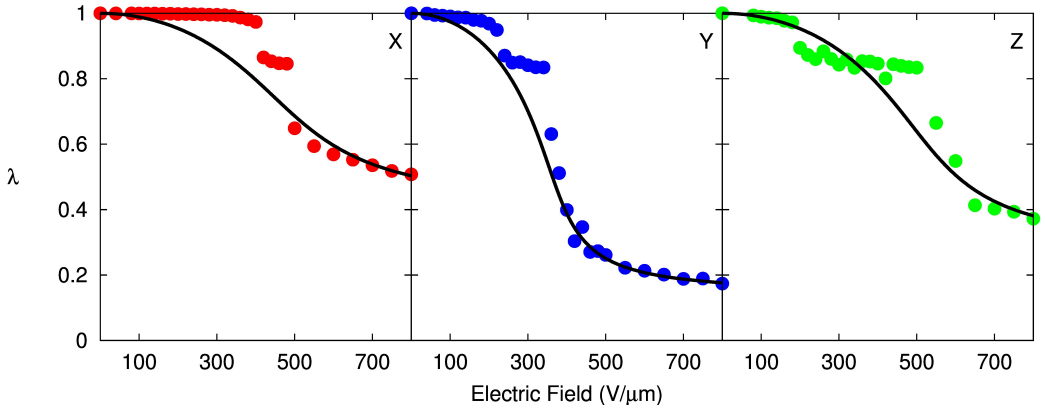

Figure 5.14: Gent model fit for simulation of PE in presence of external electric field in (a) x-direction, (b) y-direction and (c) z-direction

Bead-Spring Model

The Gent model is able to define the mechanics, but it is an empirical model and lacks in defining the physics. To understand the underlying physics in presence of an electric field, bead-spring model can be used. In the model, when an extension force is applied to the system, the end to end distance is described by the Langevin Function

$$\frac{\langle R \rangle}{Nb} = \coth\left(\frac{f \cdot b}{kT}\right) - \frac{1}{\frac{f \cdot b}{kT}} \tag{5.13}$$

where, f is the force, b is the kuhn length and R is the end to end distance. In our simulation, $f \approx -qE$ and unidirectional, hence the end to end distance changes to

$$\frac{\langle R \rangle}{Nb} \approx \coth\left(\frac{-qEb_x}{kT}\right) - \frac{1}{\frac{-qEb_x}{kT}} \tag{5.14}$$

But the force is not exactly equal to E and box size is also equal to end to end distance, so making the substitution

$$\frac{\langle R \rangle}{Nb} \rightarrow \frac{\langle R \rangle}{Nb} + n \tag{5.15}$$

$$E \rightarrow E + p \tag{5.16}$$

Hence equation 5.14 becomes

$$\frac{\langle R \rangle}{Nb} = \coth\left(-\frac{qEb_x}{kT} - \frac{qpb_x}{kT}\right) - \frac{1}{-\frac{qEb_x}{kT} - \frac{qpb_x}{kT}} + n \tag{5.17}$$

The modified langevin function (Equation 5.17) can be fitted to all the simulations, to find the parameters for each system. The obtained parameters are plotted against the predicted dielectric breakdown in Figure 5.15. A linear positive trend between the inverse product of charge and kuhn length, and the dielectric breakdown is observed. The two outling points are obtained strains for PE–OH system at 300K and 400K when field is passed in x-direction (Figure 5.15). This high breakdown in the system is occuring because the field is parallel to c-axis and absence of bond breaking. The positive correlations are encouraging, but more analysis needs to be

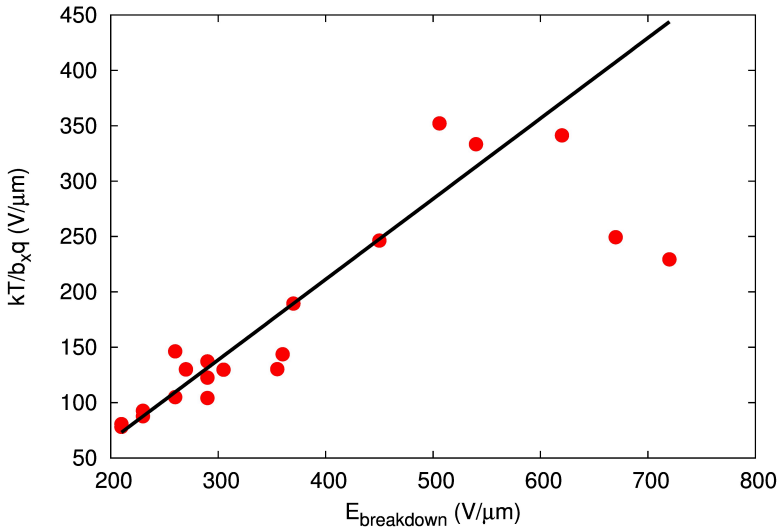

Figure 5.15: Comparison of modified langevin parameters to breakdown field.

done for understanding dielectric breakdown relationship with charge and kuhn lenght theoretically.

5.9 Discussion

In this chapter, we developed a methodology for mimicking electromechanical breakdown, as seen in the experiments. We used the developed scheme to systematically compare the effect of side groups (–OH and –CH_3), system size, crystallinity, water, and temperature for various samples. We observed quantitative agreement of simulations results with experimentally known data. To delineate the mechanism of electromechanical breakdown we calculate the local stresses in the system. We employ the technique used by Zhou et. al. [101] for calculating the atomic stress, where the local stress is given by

$$\sigma_i = \sum_{i \neq j} \frac{1}{V_i} r_{ij} \otimes f_{ij} \tag{5.18}$$

where Vi is the volume surrounding particle i, and r_{if} and f_{if} are the distances and forces between particles i and j, respectively. Since calculating the volume of each particle can be computationally expensive, we approximate $V_i = V_{box}/n$. Another constraint in using equation 5.18 is that the force is required to be two-body interaction but the OPLS potential has angles and dihedrals which are multi body interactions. Zhang et. al developed a method to decompose these three-body potential energy functions (angle potentials) into the sum of two-body forces. [102]. Later the approach was extended to four-body potentials [103] thereby permitting direct application of equation 5.18 to three and four-body potentials.

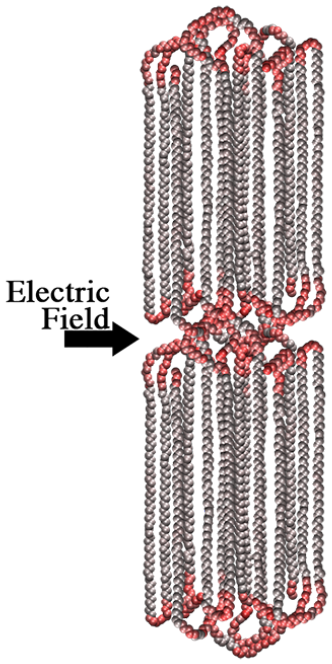

Figure 5.16: Periodic image of PE_{4C} representing the local stress distribution in the sample. The high and low stress regions are represented by red and gray color respectively.

The figure 5.16 is the snapshot of the periodic images of PE_{4C} under the effect of the electric field (E=700 V/μm). The calculated local stress is represented as color gradient for the carbons, high local stress is represented by red while gray represents low local stress. As seen in the figure, the crystalline regime is predominately low-stress region while there is a high concentration of stress in the interphase/non-crystalline regime.

To measure principal contributor to high local stress, we measure the bond length, angle, and dihedral between each pair of bonded atom and average it over the last 100 ps of the simulation. The calculated increase is found to be mainly due to the increase in the bond length between few atoms. The figure 5.17a shows the distribution of C–C bonds for various electric field applied in the x-direction. The distribution peak for bond length distribution is weakly dependent on the applied electric field, but the distribution width if found to increase drastically with the increase in applied electric field. The cause of the low dependency is due to the high crystallinity in the sample, where the carbons are more stable and show negligible displacement from the mean position with the increase in the electric field, figure 5.17b. However, the peak of the distribution of the non-crystalline regime shifts by a significant measure (Figure 5.17b). This observation is consistent with the local stress calculation, where the non-crystalline region is under high local stress. Under these forces/extension, the OPLS force field does not represent the system correctly, as it assumes the bond to be rigid and non-breakable. In the subsequent chapter, we will introduce the bond breaking to our simulations and thus, try to understand the mechanism behind the electromechanical breakdown.

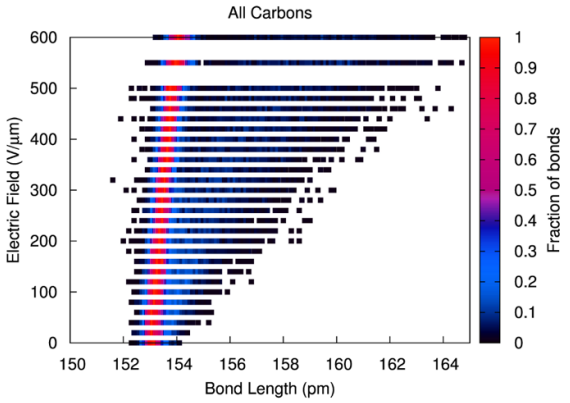

a)

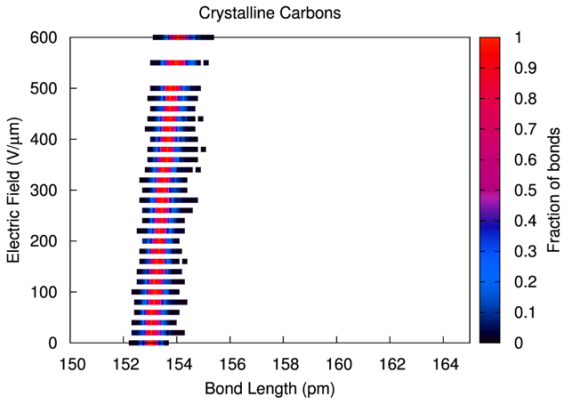

b)

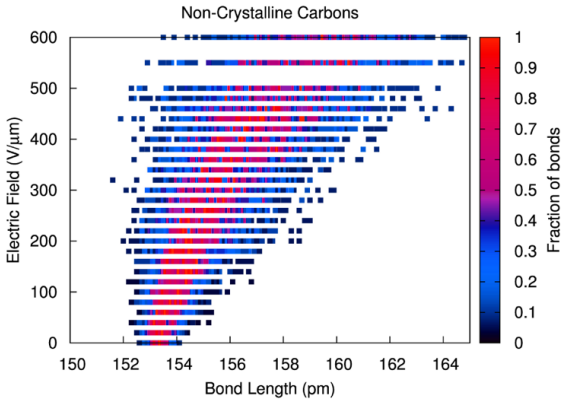

c)

Figure 5.17: C–C bond length distribution for (a) whole sample, (b) crystalline, (c) and non-crystalline regime as a function of field strength in the x-direction.

Chapter 6

Bond Breaking

Bond breaking has been included in coarse-grained simulations extensively[104, 105], but extension of it to all–atom simulations has been complicated. The functional form of the OPLS-AA force field is given by

$$E(r^n) = E_{LJ} + E_{coulombic} + E_{bond} + E_{angle} + E_{dihedral} \tag{6.1}$$

where bond energy is a harmonic function, which is stiff in nature. Due to less flexibility, the bond breaking energy is achieved at relatively low bond extensions. Van der Waals interactions are triggered when the bond is allowed to break. At this small deformation there is a huge overlap between the atoms and unrealistic energies in the simulations are observed.

In this chapter we will be exploring the methodologies to overcome these issues associated with OPLS potential and use the modified potential to study the response of polyethylene to applied external electric field.

6.1 Modified Morse Potential

Bond length potential models the potential energy for a stretched bond. As mentioned above the OPLS force field uses the harmonic potential which is commonly used in many all-atom MD simulations. The Harmonic potential is represented as: $E_H^b(r) = K(r - r_m)^2$. Here r_m is the reference bond length, while K is the energy parameter, seen by the interatomic force given by the harmonic potential: $F_H^b(r) = 2K(r - r_m)$. This is Hookes law, where $2K$ is the spring constant. This potential standalone gives a linear elastic material behavior. A chain with these bonds could be seen mechanically as linear elastic springs connected in series. The values for Carbon – Carbon bond in OPLS are: $r_m = 1.529$ Å and $K = 224.262$ kcal/mol.

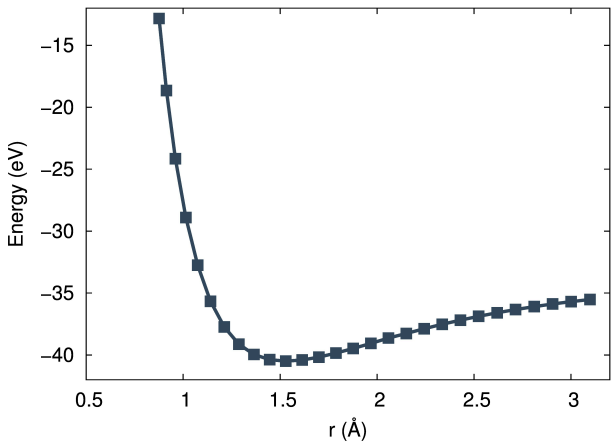

Figure 6.1: Energy of two isolated CH_3* radicals with respect to the distance between calculated using DFT.

The harmonic potential is reliable when the bond lengths are not far away from the reference bond length. However, we know that the potential energy between two atoms does not go to infinity when the bond is stretched. There have been ways of trying to fit curves such as Figure 6.1 to a simple potential. The Lennard-

Jones potential works, but a much better fit is the Morse potential, given as: $E_M^b(r) = A[1 - e^{-\alpha(r-r_m)}]^2$. Where A is the potential energy at infinite bond length, and thus traditionally considered as the bond dissociation energy. Hence, inspired by the work of Popov. et. al[106] on bond dissociation simulations we will use a modified Morse bond potential given by:

$$E_M^{bb}(r) = \begin{cases} A[1 - e^{-\alpha(r-r_m)}]^2 & r < r_c \\ \\ 0 & r > r_c \end{cases}$$

Here there are three parameters A, α and r_c. We will now discuss the various methods to determine each parameter and its implementation in LAMMPS.

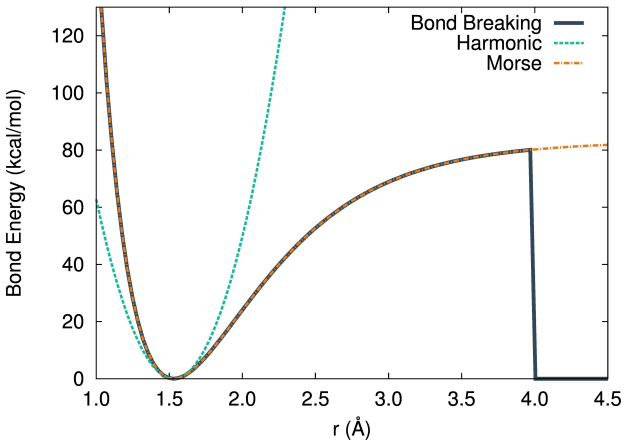

Figure 6.2: The Harmonic and Morse bond potential with parameters compared to the bond breaking potential used in simulations.

Determining Parameters

To estimate the bond energy potential of a Carbon – Carbon bond we measured the dissociation energy of the bond in ethane (C_2H_6) using density functional theory.

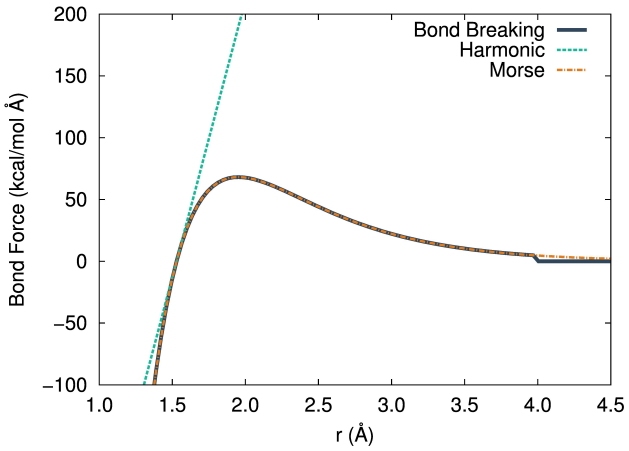

Figure 6.3: The Harmonic and Morse bond force with parameters compared to the bond breaking force used in simulations.

We used Heyd-Scuseria-Ernzerhof (HSE) exchange-correlation energy functional for performing the mentioned DFT simulations. We first considered an isolated C_2H_6 molecule and found its ground state energy to be -44.55 eV. Following that we calculated the energy of two isolated CH_3* radicals with respect to the distance between them as shown in Figure 6.1. The net difference in the ground state energies would give the bond energy as 4 eV or 92 kcal/mol which is close to experimental value of 90.2 kcal/mol [107]. Note that the dissociation energy here encompasses bond length, angle, and dihedral energy. Hence to estimate the bond energy constant for Morse potential we need to find the contribution due to angle and dihedral terms. When Carbon – Carbon are at a distance of 4 Å the energy contributions of angle and dihedral is 5.6 and 3.3 kcal/mol respectively. Therefore we use 83.01 kcal/mol as bond energy parameter (A) for the Morse potential. This value is in sync with earlier estimated values for the mimicking thermal degradation polyethylene [108].

To calculate α we relate the Morse potential to the harmonic potential by applying

a second order Taylor expansion around $r = r_m$

$$\begin{aligned} E(r)|_{r=r_m} &= E(r_m) + \tfrac{(r-r_m)}{1!}E'(r_m) + \tfrac{(r-r_m)^2}{2!}E''(r_m) \\ &= 0 + \tfrac{(r-r_m)}{1}0 + \tfrac{(r-r_m)^2}{2}2\alpha^2 A \\ &= (r-r_m)^2\alpha^2 A \end{aligned}$$

The potential now resembles the harmonic bond length potential, where

$$\begin{aligned} \alpha^2 A &= K \\ \alpha &= \sqrt{\tfrac{K}{D}} = 1.64 \end{aligned}$$

The energy and force relationship for the defined Morse potential is compared to Harmonic potential in Figure 6.2 and 6.3. As seen in the figure the energy reaches an asymptotic limit at large distances and can carry on till infinity, which is not physical. Here we propose the concept of bond breaking/dissociation. From a quantum chemical perceptive, breaking a bond is a trivial process. Excitation of a critical number of electrons in the bonded orbitals, so that more electrons are antibonding than bonding. This requires some activation energy, which we have already calculated for the Morse potential. By increasing the separation between atoms, the electrons in a sigma bond will in average be longer and longer separated from the nuclei, giving a greater energy for the system as seen in Figure 6.1. This is the nature of a realistic bond length potential and Morse potential mimics it very closely.

To calculate the critical bond breaking length we consider a polymer molecule having one end fixed and a force acting on the other end, as shown in Figure 6.4. We consider the polymer to be a chain of N units bonded together by bonds obeying the Morse potential being stretched by a unidirectional force F. We can denote the

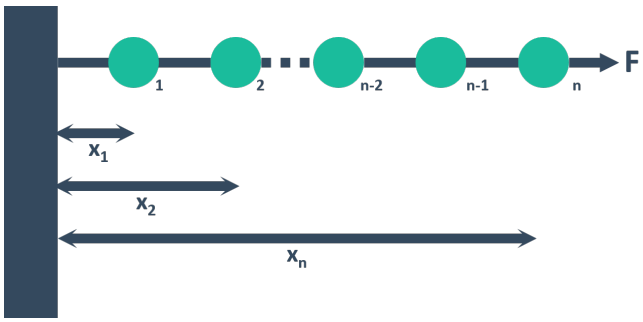

Figure 6.4: Definition of single-particle coordinates investigated consisting of N units joined together by bonds obeying the Morse potential. It is fixed at one end and is acted upon by a force F at the other end.

position of the nth atom as x_n and taking the number of bonds to be N-1, we can write the potential energy of the system to be

$$E^m_{total} = \sum_{n=1}^{N-1} E^m(x_n - x_{n-1} - r_m) - Fx \tag{6.2}$$

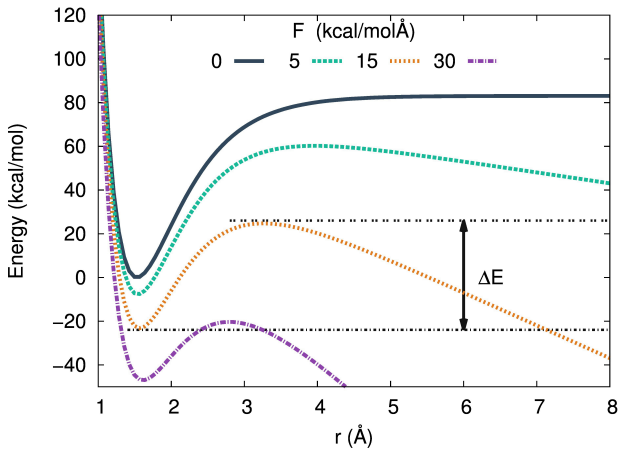

Figure 6.5: The modified Morse potential under external force for various values of F. ΔE is the activation energy when F = 15 kcal/molÅ.

where r_m is the equilibrium bond length. The force can be scaled to $\tilde{F}$, where $F = \frac{\alpha A}{2}\tilde{F}$. The potential is plotted versus r in Figure 6.5 for various $\tilde{F}$ values and $b = 1.529$. As seen in the figure, the potential has two stationary points, one at the

potential minimum r = r_{eq} and one at the saddle point, r = r_b given by

$$r_{eq} = r_m + \frac{1}{\alpha} ln \left(\frac{2}{1 + \sqrt{1 - \tilde{F}}} \right) \tag{6.3}$$

$$r_m = r_m + \frac{1}{\alpha} ln \left(\frac{2}{1 - \sqrt{1 - \tilde{F}}} \right) \tag{6.4}$$

and the activation energy will be given by

$$\Delta E = A \left[\sqrt{1 - \tilde{F}} + \frac{\tilde{F}}{2} ln \left(\frac{1 - \sqrt{1 - \tilde{F}}}{1 + \sqrt{1 - \tilde{F}}} \right) \right] \tag{6.5}$$

The bond will break when the energy barrier disappears (at $\tilde{F} = 1$), where the r_m and r_{eq} merge at a saddle point. This point can be estimated to be

$$r_b = r_m + \frac{ln(2)}{\alpha} \approx 2\text{Å} \tag{6.6}$$

This point is a metastable state, and if the bond is slightly extended the potential energy will irreversibly drive the atoms away from each other leading to bond breaking. We argue that breaking of the bond below this critical distance will give incorrect dynamics. Note that if we break the bond at this critical distance the atoms feel sudden increased force leading to acceleration, which requires us to decrease the timestep of the simulation. Hence, in our simulations we break the bond at 4 Å which allows us to capture the bond dissociation dynamics without significantly compromising simulation timestep. We acknowledge that this will increase the amount of energy required to break the bond, which would manifest itself as a larger

perceived dissociation energy ($\approx$ 105 kcal/mol).

Implementation in LAMMPS

LAMMPS has implemented a method to break bonds using fix bond/break. The algorithm deletes the bond between atoms when they are further away than a pre-described length r_{cutoff}, with an optional probability of success. The proposed fix is an effective way of implementing the bond breaking. However, there are some tweaks required before we can apply it to our system. In the fix, the angle and dihedral interactions over the bonds are considered to be independent of the bond break and are kept in this system even when the bond is deleted. This implies that these potentials will still be accounted in the energy calculations, giving rise to a lower entropy. Hence the code was extended to ignore angles and dihedrals once the bonds are broken.

Another disadvantage in the using this fix is that it requires special bonds constraint as `0 1 1`. This fix controls the LJ interactions between 1-2 atoms, 1-3 and 1-4 neighbors respectively. So the command `0 1 1` means that there will be no LJ between 1-2 atoms, while there will be full LJ interactions for 1-3 and 1-4 atoms. This interaction is unreliable for all-atom simulations where the bond length is smaller than the LJ radius of atoms. The repulsion between 1-3 atoms is unrealistic, and OPLS force field is optimized to consider it as 0. OPLS also assumes the 1-4 interactions as half of the calculated value. Thus, to use this fix for all-atom simulations, the code was modified to implement specified interactions between 1-3

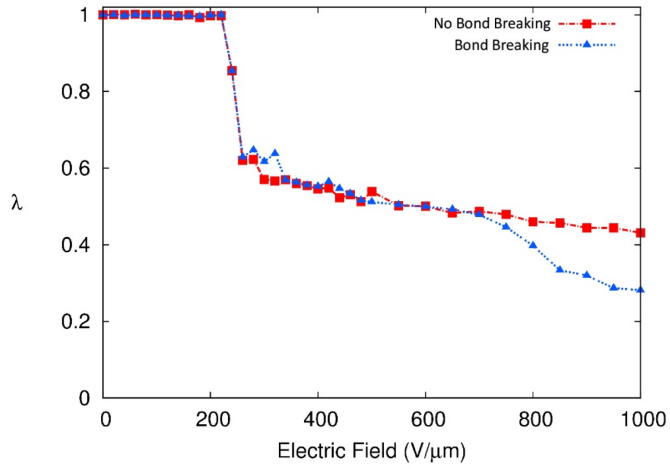

a)

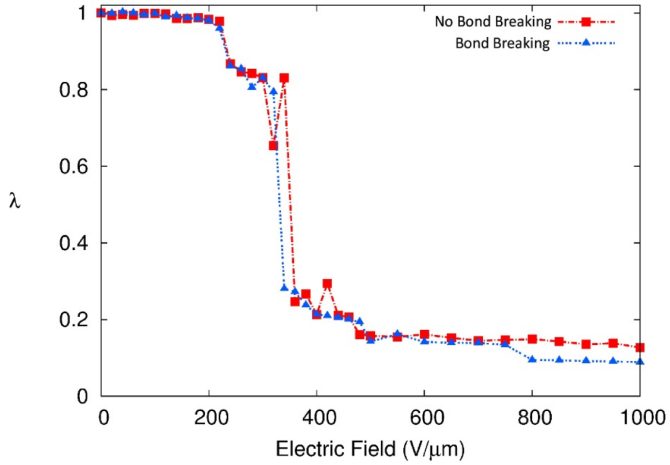

b)

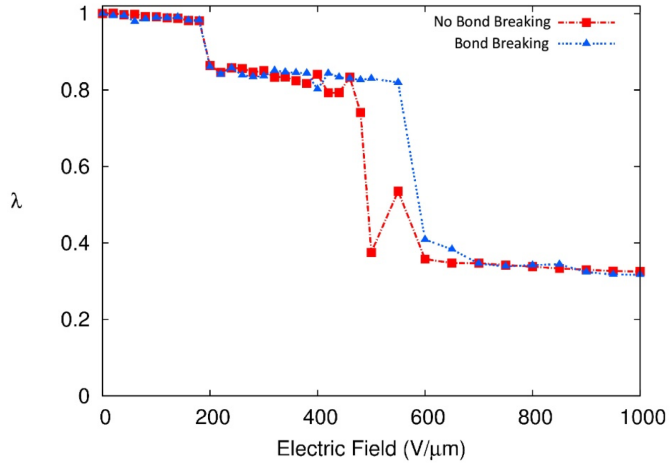

c)

Figure 6.6: The electric field and λ relationship for (a) x , (b) y, and (c) z-directions both the bond potential were found to be similar in all the cases

and 1-4 atoms correctly.

6.2 Bond Breaking in Simulation

The protocol developed for the introduction of the electric field in the system with harmonic bonds was carried forward for the modified bond potential. The unidirectional field was applied in isothermal–isobaric ensemble (NPT) and the field was ramped up to the desired electric field voltage at a rate of 50 V/μm per ns. The systems were then allowed to equilibrate at the desired electric field for 2ns followed by calculation of the box size in the field direction averaged over the last 500 ps. The average box size in the field direction relative to the initial box size in the direction gives us strain (λ) for the specific electric field voltage. For isotropic averaging, unidirectional field was applied in each the X, Y, and Z-direction.

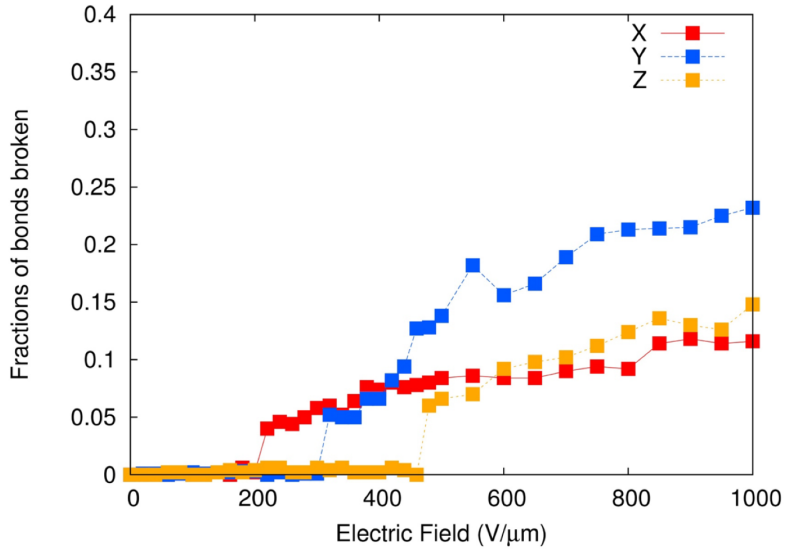

Figure 6.7: Fraction of C–C bonds broken in the simulation due to application of electric field.

The electric field and λ relationship for both the bond potential are comparable in all the cases (Figure 6.6). The similarity between the two flavors of simulations implies that the change of potential has no effect on the macroscopic quantity i.e. the dielectric breakdown. However, on analyzing the system, we observe a significant amount of bonds are broken in the systems. The onset of bond breakage is the point of failure and will lead to the breakdown of the material. The electric field at which the first bond is broken is thus the dielectric strength of the polymer.

The isothermal–isobaric ensemble (NPT) was used to perform the simulations mentioned above where a thermostat is applied. Hence in the case when a bond breaks the increased kinetic energy of the atoms is removed from the system. This removal of energy leads to loss of memory of broken bonds, and the resultant sample has now $(n + 1)$ chains in the system. However, in reality, bond breaking should be a cascading/snowball effect where a broken bond results in an avalanche of broken bonds. Thus, to mimic this effect we use isoenthalpicisobaric ensemble (NPH) which is analogous to the microcanonical ensemble. In standard microcanonical, the volume is set and the pressure is determined only after the end of the simulation as an averaged quantity. If the goal is to compare with the experiments, then a fixed pressure is also desired. One procedure would be to vary the size of the simulation cell until the desired pressure is obtained, similar to the procedure to the scaling of the velocity to obtain the desired temperature. Moreover, for the constant pressure case, the enthalpy (H = E + PV) is constant for the simulation, not the energy.

The protocol developed for the introduction of the electric field in the system with harmonic bonds was carried forward for the modified bond potential. The

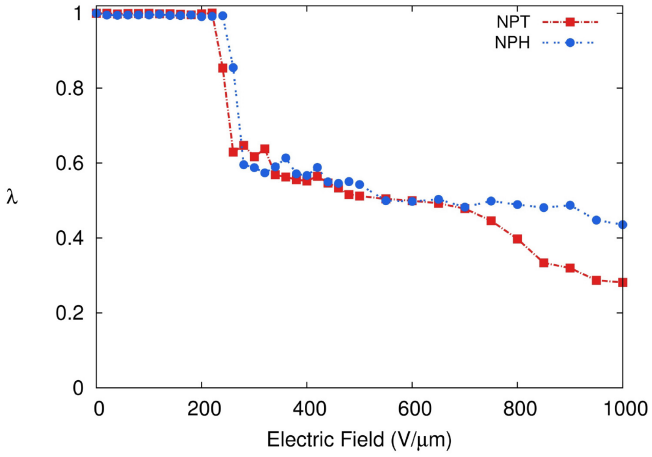

a)

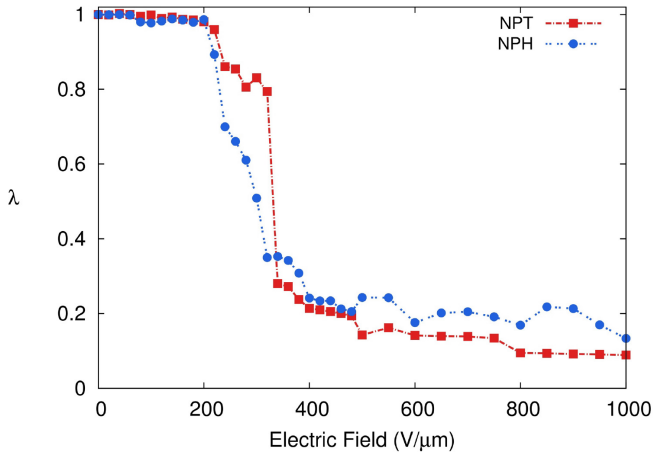

b)

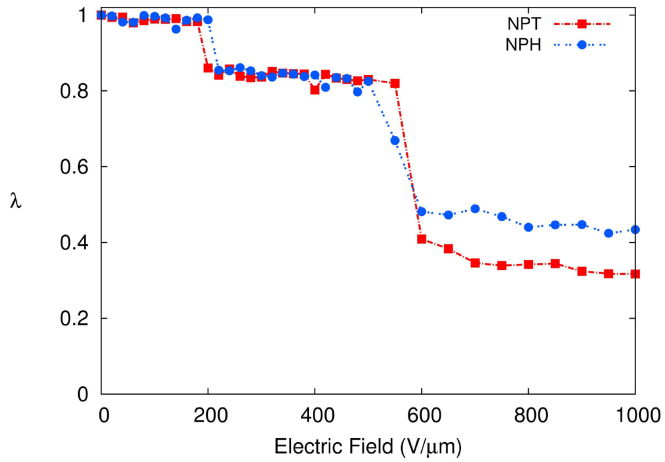

c)

Figure 6.8: The electric field and λ relationship for (a) x , (b) y, and (c) z-directions for the NPT (blue) and NPH (cyan) ensembles.

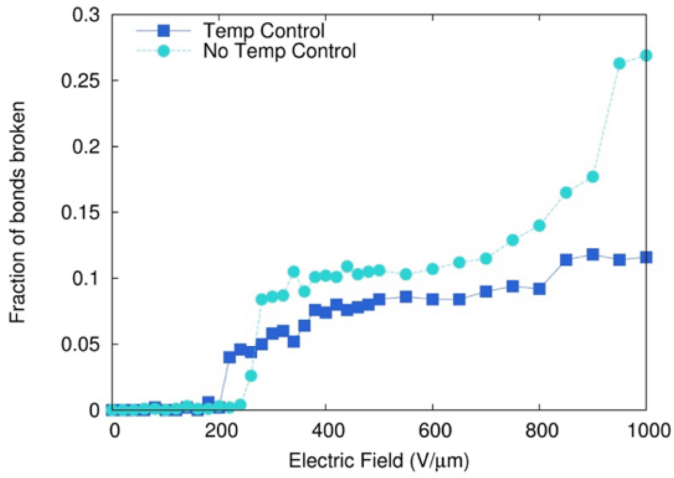

a)

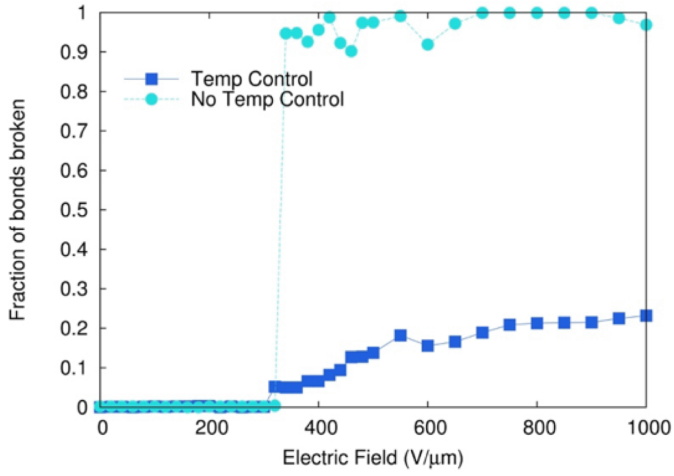

b)

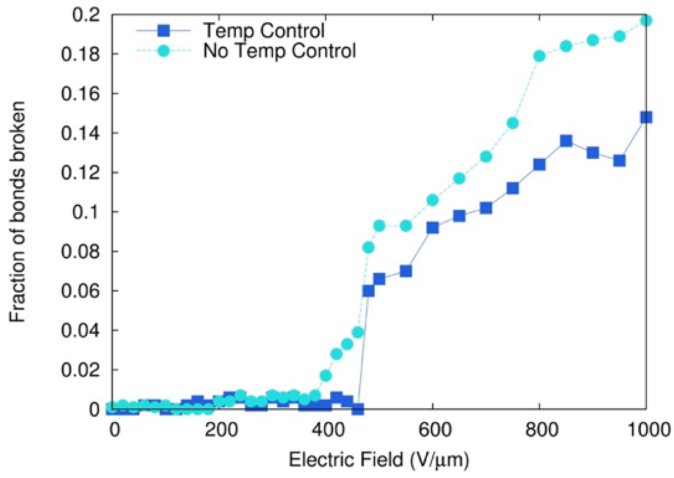

c)

Figure 6.9: Fraction of C–C bonds broken in the simulation due to application of electric field in (a) x , (b) y, and (c) z-directions for the NPT (blue) and NPH (cyan) ensembles.

unidirectional field was applied in isothermal–isobaric ensemble (NPT) and the field was ramped up to the desired electric field voltage at a rate of 50 V/μm ns. The systems were then allowed to equilibrate at the desired electric field for 2ns followed by calculation of the box size in the field direction averaged over the last 500 ps. The average box size in the field direction relative to the initial box size in the direction gives us strain (λ) for the specific electric field voltage. For isotropic averaging unidirectional field was applied in each the x, y, and z-direction.

Before application of the electric field, the sample of PE chain initially at 300 K was equilibrated under NPH ensemble for 5 ns. The temperature was monitored during the 5 ns simulation and was observed to fluctuate around 300 $\pm$ 5 K for the chosen barostat parameters. Once the sample was equilibrated, the protocol developed for the introduction of the electric field in the systems mentioned above was reapplied for this sample. However, the unidirectional field was applied under NPH ensemble and not in NPT ensemble. The electric field was ramped at the rate of 50 V/μm per ns to the desired field, followed by equilibration at the desired field for 2 ns. Thereafter, the box size in the field direction was averaged over the last 500 ps for calculation of strain (λ) at the applied external field.

The electric field and strain relationship obtained is comparable to the one obtained under NPT conditions 6.8. Hence all the three flavors of simulations (no bond breaking, bond breaking with temperature control, bond breaking without temperature control) give similar results when we only compare the electric field relationship with strain. This similarity in results implies that the mechanism of bond breaking is not captured in the experimentally observed field–strain curve.

However, on comparing the fraction of bonds broken in the samples in different ensembles we observe catastrophic failure in case of no temperature control (NPH). The temperature fluctuates around 310 – 320 K during initiation of bond breaking (¡ 1%). However, the temperature exponentially increases to above 500 K as 2% of the bonds are broken in the system leading to disastrous failure of the material.

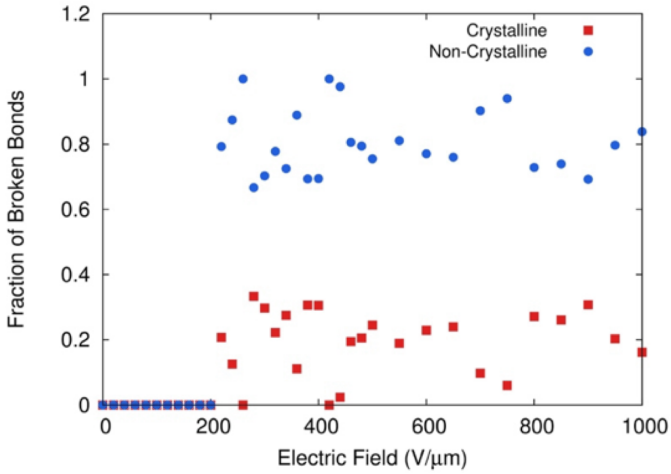

Figure 6.10: Comparison of fraction of C–C bonds broken in crystalline versus non-crystalline regime in the simulation due to application of electric field in the x-direction.

We determine the regime of failure or bond breakage by first marking the carbon as crystalline or non-crystalline before the external electric field is applied. At the end of each simulation (various applied electric field), we count the numbers of carbons with bonds broken. The number of crystalline and non-crystalline carbons with bond breakage normalized by the total number of bonds broken in the system when the electric field is applied in the x-direction is shown in figure 6.10. The bonds are primarily broken in the non-crystalline regime. This result is consistent with the presence of high local stress in the region (Figure 5.16).

6.3 Electro–fracture

The Stark and Garton's model of breakdown implicit to the analysis is unrealistic as it assumed the dielectric material disappeared to an infinitesimal thickness at $E > E_{bd}$. It also ignores plastic flow and the dependence of Young's modulus on time and stress. Due to these reasons, the model fails to explain electromechanical breakdown in various polymers [109]. As observed in the last section there are microscopic areas of stress concentration leading to instability which may give rise to a localized breakdown. This propagation of the "crack" in the material is the principle behind fracture mechanics.

A. A. Griffith during World War I laid the foundation for Fracture mechanics, to explain the failure of glassy materials [110]. There were two conflicting facts that motivated Griffith's work. The stress required to fracture bulk glass is in the order of 100 MPa while the theoretical stress needed for breaking an atomic bond is 2 orders of magnitude larger. Griffith suggested that the low fracture strength observed in the experiments was due to the presence of microscopic defects in the bulk material.

To verify the hypothesis, Griffith introduced an artificial crack in the glass specimens. The experiments showed that the product of the square root of the crack length (a) and the stress at the fracture (σ_f) was nearly constant, which is expressed by the equation: $\sigma_f \sqrt{a} \approx C$. This relation is inconsistent with linear elasticity theory by Inglis [111]. Linear elasticity theory predicts that stress at the tip of a sharp flaw is infinite. To avoid that problem, Griffith developed a thermodynamic approach to demonstrate the relation observed by him.

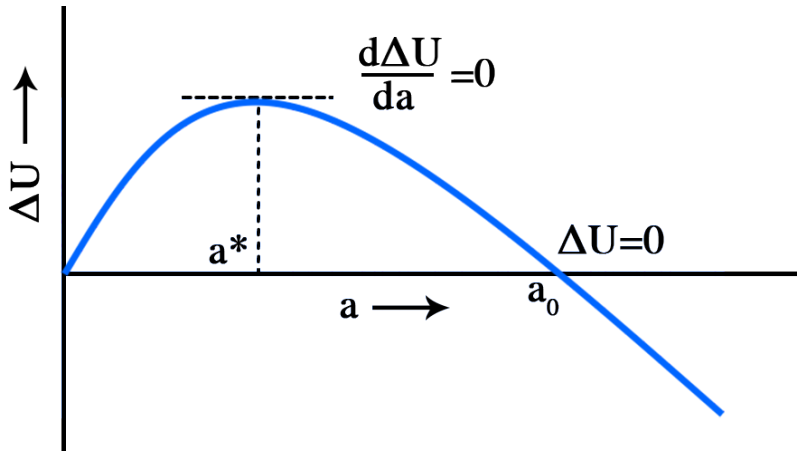

Figure 6.11: Energy potential for crack propagation.

The growth of a crack requires the creation of two new surfaces and hence an increase in the surface energy. The energy for creating 2 surfaces can be given by $4\gamma a$, where γ is the surface energy of the material. While the reduction in elastic energy is $\pi a^2\sigma^2/Y$, where Y is the Young's modulus of the material. Hence the change in the energy will be given by: $\Delta U = 4\gamma a - \pi a^2\sigma^2/Y$, shown in figure 6.11. The fracture is observed at $a*$, which can be calculated using $\frac{\Delta U}{da} = 0$. On solving the equation we get $\sigma_f\sqrt{a} = \sqrt{2\gamma Y/\pi}$, where the right hand side is a constant and justifies the experimental observation. This relationship holds true for all glassy materials, however for ductile materials the surface energy (γ) predicted by Griffith's theory is unrealistically high. During World War II, Irwin realized that plasticity must play a significant role in the fracture of ductile materials [112].

This relationship holds true for all glassy materials, however for ductile materials the surface energy (γ) predicted by Griffith's theory is unrealistically high. During World War II, Irwin realized that plasticity must play a significant role in the fracture of ductile materials [112]. In ductile materials, a plastic zone develops at the tip of

the crack and as the applied load increases, the plastic zone increases in size until the crack grows and the material behind the crack tip unloads. The plastic loading and unloading cycle near the crack tip leads to the dissipation of energy as heat and this dissipative term has to be added to the energy balance relation devised by Griffith for brittle materials. Hence, the total energy for formation of a new surface is given by $G = 2\gamma + G_p$, where γ is the surface energy and G_p is the plastic dissipation per unit area of crack growth. The modified version of Griffith's energy criterion can then be given by

$$\sigma_f \sqrt{a} = \sqrt{\frac{2GY}{\pi}} \tag{6.7}$$

This mechanism can be extended to understand electro–fracture where the defect (non-crystalline region) propagates through a dielectric material due to electrostatic forces. The defect spontaneously propagates when the energy required to create the crack is less than the strain energy liberated by the cracked material. As shown above, the elastic energy in the system due to mechanical stretching is given by $\frac{1}{2}\sigma\varepsilon = \sigma^2/2Y$, where σ and ε are the mechanical stress and strain respectively. The bond breakage gives rise to an enhanced field, E, at the tip resulting in an additional internal mechanical stress in the system due to the electric field. Hence, the mechanical compressive stress induced by an electric field is given by $\sigma = \frac{1}{2}\varepsilon_0\varepsilon_r E^2$ resulting in an induced strain energy density of $\varepsilon_0^2\varepsilon_r^2 E^4/8Y$. Note that there is also electrostatic strain energy in the sample given by $\frac{1}{2}\varepsilon_0\varepsilon_r E^2$, however, the effect of this energy is minuscule compared to the induced strain energy in the material due to the

defect. If there is a spherical crack of radius a then the volume displaced is πa^2 and the energy released is given by $\frac{\varepsilon_0^2 \varepsilon_r^2 E^4}{8Y} \pi a^2$. As discussed above, a part of this energy is used create two new surfaces and rest is lost in the form of plastic deformation energy. Hence the energy required for defect propagation is $G\pi a$. Consequently, the defect will propagate and result in dielectric breakdown when the $\frac{\varepsilon_0^2 \varepsilon_r^2 E^4}{8Y} \pi a^2 > G\pi a^2$. The resultant critical electric breakdown is thus given by

$$E_b = \sqrt[4]{\frac{8GY}{\varepsilon_0^2 \varepsilon_r^2 a}} \tag{6.8}$$

6.4 Effect of temperature

In the previous sections, we have developed the simulation to mimic dielectric breakdown in polymers. The breakdown strength of several polymers is sensitive to the temperature and it is generally observed to decrease with increase in the ambient temperature. This temperature dependency has been a topic of discussion for decades. The conventional theory (electronic breakdown) of calculating breakdown strength of materials does not predict this inverse relationship of temperature and breakdown strength. However, the electro–fracture mode of breakdown explored in this dissertation should give us the experimentally observed breakdown relationship between breakdown strength and temperature.

To investigate the breakdown strength and temperature dependency, we use the semi–crystalline 1000 carbons PE at 300 K as the initial seed. We cool the sample to 250 K at a rate of 5 K/ns, followed by equilibration at that temperature for 5 ns. We

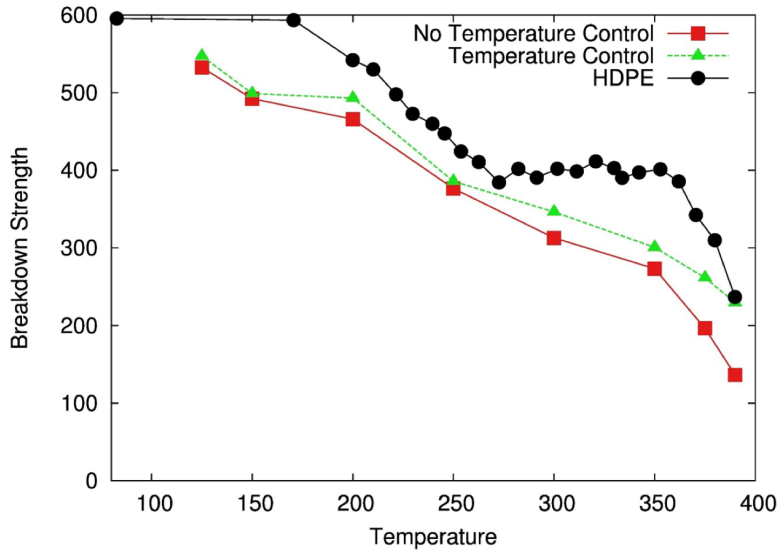

Figure 6.12: Breakdown strength dependence on temperature obtained from simulation using the two ensembles (NPT and NPH) compared to experimentally obtained breakdown strength. [11]

use the final trajectory thus obtained as the seed for two different sets of simulations. The first set of simulations is to study dielectric breakdown mechanism by applying various electric fields in X, Y, and Z-directions, while the other simulation is to cool the sample further to 200 K and equilibrate at the temperature. Again two sets of simulations were performed on the final configuration obtained at 200 K. These steps were iterated for calculation of breakdown strength of the sample at 150 K and 125 K. We also heat the sample from 300 K following the same procedure to find the breakdown strength of the sample at 350, 375, and 390 K. The temperature was kept below the melting point of the sample.

The calculated breakdown strength for the sample is shown in the figure 6.12. The dielectric strength of the sample calculated using simulations is comparable to the experimentally obtained breakdown strength of the material [11]. At low

temperatures, we observe a continuous increase in breakdown strength with the decrease in temperature, but in experiments a plateau is observed. It is our conjecture that this discrepancy in results is due to failure of simulations to predict electronic breakdown and at low temperatures electronic breakdown is responsible for the dielectric breakdown. We calculated breakdown strength for PE using both NPT and NPH ensemble for comparison. Both flavors of simulation give similar predictions at the low temperature, but at the higher temperatures (> 250 K) they tend to diverge. The calculated dielectric strength is lower for the NPH at a higher temperature because of the restricted heat dissipation in the system. This trend is also observed in the experiments and is usually associated with the thermal breakdown of the material. In summary, we can now predict the dielectric strength of materials due to electromechanical breakdown using molecular dynamics.

Chapter 7

Conclusions and Rational Design

Modeling and simulation of dielectric properties of polymer for high energy storage capacitors is the central focus of this dissertation. The systems studied in this thesis are polyolefins and their derivatives. Designing a suitable dielectric material has multi–property constraints, like static relative permittivity, breakdown strength, dielectric loss, polymer morphology, glass transition and melting temperatures, defect content (and their effects), electronic structure, thermal conductivity, etc. On the most basic level, a good dielectric material should have high static relative permittivity and breakdown strength and negligible dielectric loss. However, one cause of complication is that these properties are not independent of each other, a positive change in one often leads to a negative shift in another. Hence understanding the interplay between these properties has been a topic of discussion for decades. In this dissertation, we have systematically investigated the fundamentals behind the relationship of each of the quantities. Specifically, we discover that ordering/crystallinity plays a critical role on each of the dielectric property.

In Chapter 2, we explore the significance of water in the system while finding several points of agreement between the simulations and experiments involving PE–OH. We discover that there are two classes of water in the system: free and bound

water. Free water is the water in the material which is not trapped and can easily escape from the system, while the bound water is hydrogen bonded to hydroxyls in the sample. This observation in simulations led to experimental exploration. On removal of free water from the sample in experiments, the static relative permittivity decreased and agreed with the simulation predictions. Additionally, the stoichiometric ratio of bound water molecules to hydroxyl groups (1:2) also matched simulations. The dielectric loss analysis of the water molecules only explains how additional "free" water increases the static relative permittivity without adding loss in the experimental measurement. We discover that the low dielectric loss even in the presence of hydroxyls is due to hydrogen bonding. This decrease in dielectric loss comes at the cost of decreased dielectric permittivity contribution of hydroxyls, but the presence of bound water balances out this loss. To further validate the effect of hydrogen bonded water we separately analyzed the dipole autocorrelation of each CH-OH group, and we found that 69% of the groups were bound to one another via a bridging water molecule, while the other 31% were either single or H–bonded directly to another –OH group. The hydroxyls those were bridged by water relaxed the least while those not water-bridged relaxed the most.

In Chapters 3 and 4, we explored the effects of other polar groups on enhancing the dielectric properties in polyethylene. However, there are more fundamental questions examined in the process. In chapter 3 we calculated the static relative permittivity for the samples. We compare the popular method to predict the dielectric properties of materials DFT to MD. By implementing both techniques on the same ordered arrays of functional polyolefins, we confirm that both methodologies

yield identical estimates for the dipole moments and hence the ionic component of the static relative permittivity measured from each technique are comparable. Additionally, MD simulations of more realistic semi-crystalline morphologies yield estimates for this polar contribution that are in good agreement with the limited experiments in the field. However, these predictions are up to 10 times larger than those for pure crystalline simulations. Hence, we show that the constraints provided by the surrounding chains significantly impede dipolar relaxations in the crystalline regions, whereas amorphous chains must sample all configurations to attain their fully isotropic spatial distributions. Our results argue strongly that crystallinity plays a critical and inverse role in increasing static relative permittivity. In Chapter 4 we investigated the effect of other polar groups on the relaxation of polyethylene i.e. dielectric loss. We developed a scheme for capturing the relaxation process using time-temperature superposition for PE–OH. The results from tTS were compared to a single long simulation which ran to microseconds. The two flavors of MD simulations give the same relaxation behavior thus providing us with a significantly faster and accurate method for the calculation of dielectric properties. The method was extended to predict the dielectric loss of other polar groups. The relaxation time was exponentially related to the dipole moment of the side group. This suggests that one possible path for designing material with low dielectric loss is by keeping the dipole moment small. This result supports the results from Chapter 2, where the reduction in static dielectric permittivity contribution of hydroxyl reduces the loss in the material. This provides us with a pathway for designing better dielectric material by increasing the concentration of polar groups to the point where they are

still spatially distributed.

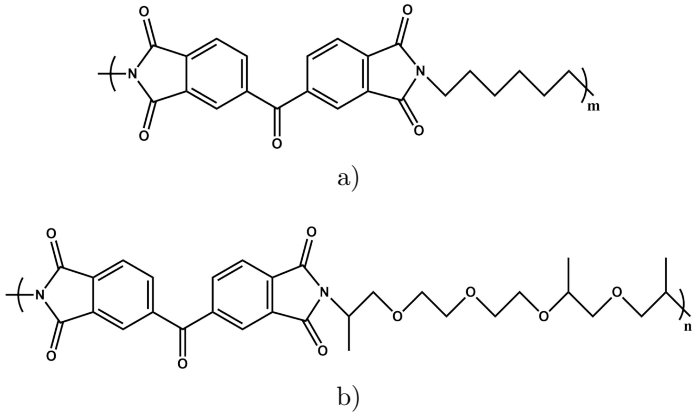

a)

b)

Figure 7.1: Chemical structure of (a) BTDA-HDA and (b) BTDA-HK511.

Chapter 5 and 6 shifts the focus from the calculation of dielectric permittivity and loss to the dielectric strength. We probe the mechanism behind the susceptibility of breakdown strength to the temperature in polymeric dielectrics. Using simulations we demonstrate that although electromechanical breakdown has not received much attention in the literature, it is the primary cause of the breakdown in many polymeric systems. This assertion is supported by the common observation of a reduction in breakdown strength during softening. The electromechanical breakdown may also act in combination with other breakdown mechanisms leading to failure of the material. One of the reasons why the idea of electromechanical breakdown is dismissed in literature is due to its failure to capture plastic deformation and prediction of unrealistic thinning. We tackle these criticisms to the breakdown mechanism by demonstrating it to be a fracture mechanics problem. We determine that the non-crystalline within a dielectric material act as defects in the sample leading to breakdown propagation. Thus, the breakdown is both a function of toughness and Young's modulus of the material. This result also ties back to the experimentally

observed increase of breakdown strength for PE–OH system, where the hydrogen bonding in the non-crystalline region leads to extra stability of the system. Hence inducing local crystallinity in the sample can further increase the breakdown strength of the material.

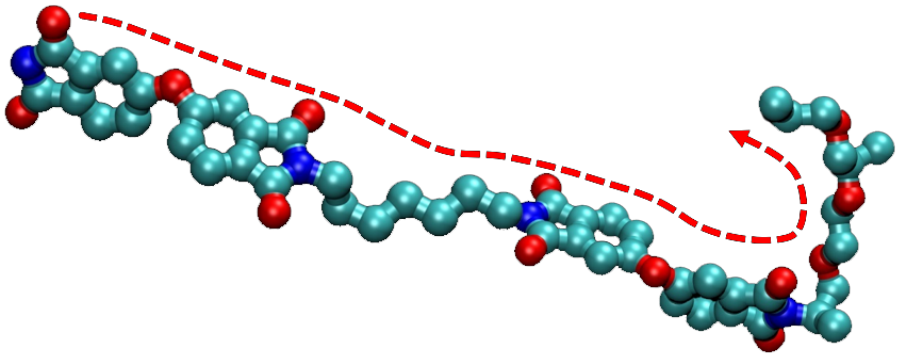

Figure 7.2: Sanpshot of a unit of copolymer BHH2.

To summarize the dielectric permittivity increases due to the amorphous regime, breakdown strength increases due to local crystallinity, and dielectric loss decreases by spatially distributing the polarizable group. Using these ideas as the blueprint, we design a copolymer and investigate its properties for applications requiring enhanced energy density. We focus on creating a periodic copolymer resulting in consistent properties in the material. The two repeat units used for the design of the copolymer are BTDA-HDA and BTDA-HK511. The chemical structure of both of them is shown in figure 7.1. We study five systems namely BHH0, BHH1, BHH2, BHH3, and BHH4 with varying ratio of BTDA-HK511 and BTDA-HDA as 0:100, 25:75, 50:50, 75:25, and 100:0. A single chain with 50 repeating blocks, where each block consists of 4 monomer units varying to generate desired concentration of units in the sample, was simulated.

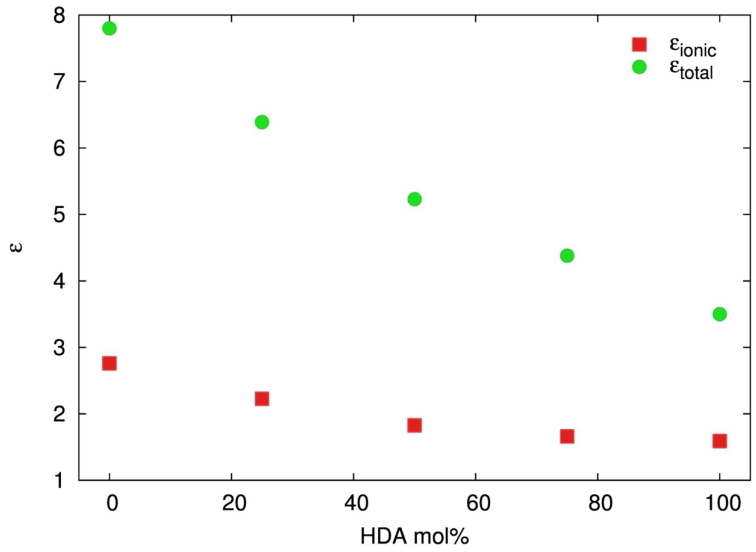

Figure 7.3: Static dielectric permittivity measured for all the copolymers. The red squares represent the ionic component of dielectric permittivity calculated from simulations. The green circles are the total dielectric permittivity measured for the sample experimentally.

Each sample was equilibrated at 1000 K for 5 ns to generate an amorphous chain. The samples were then cooled to 700 K at the rate of 50 K/ns. After reaching 700 K, the cooling rate was slowed down to 5 K/ns and samples were cooled until they reached 300 K . Note that unlike PE where we start slow cooling at 500 K, here we start cooling at a higher temperature since we expect the T_g of the samples to be high. At 300 K the volume of the system is equilibrated for 10 ns, followed by the production run of 20 ns for calculation of static relative permittivity. All the samples generated visually seemed to be amorphous in nature. However, on studying the local structure of a block, we find that BTDA-HK511 has an end unit similar to polyethylene glycol (PEO). The structure of PEO is helical in nature, and this is observed in our system as well. The figure 7.2 displays this helical induced twist in the sample. We find that this unit adds amorphous nature to the system. We also

HDA mol/%	τ (ns)	β	$\tau_a vg$ (ns)
0	28.81	0.17	1.67E+4
25	49.54	0.28	6.37E+2
50	61.55	0.27	9.55E+2
75	70.24	0.30	6.51E+2
100	78.53	0.26	1.50E+3

Table 7.1: Streched exponential fitting parameters for the dipole moment DCF for various copolymers.

observe $\pi - \pi$ stacking of the rings of BTDA which introduces local crystallinity in the system. Further analysis of this morphology descriptions needs to be conducted.

The ionic component for all the samples was calculated using eq 2.3 and are shown in figure 7.3. We observe that the dielectric permittivity increases with increasing HK511 content in the system. This increase in relative permittivity supports our notion of that the amorphous regime increases the static permittivity. The introduction of the PEO-like segment in the structure provides more flexibility to the polarizable groups in the chain. We also measured the static relative permittivity of the sample experimentally and observed the same trend in results. Note that the static relative permittivity from MD results is lower than that observed in experiments. This discrepancy in results is due to the failure of classical MD in capturing the electronic component of permittivity. This is where DFT calculations can play a critical role in predicting the total static permittivity of the material.

Further, we compare the dielectric loss in the sample measured using simulations to those using experiments. After the 20 ns production run in all the samples, we observe that all samples are $\approx 50 - 70\%$ unrelaxed. Hence, we use tTS scheme to generate a fully relaxed system. All the samples were heated to 350, 400, 450,

500, 550, and 600 K under NVT conditions. At each temperature, the simulations were run for 25 ns. The last 20 ns of each simulation were used to calculated the dipole correlation function. The obtained dipole correlation functions were used to generate a master curve for each sample presented in figure 7.4a. The generate master curves were then fitted using stretched exponential function, and the parameter are mentioned in Table 7.

We observe that introduction of HDA in the sample significantly reduces the relaxation time of the chain. We conjecture that this is because HDA increases the spatial distribution and separation between the HK511 in the sample. The fitted functions were used to calculate the dielectric loss in the samples. The calculated dielectric loss for the samples from simulations are compared to experimentally obtained dielectric loss in the figure 7.4b. The time frame for simulations and experiments are drastically different; nevertheless, in the small window of overlap, they seem to be comparable to each other. The use of tTS has allowed us to access the loss at MHz's, which was previously inaccessible using classical MD simulations.

We also study the response of the polymers to an applied external electric field and determine the breakdown strength of each sample. We apply the electric field to all sample at 300 K in X, Y, and Z-directions. The procedure of applying the electric field is the same as discussed in past chapters, where the field is ramped to the desired field at 50 MV/m ns under NPH ensemble, followed by measuring average strain in the sample in the last 200 ps of the 2 ns equilibration run. The averaged measured strain for each copolymer at given electric field is presented in figure 7.5a. Note that the bond potential used in these simulations does not support

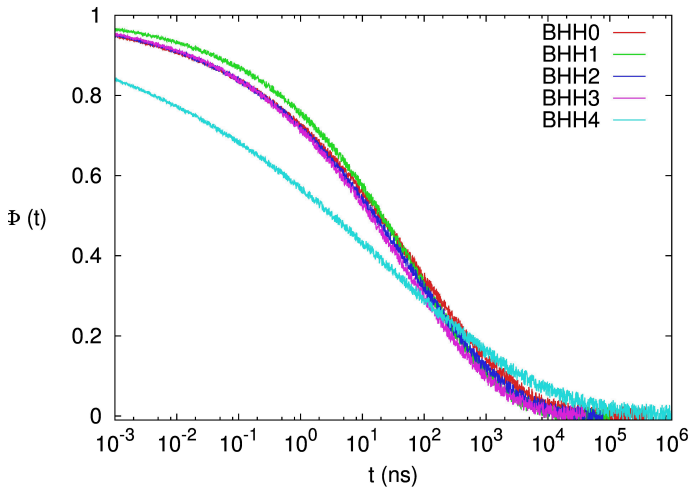

a)

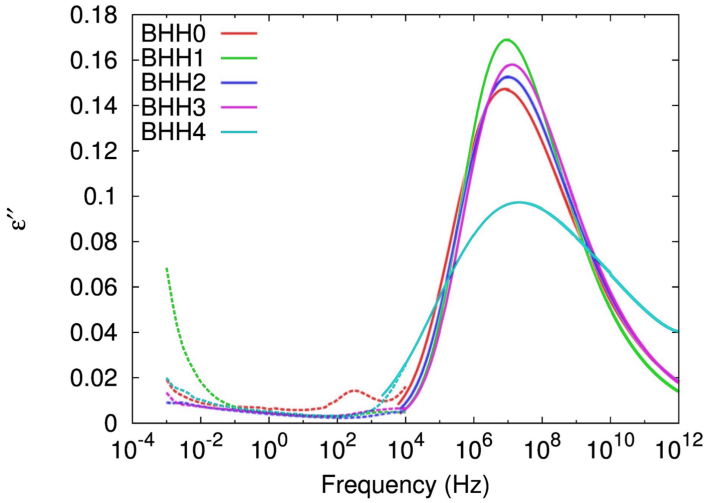

b)

Figure 7.4: (a) The master curve for dipole correlation function and (b) dielectric loss for the copolymers. The dotted lines in the loss curve are dielectric loss data obtained from experiments.

bond breaking. As shown in the past chapters, bond breaking introduces the correct mechanism but has an insignificant effect on the electric field – strain curve. Thus, within approximations, we can still use the non-breaking bond potential for predicting the breakdown strength in the samples. We interpolate the electric field at the strain for 0.6 for each sample and represent them in the figure 7.5a. We observe that the

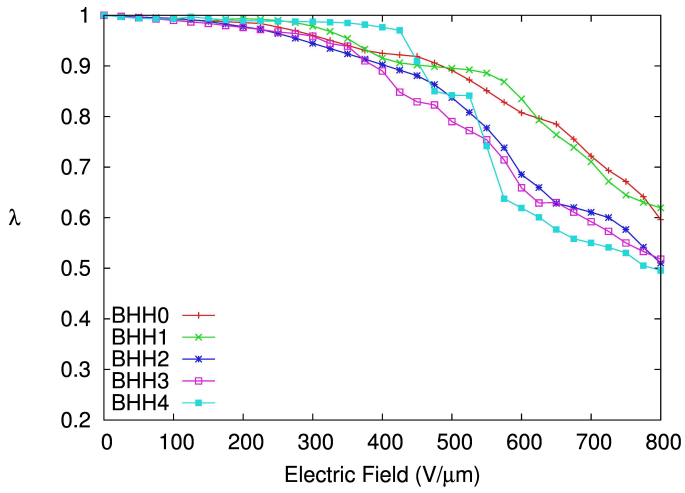

a)

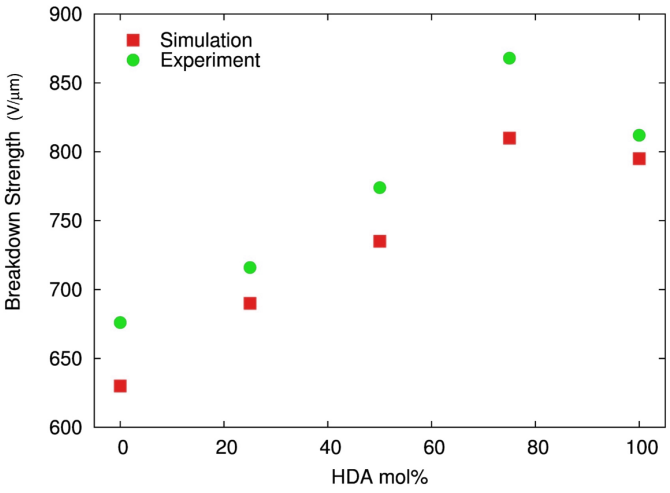

b)

Figure 7.5: (a) Electric field versus strain relationship and (b) breakdown strength for copolymers.

breakdown strength of the material increases with increasing HDA content in the system; this again can be due to the nature of HK511 group which disrupts the packing of chains. The breakdown strength calculated using the simulations and experiments are in qualitative agreement with each other. However, the predicted breakdown strength from simulations is lower; it is our conjecture this might be due to the absence of polarizability in the simulation potential or due to the lower

crystallinity of the simulation samples (or both). It is important to note that here we can now predict the breakdown strength of polymeric materials which not only gives a tool to for designing polymer dielectrics but also helps us understand the dielectric breakdown mechanism in polymers.

Bibliography

(1) Ahlfont, K.; Sandborgh, H. *Pulsed Power Technology and Applications Scandinavia*; tech. rep. April; 1999, TR–112566.

(2) Christen, T.; Carlen, M. W. *Journal of Power Sources* **2000**, *91*, 210–216.

(3) Abruña, H. D.; Kiya, Y.; Henderson, J. C. *Physics Today* **2008**, *61*, 43–47.

(4) Ho, J.; Ramprasad, R.; Boggs, S. *IEEE Transactions on Dielectrics and Electrical Insulation* **2007**, *14*, 1295–1301.

(5) Bottcher, C. J.F.C.J. F.; van. Belle, O. C.; Bordewijk, P. P.; Rip, A., *Theory of electric polarization*; Elsevier Scientific Pub. Co: 1973.

(6) Ahmad, Z. In *Dielectric Material*.

(7) Ahmad, Z., *Chapter 1 Polymeric Dielectric Materials*; InTech: 2012, pp 3–26.

(8) Dervos, C. T.; Tarantili, P. a.; Athanassopoulou, M. D. *Journal of Physics D: Applied Physics* **2009**, *42*, 135409.

(9) Boggs, S. a. *IEEE Electrical Insulation Magazine* **2010**, *26*, 8–22.

(10) Boggs, S.; Ho, J.; Jow, T. *IEEE Electrical Insulation Magazine* **2010**, *26*, 7–13.

(11) Ieda, M. *IEEE Transactions on Electrical Insulation* **1980**, *EI-15*, 206–224.

(12) Dictionary, O. E., *Oxford Dictionary of English*; Oxford University Press: 2010.

(13) Frenkel, D; Smit, B, *Understanding Molecular Simulation: From Algorithms to Applications*; Computational science series; Elsevier Science: 2001.

(14) Siu, S. W. I.; Pluhackova, K.; Böckmann, R. A. *Journal of Chemical Theory and Computation* **2012**, *8*, 1459–1470.

(15) Jorgensen, W. L.; Maxwell, D. S.; Tirado-Rives, J. *Journal of the American Chemical Society* **1996**, *118*, 11225–11236.

(16) Jorgensen, W.; Gao, J. *The Journal of Physical Chemistry* **1986**, *47907*, 2174–2182.

(17) Robertson, M. J.; Tirado-Rives, J.; Jorgensen, W. L. *Journal of Chemical Theory and Computation* **2015**, *11*, 3499–3509.

(18) Henchman, R. H. Simulation Studies of the Structure and Energetics of a Host-guest System., 1999.

(19) Newton, I; Bernoulli, D; Leseur, T; MacLaurin, C; Jacquier, F; Euler, L, *Philosophiæ naturalis principia mathematica*; Philosophiæ naturalis principia mathematica v. 1; excudit G. Brookman; impensis T. T. et J. Tegg, Londini: 1833.

(20) Verlet, L. *Physical Review* **1967**, *159*, 98–103.

(21) Andersen, H. C. *The Journal of chemical physics* **1980**, *72*, 2384–2393.

(22) Nosé, S. *Molecular physics* **1984**, *52*, 255–268.

(23) Nosé, S. *The Journal of chemical physics* **1984**, *81*, 511–519.

(24) Hoover, W. G. *Physical review A* **1985**, *31*, 1695.

(25) Martyna, G. J.; Klein, M. L.; Tuckerman, M. *The Journal of chemical physics* **1992**, *97*, 2635–2643.

(26) Bond, S. D.; Leimkuhler, B. J.; Laird, B. B. *Journal of Computational Physics* **1999**, *151*, 114–134.

(27) Hünenberger, P. H. In *Advanced computer simulation*; Springer: 2005, pp 105–149.

(28) Yuan, X.; Matsuyama, Y.; Chung, T. C. M. *Macromolecules* **2010**, *43*, 4011–4015.

(29) Yamamoto, T.; Sawada, K. *Journal of Chemical Physics* **2005**, *123*, 234906.

(30) Liu, C.; Muthukumar, M. *The Journal of Chemical Physics* **1998**, *109*, 2536.

(31) Fujiwara, S.; Sato, T. *The Journal of Chemical Physics* **1997**, *107*, 613.

(32) Welch, P.; Muthukumar, M. *Physical Review Letters* **2001**, *87*, 218302.

(33) Yamamoto, T. *Polymer* **2009**, *50*, 1975–1985.

(34) Yi, P.; Rutledge, G. C. *The Journal of chemical physics* **2009**, *131*, 134902.

(35) Gee, R. H.; Lacevic, N.; Fried, L. E. *Nature materials* **2006**, *5*, 39–43.

(36) Ramos, J.; Martínez-Salazar, J. *Journal of Polymer Science Part B: Polymer Physics* **2011**, *49*, 421–430.

(37) Misra, M.; Agarwal, M.; Sinkovits, D. W.; Kumar, S. K.; Wang, C.; Pilania, G.; Ramprasad, R.; Weiss, R. a.; Yuan, X.; Chung, T. C. M. *Macromolecules* **2014**, *47*, 1122–1129.

(38) Stone, J. E.; Phillips, J. C.; Freddolino, P. L.; Hardy, D. J.; Trabuco, L. G.; Schulten, K. *Journal of Computational Chemistry* **2007**, *28*, 2618–2640.

(39) Anderson, J. a.; Lorenz, C. D.; Travesset, a. *Journal of Computational Physics* **2008**, *227*, 5342–5359.

(40) Plimpton, S. *J. Comp. Phys.* **1995**, *117*, 1–19.

(41) Bunn, C. W. *Transactions of the Faraday Society* **1939**, *35*, 482–491.

(42) Frohlich, H.; Maradudin, A., *Theory of Dielectrics*, 2nd ed.; 2; Oxford University Press: 1958; Vol. 12, p 192.

(43) Borodin, O.; Bedrov, D.; Smith, G. D. *Macromolecules* **2002**, *35*, 2410–2412.

(44) Cormia, R. L.; Price, F. P.; Turnbull, D *The Journal of Chemical Physics* **1962**, *37*, 1333–1340.

(45) Teh, J. W.; Blom, H. P.; Rudin, A *Polymer* **1994**, *35*, 1680–1687.

(46) Yu, X.; Kong, B.; Yang, X. *Macromolecules* **2008**, *41*, 6733–6740.

(47) Jorgensen, W. L.; Chandrasekhar, J.; Madura, J. D.; Impey, R. W.; Klein, M. L. *The Journal of Chemical Physics* **1983**, *79*, 926.

(48) Karasawa, N.; Goddard, W. A. *Macromolecules* **1995**, *28*, 6765–6772.

(49) Noskov, S. Y.; Lamoureux, G.; Roux, B. *The journal of physical chemistry. B* **2005**, *109*, 6705–13.

(50) Provencal, R. A.; Casaes, R. N.; Roth, K.; Paul, J. B.; Chapo, C. N.; Saykally, R. J.; Tschumper, G. S.; Schaefer, H. F. *The Journal of Physical Chemistry A* **2000**, *104*, 1423–1429.

(51) Alvarez, F.; Alegra, A.; Colmenero, J. *Physical Review B* **1991**, *44*, 7306–7312.

(52) Buchner, R; Barthel, J; Stauber, J *Chemical Physics Letters* **1999**, *306*, 57–63.

(53) Hohenberg, P.; Kohn, W. *Physical Review B* **1973**, *7*, 1912–1919.

(54) Kohn, W.; Sham, L. J. *Physical Review* **1965**, *140*, 1133–1138.

(55) Kresse, G.; Hafner, J. *Physical Review B* **1993**, *47*, 558–561.

(56) Klimeš, J.; Bowler, D. R.; Michaelides, A. *Journal of physics. Condensed matter : an Institute of Physics journal* **2010**, *22*, 022201.

(57) Liu, C. S.; Pilania, G.; Wang, C.; Ramprasad, R. *Journal of Physical Chemistry A* **2012**, *116*, 9347–9352.

(58) Blöchl, P. E. *Physical Review B* **1994**, *50*, 17953–17979.

(59) Baroni, S.; De Gironcoli, S.; Dal Corso, A.; Giannozzi, P. *Reviews of Modern Physics* **2001**, *73*, 515–562.

(60) Pilania, G.; Ramprasad, R. *Journal of Materials Science* **2012**, *47*, 7580–7586.

(61) Bernardini, F.; Fiorentini, V.; Vanderbilt, D. *Physical Review B* **1997**, *56*, R10024–R10027.

(62) Zhao, X.; Vanderbilt, D. *Physical Review B* **2002**, *65*, 233106.

(63) C. Mike Chung, T. *Green and Sustainable Chemistry* **2012**, *02*, 29–37.

(64) Haggenmueller, R.; Fischer, J. E.; Winey, K. I.; Pennsyl, V; December, R. V.; Re, V; Recei, M.; February, V *Macromolecules* **2006**, *39*, 2964–2971.

(65) Ramos, J.; Mart, J.; Sanmart, S. *Macromolecules Symposia* **2012**, *312*, 97–107.

(66) Lavine, M. S.; Waheed, N.; Rutledge, G. C. *Polymer* **2003**, *44*, 1771–1779.

(67) Fujiwara, S.; Sato, T. *Journal of Chemical Physics* **2008**, *107*, 613.

(68) Wang, S.; Yu, X.; Kong, B.; Yang, X. *Science China Chemistry* **2013**, *56*, 195–202.

(69) Tomer, V; Polizos, G; Randall, C. A.; Manias, E; Tomer, V; Polizos, G; Randall, C. A.; Manias, E *Journal of Applied Physics* **2011**, *109*, 074113.

(70) Flory, P. J., *Principles of Polymer Chemistry*; Baker lectures 1948; Cornell University Press: 1953.

(71) Wunderlich, B.; Cormier, C. *Journal of Polymer Science : Part A-2* **1967**, *5*, 987–988.

(72) Zhang, M.; Yuan, X.; Wang, L.; Chung, T. C. M.; Huang, T.; Degroot, W. *Macromolecules* **2014**, *47*, 571–581.

(73) Dong, R.; Ranjan, V.; Buongiorno Nardelli, M.; Bernholc, J. *Physical Review B* **2015**, *92*, 024203.

(74) Rubinstein, M.; Colby, R. H., *Polymer Physics*; OUP Oxford: 2003, p 456.

(75) Thakur, Y.; Dong, R.; Lin, M.; Wu, S.; Cheng, Z.; Hou, Y.; Bernholc, J.; Zhang, Q. *Nano Energy* **2015**, *16*, 227–234.

(76) Barshaw, E. J.; White, J; Chait, M. J.; Cornette, J. B.; Bustamante, J; Folli, F; Biltchick, D; Borelli, G; Picci, G; Rabuffi, M **2007**, *43*, 2006–2008.

(77) Kaznessis, Y. N.; Hill, D. A.; Maginn, E. J. *The Journal of chemical physics* **1999**, *111*, 1325–1334.

(78) Jämbeck, J. P. M.; Unge, M.; Laihonen, S. In *Electrical Insulation and Dielectric Phenomena (CEIDP), 2015 IEEE Conference on*, IEEE: 2015, pp 146–149.

(79) Kubo, R. *Journal of the Physical Society of Japan* **1957**, *12*, 570–586.

(80) Borisova, T. I. *Polymer Science U.S.S.R.* **1970**, *12*, 1060–1066.

(81) Crossley, J. *Advances in Molecular Relaxation Processes* **1974**, *6*, 39–59.

(82) Wagner, K. W. *Transactions of the American Institute of Electrical Engineers* **1922**, *XLI*, 1034–1044.

(83) Chadband, W., *Electrical Degradation and Breakdown in Polymers*; 11-12; P. Peregrinus: 1992; Vol. 38, p 404.

(84) Fothergill, J. C. In *IEEE transactions on electrical insulation*, IEEE: 1991; Vol. 26, pp 1124–1129.

(85) Ritsko, J. J., *J.J. Ritsko, in Electronic Properties of Polymers*; Wiley new york: 1982.

(86) Stark, K. H.; Garton, C. G. *Nature* **1955**, *176*, 1225–1226.

(87) Moll, H. W.; LeFevre, W. J. *Industrial & Engineering Chemistry* **1948**, *40*, 2172–2179.

(88) McKeown, J. *Proceedings of the Institution of Electrical Engineers* **1965**, *112*, 824.

(89) Doi, A. *Journal of Materials Science* **1987**, *22*, 4377–4380.

(90) Gerratt, A. P.; Bergbreiter, S. *Journal of Micromechanics and Microengineering* **2013**, *23*, 067001.

(91) Wang, Y.; Zhou, X.; Lin, M.; Zhang, Q. M. *Applied Physics Letters* **2009**, *94*, 202905.

(92) Li, J.; Gong, H.; Yang, Q.; Xie, Y.; Yang, L.; Zhang, Z. *Applied Physics Letters* **2014**, *104*, 263901.

(93) Blok, J.; Legrand, D. G. *Journal of Applied Physics* **1969**, *40*, 288–293.

(94) Sun, W.; Chen, Z.; Huang, S.-Y. *Fluid Phase Equilibria* **2005**, *238*, 20–25.

(95) Peng, T. J.; Landel, R. F. *Journal of Applied Physics* **1972**, *43*, 3064–3067.

(96) Ogden, R. W. *Brunel University Mathematics Technical Papers ...* **2008**, 1–21.

(97) Yeoh, O. H. *Rubber Chemistry and Technology* **1990**, *63*, 792–805.

(98) Morman, K. N.; Pan, T. Y. *Rubber Chemistry and Technology* **1988**, *61*, 503–533.

(99) James, H. M.; Guth, E. *Journal of Chemical Physics* **1943**, *11*, 455.

(100) Gent, a. N. *Rubber Chemistry and Technology* **1996**, *69*, 59–61.

(101) Zhou, M. In *Proceedings of the Royal Society of London A: Mathematical, Physical and Engineering Sciences*, The Royal Society: 2003; Vol. 459, pp 2347–2392.

(102) Zhang, T.-Y.; Liu, G.; Wang, Y. *Acta Materialia* **2004**, *52*, 2025–2035.

(103) Riggleman, R. A.; De Pablo, J. J. *Journal of Chemical Physics* **2008**, *128*, DOI: 10.1063/1.2925684.

(104) Baljon, a. R. C.; Robbins, M. O. *Computational and Theoretical Polymer Science* **1999**, *9*, 35–40.

(105) Stevens, M. J. *Macromolecules* **2001**, *34*, 2710–2718.

(106) Popov, K. V.; Knyazev, V. D. *Journal of Physical Chemistry A* **2014**, *118*, 2187–2195.

(107) Luo, Y. R., *Handbook of Bond Dissociation Energies in Organic Compounds*; CRC Press: 2002.

(108) Nyden, M. R.; Noid, D. W. *The Journal of Physical Chemistry* **1991**, *95*, 940–945.

(109) Zhou, X.; Zhao, X.; Suo, Z.; Zou, C.; Runt, J.; Liu, S.; Zhang, S.; Zhang, Q. M. *Applied Physics Letters* **2009**, *94*, 2007–2010.

(110) Griffith, A. A. *Philosophical transactions of the royal society of london. Series A, containing papers of a mathematical or physical character* **1921**, *221*, 163–198.

(111) Inglis, C. E. *Spie Milestone series MS* **1997**, 3–17.

(112) Irwin, G. R. *Spie Milestone series MS* **1957**, *137*, 16.